TECHNISCHE UNIVERSITÄT MÜNCHEN

Lehrstuhl E23 für Technische Physik

Walther-Meißner-Institut für Tieftemperaturforschung
der Bayerischen Akademie der Wissenschaften

Experiments on Two-Resonator Circuit Quantum Electrodynamics: A Superconducting Quantum Switch

Elisabeth Christiane Maria Hoffmann

Vollständiger Abdruck der von der Fakultät für Physik der Technischen Universität München zur Erlangung des akademischen Grades eines

Doktors der Naturwissenschaften

genehmigten Dissertation.

Vorsitzender:	Univ.-Prof. Dr. Björn Garbrecht
Prüfer der Dissertation:	1. Univ.-Prof. Dr. Rudolf Gross
	2. Univ.-Prof. Jonathan J. Finley, Ph.D.

Die Dissertation wurde am 27. März 2013 bei der Technischen Universität München eingereicht und durch die Fakultät für Physik am 29. Mai 2013 angenommen.

You may say I'm a dreamer
but I'm not the only one ...
John Lennon

Abstract

The field of cavity quantum electrodynamics (QED) studies the interaction between light and matter on a fundamental level. In typical experiments individual natural atoms are interacting with individual photons trapped in three-dimensional cavities. Within the last decade the prospering new field of circuit QED has been developed. Here, the natural atoms are replaced by artificial solid state quantum circuits offering large dipole moments which are coupled to quasi-onedimensional cavities providing a small mode volume and hence a large vacuum field strength. In our experiments Josephson junction based superconducting quantum bits are coupled to superconducting microwave resonators. In circuit QED the number of parameters that can be varied is increased and regimes that are not accessible using natural atoms can be entered and investigated. Apart from design flexibility and tunability of system parameters a particular advantage of circuit QED is the scalability to larger system size enabled by well developed micro- and nanofabrication tools. When scaling up the resonator-qubit systems beyond a few coupled circuits, the rapidly increasing number of interacting subsystems requires an active control and directed transmission of quantum signals. This can, for example, be achieved by implementing switchable coupling between two microwave resonators. To this end, a superconducting flux qubit is used to realize a suitable coupling between two microwave resonators, all working in the Gigahertz regime. The resulting device is called quantum switch. The flux qubit mediates a second order tunable and switchable coupling between the resonators. Depending on the qubit state, this coupling can compensate for the direct geometric coupling of the two resonators. As the qubit may also be in a quantum superposition state, the switch itself can be "quantum": it can be a superposition of "on" and "off".

This work presents the theoretical background, the fabrication techniques and spectroscopy measurements on a quantum switch device. In particular, the quantum switch is realized using a flux qubit galvanically coupled to two microwave resonators. Despite the fact that this design requires a further theoretical investigation beyond the original model, the switching behavior is demonstrated.

Contents

List of Figures

Chapter 1

Introduction

In the late 1920s, Paul Dirac formulated the theory of interaction between light and matter [1] and described the quantized electromagnetic field as an ensemble of harmonic oscillators interacting with charged particles. Based on the quantization of light, the area of optics expanded by what is known today as *quantum optics*. The invention of the laser in 1958 [2] and the related technical developments in the following years [3] laid the basis for modern quantum optics [4, 5].

These days, simulations of complex physical systems require fast and powerful computers. Already in 1982, Richard Feynman pointed out that devices operating according to the laws of quantum mechanics would be much more efficient for simulations of quantum systems [6]. For the realization of such a device, different quantum mechanical systems are investigated regarding their usage in quantum simulation. Here, quantum bits, or qubits are the fundamental information unit in a digital quantum processor and equivalent to bits in a classical processor. A qubit is a quantum mechanical two-level system with transition-frequency ω_{Q}. The qubit state, which in general is a superposition of the ground state $|g\rangle$ and the excited state $|e\rangle$, can be manipulated by external control parameters and determined by a suitable readout process. There is a large and steadily increasing number of possible qubit realizations. To this end, the field of quantum optics has been particularly successful. Neutral atoms [7–14] or ions [15–20] as qubits coupled to electromagnetic quantized fields provide promising systems for quantum simulation processes. However, after the demonstration of quantum coherent behavior of solid state systems about a decade ago, solid state based quantum systems are attracting increasing research effort.

From cavity QED to circuit QED

In 2012, the experimental demonstration of direct, non-demolition observation of individual quantum particles earned Serge Haroche and David Wineland the Nobel Price in Physics. Both work in the field of quantum optics and study the fundamental interaction between light and matter. While Wineland used photons to detect the states of trapped ions [21, 22], Haroche explored the light-matter interaction by coupling "trapped light" and "flying atoms". His observation of an enhanced spontaneous emission of single atom in a cavity [23] laid the basis for a new research field in quantum optics, the field of *cavity* quantum electrodynamics (QED) [24]. Moreover, by detecting the state of atoms moving through a cavity and interacting with the quantized cavity modes he was able to detect the state of the photons in the cavity in a non-demolition manner [25, 26].

An important condition to investigate the coherent atom-photon interaction is the coupling of the two systems being much larger than the photon loss rate of the cavity

and the atom decay rate into modes other than the cavity mode. The atom-photon coupling strength is in general given by the product of the dipole moment and the zero-point electromagnetic field strength of the cavity mode which decreases with increasing mode-volume. In case of a single Rydberg atom in a Fabry-Pérot cavity, the coupling of the two systems is relatively large due the large atomic radius of the Rydberg atom which results in a large dipole moment.

Replacing the Rydberg atom by an artificial atom with an even larger size and hence larger dipole moment and reducing the dimensionality of the cavity, thereby reducing the mode volume, leads to even higher coupling rates. This idea is followed in the research area of superconducting *circuit* QED. Here, the atom is replaced by a superconducting circuit with a discrete energy spectrum and the three-dimensional cavity by a quasi-one-dimensional microwave resonator with very strongly reduced mode volume. This idea was presented in Ref. [27] and experimentally implemented in 2004 [28]. On the one hand, by reduction of the of the mode volume the electrical field per photon could be increased by a factor of $\sim 10^3$. On the other hand, the electric dipole moment of the artificial atom could be increased to a value exceeding the one of Rydberg atoms by a factor of 10^2 to 10^3. An important advantage of circuit QED systems is their high design flexibility and wide tunability of system parameters such as the resonator frequency, the resonator loss rate, the qubits transition frequency and the coupling constant. In this way circuit QED allows to study light-matter interaction with an unprecedented level of control.

Regarding future applications of qubits such as their usage for analogue or digital quantum simulation a few fundamental techniques have to be established. To this end, time-domain [29] and frequency-domain [30] measurements were realized by entering the dispersive limit, where qubit and cavity are detuned. Moreover, the interaction of the resonator-qubit system was investigated in detail [31–33].

Future digital quantum simulators most likely consist of a large number of subsystems interacting with each other. Dealing with an increased number of subsystems, one has to deal with the problem of directing and storing of quantum signals. Addressing these problems, the coupling of qubits via a cavity bus was realized [34, 35] as well as coupling two qubits via a third one [36]. In the same breath the controllable coupling between different qubits needs to be mentioned [37, 38] which culminated in a controllable entanglement of even three qubit states [39] or resonators [40].

So far, the coupling of two individual components, e. g., a qubit and a resonator, is performed in the resonant regime. To avoid decoherence effects due to the qubit a dispersively coupled qubit is favorable. One idea is to use the resonators as the memory unit while the qubit only serves as a coupling unit, providing the transfer of the state between the detuned resonators [41, 42]. In a second ansatz, the qubit is working in the dispersive limit. Here, it only controls the coupling between the two resonators. An extraordinary large qubit decoherence time is not necessary. A device, fulfilling these requirements was first introduced by M. Mariantoni [43] and was called *quantum switch*. Later, decoherence channels of the system were investigated explicitly [44].

The quantum switch consists of two resonators coupled directly and via a qubit. In the dispersive regime, the qubit mediates a dynamic second order interaction with its sign depending on the qubit state. The parameters of the qubit can be tuned externally such that the magnitude of the dynamic coupling is equal to the first order geometric coupling of the two resonators. Hence, depending on the qubit state, the interaction of the resonators is off or on. Here, in the off state the geometric and dynamic coupling

compensate each other.

Using a quantum system as mediator provides the luxury of using the qubit for further experiments such as the creation of a superposition state between the resonators $(|1\rangle_A|0\rangle_B + |0\rangle_A|1\rangle_B)/\sqrt{2}$ or tripartite entangled Greenberg-Horne-Zeilinger (GHZ) states $(|g\rangle|1\rangle_A|0\rangle_B + |e\rangle|0\rangle_A|1\rangle_B)/\sqrt{2}$ [45]. Here, $|n\rangle_{A(B)}$ denotes n Fock states in resonator A (B). Although the qubit is used to create these states, the resonators and the qubit are off resonant and the quantum switch is working in the dispersive limit. Ideas for fascinating experiments which can be performed using the quantum switch will be presented in chapter 6.

This work presents the first realization of a quantum switch consisting of two microwave resonators with resonance frequencies in the GHz-regime coupled to one flux qubit. Using different fabrication techniques, the resonators and the qubit are fabricated at the Walther-Meißner-Institut. Since the qubit is working off-resonantly, decoherence effects play a minor role. Nevertheless, the requirements regarding the key parameters of the quantum switch and the fabrication of its single components are demanding. Furthermore, the characterization of the device requires a complex cryogenic setup including high stability of the applied magnetic flux and temperature. To meet these requirements, an existing dilution refrigerator had to be rebuilt within this thesis.

Outline of the thesis

The thesis is structured as follows. For a fundamental understanding of the quantum switch, the single components must be well understood. Starting with a brief overview of the physics of Josephson junctions in section 2.1, superconducting quantum interference devices (SQUIDs) and qubits are discussed in the following sections. Two different qubit layouts are used within this work, a flux qubit with three Josephson junctions and a flux qubit with four Josephson junctions. Starting with the three-Josephson-junction case, the advantage of the four-Josephson-junction design is illustrated in subsection 2.4.2. Experimentally, the four-Josephson-junction qubit is well known, nevertheless a theoretical overview is useful. As the fabrication of a four-Josephson-junction qubit is less reproducible than the fabrication of the three-Josephson-junction qubit, the quantum switch is realized using a three-Josephson-junction flux qubit. However, the dc-SQUID measurements shown in section 4.3 are performed with four-Josephson-junction qubits.

Chapter 3 gives an introduction to circuit QED and two-resonator circuit QED. The latter is introduced by a detailed derivation of the quantum switch and a discussion of its critical parameters.

A major part of the experimental work was focused on the optimization and fabrication of the measured devices. Therefore, chapter 4 gives an overview of the experimental techniques such as fabrication processes, see section 4.1, and measurements setups, see sections 4.2 and 4.4. Important for future works is the characterization of the four-Josephson-junction qubit in chapter 4.3. Some ideas improving the quantum switch using four-Josephson-junction qubits will be shown in chapter 6.

For measurements on the quantum switch, an existing 30 mK dilution unit had to be upgraded. A rough overview of the used setup and about some critical components is given in 4.4. Since only small parts of the modified setup is used for measurements on the quantum switch, in addition an overview on the complete systems is presented in appendix D.1.

The results of the quantum switch measurements are presented in chapter 5. After a short overview of the characterization of a two-resonator sample, the qubit parameters and the coupling strengths are presented in subsection 5.3.2. These values are used to determine the theoretical prediction of the quantum switch and section 5.4 shows good agreement between prediction and experimental data. The quality of the switch is presented and discussed in subsection 5.4.3.

After a short summery about the results, some ideas of interesting experiments using this device will be given in the outlook in chapter 6.

Chapter 2

Superconducting Circuits for Quantum Information Processing

This chapter gives the theoretical background for the elemental building blocks of the quantum switch, namely Josephson-junction-based devices and microwave resonators. The Josephson junctions explained in section 2.1 are the basic elements for the dc-SQUID, the three-Josephson-junction, and the four-Josephson-junction qubit discussed in the subsequent sections.

2.1 Josephson junctions

In 1962, Brian D. Josephson published an article [46] which provided the basis for the most important component in circuit-QED, the Josephson junction [47]. A Josephson junction consists of two weakly coupled superconductors, e.g., two superconductors separated by a thin insulating barrier, see Fig. 2.1. The Cooper pairs of each superconductor condensed into the same quantum state can be described by the macroscopic wave function $|\psi_{\mathrm{L/R}}| \exp(i\phi_{\mathrm{L/R}})$. The tunneling current of the Cooper pairs through the thin barrier is

$$I_{\mathrm{s}} = I_{\mathrm{c}} \sin(\phi) \qquad \text{(first Josephson relation)}, \tag{2.1}$$

where ϕ is defined as the phase difference $\phi_{\mathrm{L}} - \phi_{\mathrm{R}}$ and the critical current I_{c} is the maximum supercurrent flowing through the junction. The wavefunctions $|\Psi_{\mathrm{L}}\rangle$ and $|\Psi_{\mathrm{R}}\rangle$ are coupled via the tunneling of Cooper pairs through the barrier. The related coupling energy is the Josephson energy $E_{\mathrm{J}} = I_{\mathrm{c}}\Phi_0/(2\pi)$. Here, the magnetic flux quantum is defined as $\Phi_0 = h/(2e)$ [48, 49]. Applying a voltage across the junction, the time

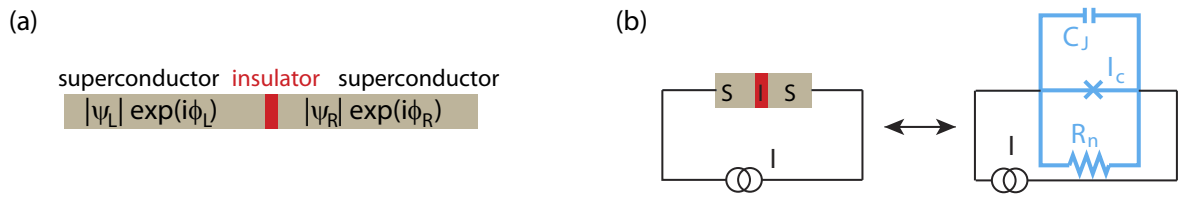

Figure 2.1: (a) A Josephson junction consists of two superconductors separated by a thin insulating layer (red). (b) RCSJ-model of a current biased Josephson junction where the junction is represented by the capacitance C_{J}, the critical current I_{c}, and the normal resistance R_{n}.

derivative of the phase is given as

$$\frac{\mathrm{d}\phi}{\mathrm{d}t} = \frac{2\pi}{\Phi_0} V \qquad \text{(second Josephson relation)}. \tag{2.2}$$

From the definition of an inductance $L = V/(\mathrm{d}I/\mathrm{d}t)$, one finds the inductance of a Josephson junction to be $L_\mathrm{J} = \Phi_0/(2\pi I_\mathrm{c}\cos(\phi))$. This Josephson inductance is nonlinear and can even become negative. It is the basis for the nonlinear quantum systems discussed later.

A real Josephson junction can be modeled with an equivalent circuit, containing the self-capacitance C_J, a resistance R_n and an ideal Josephson junction, see Fig. 2.1(b). By applying Kirchhof's law and using the second Josephson equation, one obtains an equation of motion of the phase difference ϕ,

$$\frac{\Phi_0}{2\pi} C_\mathrm{J} \ddot{\phi} + \frac{\Phi_0}{2\pi}\frac{1}{R_\mathrm{n}}\dot{\phi} = I - I_\mathrm{c}\sin(\phi) = -\frac{2\pi}{\Phi_0}\frac{\partial U_\mathrm{J}}{\partial \phi}, \tag{2.3}$$

with the *tilted washboard potential*

$$U_\mathrm{J} = E_\mathrm{J}\left(1 - \cos(\phi) - \frac{I}{I_\mathrm{c}}\phi\right).$$

More details on the washboard potential and the RCSJ model can be found in Ref. [50].

It is important to note that in the treatment given above the phase difference ϕ is considered a classical variable and the equation of motion (2.3) corresponds to that of a classical particle in the tilted washboard potential. The reason is that in most Josephson junctions the Josephson coupling energy E_J (can be view as the potential energy) is much bigger than the charging energy $E_\mathrm{C} = e^2/(2C_\mathrm{J})$ of an elementary charge on the junction capacitance (can be viewed as the kinetic energy). However, this is no longer the case when going to junctions with small junction area A. Here, the coupling energy E_J, which scales proportional to A_JJ, becomes small, while the charging energy E_C, which scales proportional to $1/A$ becomes big. In this case we have to do a full quantum treatment including the effect of the small junction capacitance (cf. section 2.3).

2.2 Dc-SQUID

In this section, basic theoretical aspects about the **d**irect-**c**urrent **s**uperconducting **q**uantum **i**nterference **d**evice (dc-SQUID) [51] are introduced. Today, SQUIDs are well-known devices which are discussed in detail in Refs. [47, 50, 52]. The dc-SQUID is not the primary subject of this thesis but used to characterize the qubits. Therefore, the introduction will be focused on the main parameters used later.

A dc-SQUID consists of two, here assumed to be identical, Josephson junctions intersecting a superconducting loop of inductance L where each junction has a critical current I_c. The loop can be biased with a current I_sq, see Figs. 2.2(a) and (b). In the absence of an external magnetic field the maximum applied zero-voltage current I_m is $2I_\mathrm{c}$.

When the applied bias current is increased to $I_\mathrm{sq} > I_\mathrm{m}$, the SQUID switches into the voltage state and a finite voltage V_sq is observed. A typical current-voltage characteristic is sketched in Fig. 2.2(c). The gap voltage $V_\mathrm{g} = 2\Delta_\mathrm{s}/e$ ($2\Delta_\mathrm{s}$ denotes the superconduct-

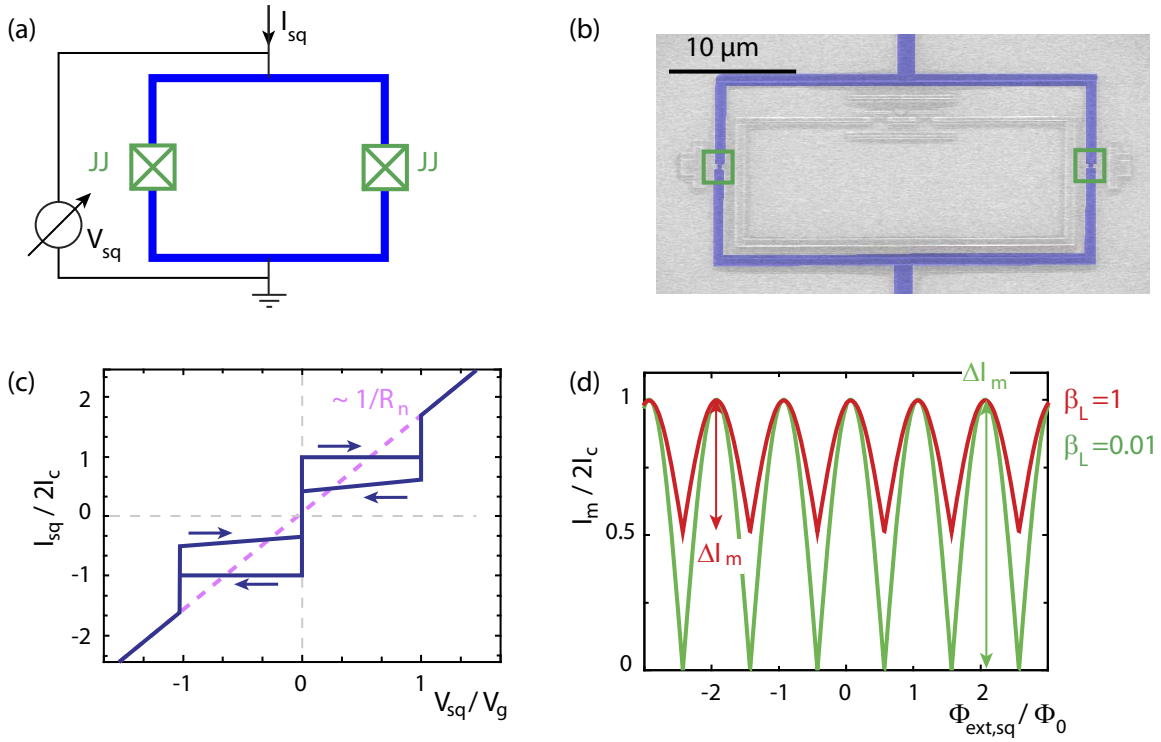

Figure 2.2: dc SQUID: (a) Schematic of a current biased dc-SQUID. The Josephson junctions (green) are symbolized with boxed crosses. By biasing the SQUID with a bias current I_{sq} the voltage V_{sq} is measured. (b) False-colored scanning electron micrograph of a sample. The dc-SQUID is colored blue and the Josephson junctions are highlighted with green boxes. (c) Schematic current-voltage characteristics for a SQUID. For $I_{\mathrm{sq}} < 2I_{\mathrm{c}}$ the voltage across the SQUID is zero. At $I_{\mathrm{sq}} = 2I_{\mathrm{c}}$ the voltage drops to the a finite value, V_{g}. With increasing bias current, the current-voltage characteristics follows the normal resistance R_{n} slope. (d) Two calculated, typical $I_{\mathrm{m}}(\Phi_{\mathrm{ext}})$ characteristics for different values of β_{L}.

ing energy gap), and the critical current itself are related by the Ambegaokar-Baratoff relation [53]

$$2I_{\mathrm{c}} = \frac{\pi}{4}\frac{V_{\mathrm{g}}}{R_{\mathrm{n}}}.$$

The normal resistance R_{n} appearing for $I_{\mathrm{sq}} > 2I_{\mathrm{c}}$ is modeled as an ohmic resistor in the RCSJ model. The hysteresis in Fig. 2.2(c) strongly depends on the junction capacitance C_{J} where the Steward-McCumber parameter [54, 55]

$$\beta_{\mathrm{c}} = 2\pi I_{\mathrm{c}} R_{\mathrm{n}}^2 C_{\mathrm{J}}/\Phi_0$$

relates the quantities I_{c}, R_{n} and C_{J}.

A magnetic flux $\Phi_{\mathrm{ext,sq}}$ can be induced into the SQUID loop and influences I_{m}. For small SQUID loops with negligible loop inductances I_{m} reads

$$I_{\mathrm{m}}(\Phi_{\mathrm{ext,sq}}) = 2I_{\mathrm{c}}|\sin(\pi\Phi_{\mathrm{ext,sq}}/\Phi_0)|, \tag{2.4}$$

see Fig. 2.2(d). The reason for the periodicity in Φ_0 lies in the fluxiod quantization of the

flux penetrating a superconducting loop [48, 49]. Equation (2.4) only holds if the loop inductance in negligible or

$$\beta_{\mathrm{L}} = 2LI_{\mathrm{c}}/\Phi_0 \ll 1.$$

Otherwise the modulation depth $\Delta I_{\mathrm{m}}/(2I_{\mathrm{c}})$ with $\Delta I_{\mathrm{m}} = 2I_{\mathrm{c}} - I_{\mathrm{m}}(\Phi_{\mathrm{ext,sq}} = \Phi_0/2)$ is reduced. For $\beta_{\mathrm{L}} = 1$ the modulation depth is approximately 0.5 and increases with decreasing β_{L}.

The oscillating critical current $I_{\mathrm{m}}(\Phi_{\mathrm{ext,sq}})$ is a useful observable to detect flux changes in the loop in the submilli-Φ_0 range. Therefore, the dc-SQUID is used to detect the magnetic field induced by a qubit as discussed in section 4.3.

2.3 Quantum mechanical treatment of charge and flux

In the discussion in section 2.2, the phase ϕ or equivalently the flux $\Phi = (\Phi_0/2\pi)\phi$ have been treated as classical variable. The charging energy was neglected. For small area Josephson junctions as used in qubits this is no longer possible and we have to do a full quantum treatment including the charge degree of freedom. Following the concept of canonical quantization we replace the classical variables flux Φ and charge Q by the respective operators $\hat{\Phi}$ and $\hat{Q}$. From the quantum mechanical point of view, $\hat{\Phi}$ and $\hat{Q}$ are conjugate observables fulfilling the commutation relation

$$[\hat{Q},\hat{\Phi}] = i\hbar.$$

As in general in quantum mechanics the operators are represented in their conjugate relations as

$$\hat{Q} = -i\hbar\frac{\partial}{\partial\phi} \quad \text{and} \quad \hat{\Phi} = i\hbar\frac{\partial}{\partial Q}.$$

The uncertainty relation of their eigenvalues reads as

$$\Delta Q \Delta\Phi \geq \frac{\hbar}{2}.$$

2.4 Superconducting persistent current qubits

A superconducting Josephson qubit can be understood as a nonlinear resonator formed by the Josephson inductance and its junction capacitance. The nonlinearity is crucial to obtain an anharmonicity in the system. An effective two state system can be considered only if the transition frequency between the two lowest states, $\omega_{\mathrm{Q}} = (E_{|e\rangle} - E_{|g\rangle})/\hbar$ strongly differs from the transition frequency between the excited state $|e\rangle$ and the third level $|f\rangle$. Depending on the design and area of the Josephson junctions, different superconducting qubits can be distinguished. The phase drop at the Josephson junction $\hat{\phi}$ and the charge $\hat{Q}$ on the capacitor are the canonically conjugated variables. If one or more Josephson junctions are implemented in a superconducting ring, the phase is often substituted by the total flux $\hat{\Phi}$ penetrating the loop. In general, one of the variables (flux or charge) is what is called a good quantum number. Depending the ratio of the qubit energy scales $E_{\mathrm{J}}/E_{\mathrm{C}}$ either charge or flux is well defined while, fulfilling the uncertainty principle, the other variable is diffused. A large zoo of superconducting qubits based

on Josephson junctions is known today. The most prominent representatives are shortly pointed out in the following.

Cooper-pair box: A Cooper-pair box can be considered as a superconducting island connected to a much larger reservoir of Cooper pairs via in general two Josephson junctions [56–58]. A capacitively coupled gate voltage controls the number of Cooper pairs on that island while an external flux bias controls the qubit transition frequency. An odd or even number of Cooper pairs on the island represents the ground and excited state of the qubit. If $E_\mathrm{J}/E_\mathrm{C} \ll 1$ the Cooper-pair box is called *charge qubit* as its eigenstates are very close to being charge states.

Transmon qubits: A transmon qubit [59] consists of a superconducting island connected to a reservoir of Cooper pairs. An additional shunting capacitor is placed in parallel to the Josephson junctions to suppress charge noise. Hence, $E_\mathrm{J}/E_\mathrm{C}$ increases and the anharmonicity is decreased and the third qubit level $|f\rangle$ has to be considered, see, e. g., Ref. [60]. The eigenstates of a transmon are superpositions of many charge states. E_J dominates the properties of the qubit. It has been shown that with increasing $E_\mathrm{J}/E_\mathrm{C}$ from ≈ 10 to ≈ 30, charge dispersion is decreased from 74 MHz to 0.8 MHz [61]. Today the transmon qubit is one of the most used superconducting qubits due to its robustness against fabrication parameters.

Flux qubits: In general, a flux qubit consists of a superconducting loop and three or more Josephson junctions [62, 63]. To obtain a two level system, the balancing of E_J and E_C is a fundamental fabrication issue. The quantum variable is the magnetic flux threading the loop. The two eigenstates correspond to the clockwise or counter-clockwise screening current flowing in the loop which is caused by the magnetic field. In the following sections the layouts of the three-Josephson-junction qubit and the four-Josephson-junction qubit will be discussed in detail.

Phase qubits: In contrast to the charge qubit, the Josephson junction of the phase qubit is relatively large. A bias current is necessary to produce the required nonlinearity. The quantum variable is the phase difference across the junction [64–66].

A detailed overview of the different superconducting qubits can be found in review articles as in Ref. [67, 68].

2.4.1 Three-Josephson-junction flux qubit

The fundamental component of the quantum switch is the superconducting *flux qubit* or *persistent current qubit* [62, 63]. It consists of a macroscopic superconducting ring interrupted by three or more Josephson junctions, see Fig. 2.3(a). Since the loop inductance L_L is designed to be small compared to the Josephson inductance L_J of the junctions, L_L is neglected. Therefore, only the two energy scales E_J and E_C determine the quantum mechanical behavior. In the flux limit $E_\mathrm{J} > E_\mathrm{C}$, the good quantum variable is the phase while the charge is fluctuating. The Josephson energy of two of the three junctions is equal. It is reduced by a factor of α for the third Josephson junction. Due to fluxoid quantization, the sum of the phase-drops across the three junctions and the phase shift caused by the external flux $\Phi_\mathrm{ext} = f\Phi_0$ penetrating the loop must be an integer multiple of 2π. Here f ist the so-called frustration. According to the Josephson relation a finite phase drop across the junctions is related to a finite supercurrent circulating in the ring. This current is called *persistent current*. That is why the qubit is called persistent flux qubit. Depending on the external flux the persistent current is flowing clock- or coun-

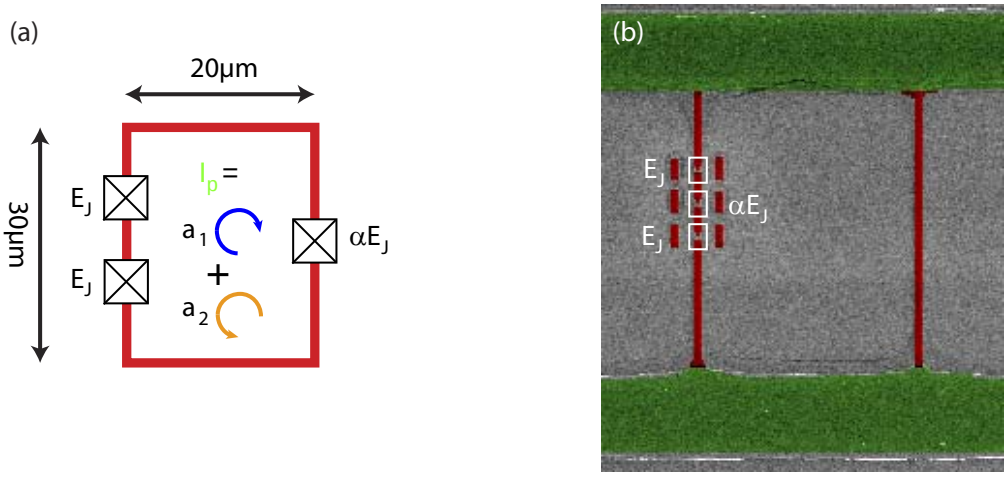

Figure 2.3: (a) Sketch of a three-Josephson-junction qubit. The current can flow clockwise or counter-clockwise, depending on the magnetic field penetrating the loop. (b) False-color image of the qubit (red) implemented between two resonator lines (green). This configuration will be used later for the quantum switch.

terclockwise. The direction defines the states $|L\rangle$ and $|R\rangle$. At $\Phi_{\text{ext}} = \Phi_0/2$ the energies of the states degenerate, resulting in the notation degeneracy point for this flux bias. However, the degeneracy is lifted by a finite tunnel coupling between the states $|L\rangle$ and $|R\rangle$, resulting in a symmetric and anti-symmetric superposition state $|g\rangle$ and $|e\rangle$. At the degeneracy point these two states are separated by the tunnel coupling δ_{Q}.

Mathematically spoken, the Josephson energy of each junction is $E_{\text{J},n}(1 - \cos\phi_n)$. Together with the fluxoid quantization, see Fig. 2.3(a), the potential energy of a three-Josephson-junction flux qubit is given by only two free variables can be expressed

$$U = E_{\text{J}}[2 + \alpha - \cos\phi_1 - \cos\phi_2 - \alpha\cos(2\pi f + \phi_1 - \phi_2)]. \tag{2.5}$$

Due to its periodicity unit cells are defined by connecting the maxima of the potential. Figure. 2.4(a) shows the potential energy at the degeneracy point. The red dashed box defines a unit cell. Two possible saddle point connections can be established between the minima L_{ij} and R_{ij}. An intracell connection is symbolized by the yellow solid line (tunneling between L_{00} and R_{00}) and an intercell tunneling is symbolized by the yellow dashed line (tunneling between R_{01} and L_{00}). The set of all L minima is represented by the qubit state $|L\rangle$ and the set of all R minima to $|R\rangle$. While the barrier in the intercell coupling is too high, the intracell tunneling results in a coupling of states $|L\rangle$ and $|R\rangle$, see Fig. 2.4(b).The finite tunnel coupling of the states $|L\rangle$ and $|R\rangle$, which are degenerate for $f = 1/2$, causes a lifting of the degeneracy and an anti-crossing of the levels. The resulting symmetric and anti-symmetric superposition states are separated by the tunneling coupling δ_{Q} at the degeneracy point $f = 1/2$ and form the ground state $|g\rangle$ and the excited state $|e\rangle$. The height of the barrier of the double well potential depends on α. For $\alpha < 0.5$, the barrier, and hence, the double well potential vanishes. For $\alpha > 0.75$, the barrier becomes too high and the tunnel coupling is reduced to too small values $\delta_{\text{Q}} < k_{\text{B}}T$. The optimal value for α in case is a three-Josephson-junction qubit is 0.7.

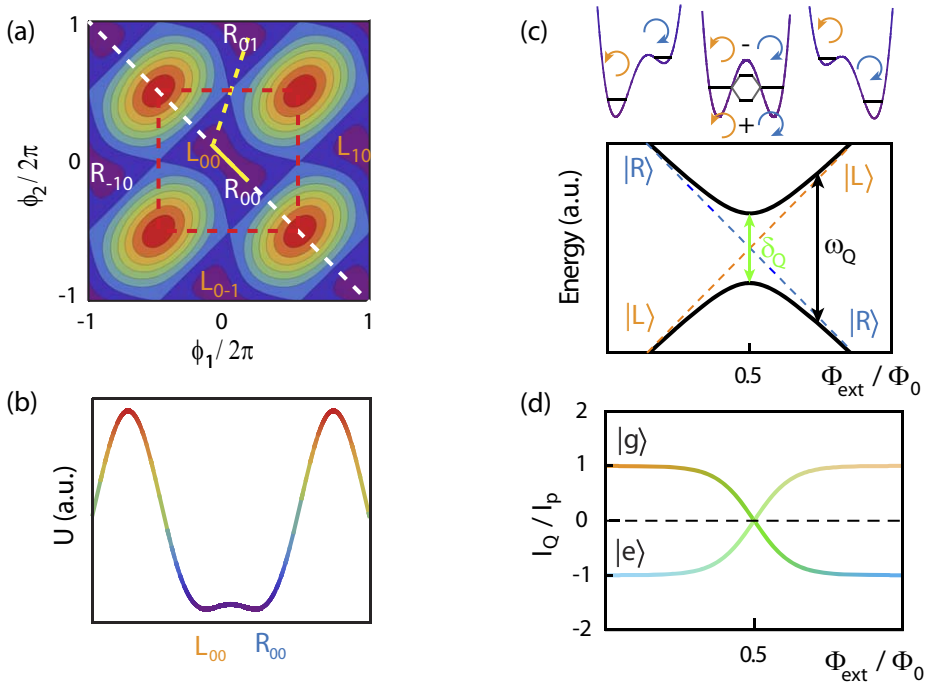

Figure 2.4: (a) Two-dimensional potential of a three-Josephson-junction flux qubit at $f = 0.5$. A unit cell, red dashed box, includes two minima (here L_{00}, and R_{00}) and one maximum. A cross-section along the dashed white line is shown in (b). The typical double well potential is clearly visible. (c) Qubit's energy spectrum versus frustration Φ_{ext}/Φ_0. Depending on the external flux, a left or a right circulating current corresponds to the ground or excited state. Near the degeneracy point, the states couple and an anticrossing results in the two levels of the flux qubit. The shape of the double well is illustrated in the sketch of the potential energy (along the dashed line) above the diagram. (d) Shows the quantum mechanical expectation value of the qubit current $I_Q = \langle I_p \hat{\sigma}_z \rangle = \partial E_i / \partial \Phi_{\text{ext}}$ in the loop.

Near the degeneracy point, the Hamiltonian of a flux qubit reflects the coupling of the states $|L\rangle$ and $|R\rangle$ via a tunneling matrix element proportional to δ_Q as

$$\hat{\bar{H}}_Q = T + U = \frac{\varepsilon}{2}\hat{\bar{\sigma}}_z + \frac{\delta_Q}{2}\hat{\bar{\sigma}}_x, \tag{2.6}$$

where $\hat{\bar{\sigma}}_{x,z}$ are Pauli operators for a spin 1/2 system in the diabatic basis consisting of the persistent-current eigenstates $|L\rangle$ and $|R\rangle$. These eigenstates of $\varepsilon\hat{\bar{\sigma}}_z/2$ are coupled via the coupling strength δ_Q. While the gap energy δ_Q is a design parameter and flux independent, the energy bias ε is given by the relation:

$$\varepsilon = \varepsilon(\Phi_{\text{ext}}) = 2\left(\Phi_{\text{ext}} - \frac{2n-1}{2}\Phi_0\right)\left.\frac{\partial U}{\partial \Phi_{\text{ext}}}\right|_{\phi_1=-\phi_2} = 2I_p\left(\Phi_{\text{ext}} - \frac{2n-1}{2}\Phi_0\right) \qquad (n \in \mathbb{N}). \tag{2.7}$$

As a direct consequence of the derivative of Eq. (2.5), the persistent current I_p is defined as

$$I_p = I_c\sqrt{1 - \left(\frac{1}{2\alpha}\right)^2}. \tag{2.8}$$

For the optimal value of $\alpha = 0.7$, the persistent current is approximately $0.7I_c$ or approximately αI_c

Figure 2.4(c) shows the two energy levels of the Hamiltonian (2.6) and the related potential shape close to the degeneracy point ($f = 0.5$). The anticrossing at the degeneracy point results in a splitting of the energy levels by the gap energy δ_Q. The new eigenstates $|g\rangle$ and $|e\rangle$ are symmetric and antisymmetric superpositions of $|L\rangle$ and $|R\rangle$. Rotating the Hamiltonian (2.6) into the qubits eigenbasis by the mixing angle $\theta = \arctan(\delta_Q/\varepsilon)$, gives the flux dependent energy difference of the eigenstates

$$E_Q = \hbar\omega_Q = \sqrt{\delta_Q^2 + \varepsilon(\Phi_{ext})^2} \tag{2.9}$$

and the Hamiltonian reads

$$\hat{H}_Q = \frac{\hbar\omega_Q}{2}\hat{\sigma}_z. \tag{2.10}$$

ω_Q is called the qubit transition frequency and has a hyperbolic dependence on the external applied flux Φ_{ext}. Depending on the qubit state $|g\rangle$ or $|e\rangle$ at a given flux value, the persistent current is circulating clock- or counter-clockwise. Figure 2.4(d) shows the qubit current I_Q as a function of the external applied flux. For $\Phi_{ext} < 0.5\Phi_0$, the ground state is represented by a counterclockwise current which is reduced to zero at the degeneracy point. With further increasing external flux Φ_{ext} the ground state is now represented by a clockwise circulating current. As a consequence, by sweeping the flux adiabatically the change of the magnetic field caused by the change of the direction of the persistent current can be detected using a dc-SQUID, see chapter 4.3.

2.4.2 Four-Josephson-junction flux qubit

A persistent current qubit can also be realized using four Josephson junctions. Experimentally, this configuration shows better coherence times than the three-Josephson-junction configuration [69–71]. The reason for this lies in the nature of a Josephson junction and on the fact that it is impossible to fabricate a real three-Josephson junction flux qubit because of topological limitations. The latter will become clear in subsection 4.1.3 where also the differences of the two designs will be depicted. At this point it should only be mentioned that a three-Josephson-junction qubit has an even number of junctions. Despite the three well defined junctions the others are relatively large in size which comes along with a large critical current. The large critical current leads to a small junction inductance and results in a small and negligible phase drop over the junction. Thus, they can be neglected in theory. Despite the fact that the origin of decoherence is rather complicated and not yet completely understood, one of the dominant sources seems to be related to defects in the oxide layer forming the tunnel barrier of the Josephson junctions. By decreasing the fourth Josephson junction the amount of defects is reduced which results in better coherence.

The four-Josephson-junction flux qubit consists also of a superconducting loop with four Josephson junctions. Three junctions have the same size and again the size of one junction is reduced by a factor of α. As in the three-junction case, the total potential energy is the sum of the single junctions' potential energies. Taking into account the flux

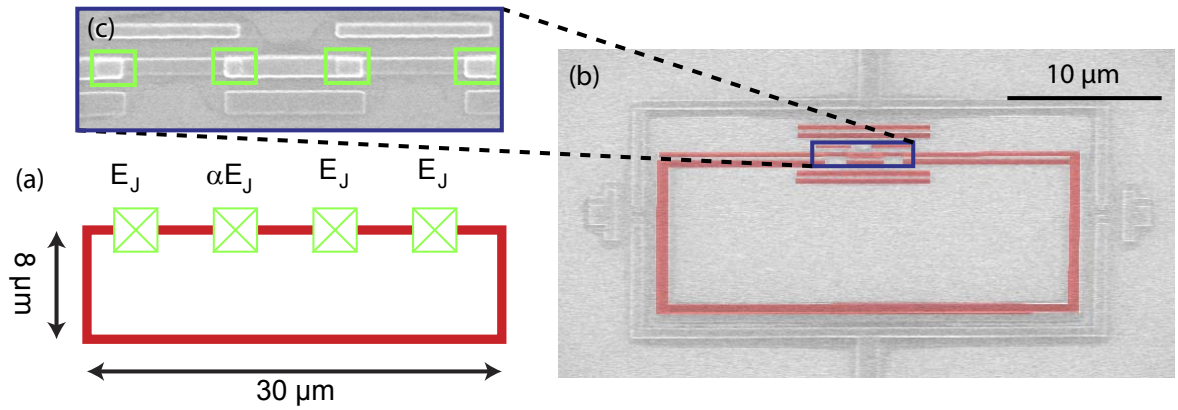

Figure 2.5: (a) Sketch of a four-Josephson-junction qubit. Three junctions have the same size while the fourth junction is reduced by a factor of $\alpha = 0.5$ (b) False-color scanning electron micrograph of the qubit (red). (c) Enlargement of the area marked by the blue box in (b)

quantization condition, it can be written as

$$U = E_\mathrm{J}[3 + \alpha - \cos\phi_1 - \cos\phi_2 - \cos\phi_3 - \alpha\cos(2\pi f + \phi_1 - \phi_2 - \phi_3)]. \tag{2.11}$$

Due to the three degrees of freedom it is hard to visualize the potential. Three-dimensional contour plots are shown for $U = 0.95\,E_\mathrm{J}$, $U = 1.03\,E_\mathrm{J}$ and $U = 1.5\,E_\mathrm{J}$ in Fig. 2.6. The contours at low energy show only two tiny spheres which are growing to a bone-like shape along the $\phi_1 = -\phi_2 = -\phi_3$ axis. A cross-section along the $\phi_1 = -\phi_2 = -\phi_3$ axis shows a similar double well potential as in the three-Josephson-junction case, see Fig. 2.6(d). Using this knowledge, the four-Josephson-junction qubit can be treated exactly such as the three junction qubit. As the double well barrier of a three-Josephson-junction qubit, the barrier of the double well of a four-Josephson-junction qubit depends on α. For $\alpha < 0.3$, the barrier of the double well potential is reduced to zero and for $\alpha > 0.8$ the barrier becomes to high and an effizient coupling between the clockwise and counterclockwise circulating current states is suppressed. The optimal value for the reduced Josephson junction is $\alpha = 0.5$.

The potential (2.11) results in a sightly different expression for the persistent current I_p. Using relation (2.7) at $\phi_1 = -\phi_2 = -\phi_3$, the persistent current is

$$I_\mathrm{p} = I_\mathrm{c}\alpha\left(\frac{3}{2}\left(\frac{3\alpha-1}{\alpha}\right)^{1/2} - \frac{1}{2}\left(\frac{3\alpha-1}{\alpha}\right)^{3/2}\right). \tag{2.12}$$

Although this relation seems to differ from Eq. (2.8) for $\alpha = 0.5$ the persistent current is $I_\mathrm{p} = 0.5I_\mathrm{c} = \alpha I_\mathrm{c}$.

2.5 Two coupled resonators

Apart from the qubit with its anharmonic level structure, the other components of the quantum switch are two coupled resonators and can be described as two coupled quantum

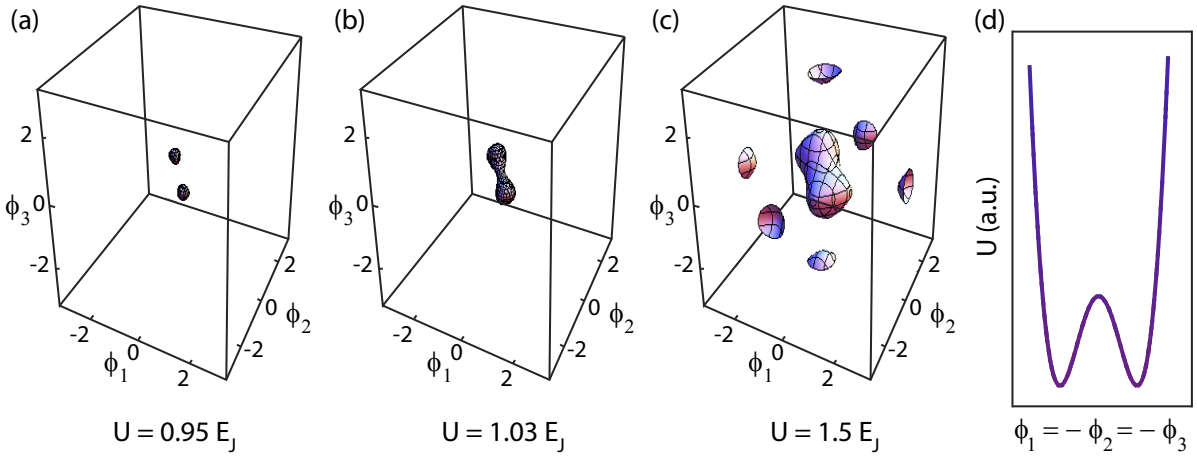

Figure 2.6: Contour plots of the potential energy of a four-Josephson-junction qubit ($f = 0.5$, $\alpha = 0.5$) for $0.95E_\mathrm{J}$ (a), $1.03E_\mathrm{J}$ (b) and $1.5E_\mathrm{J}$(c). The two tiny spheres in (a) are located at the two minima in the potential. A cross section along $\phi_1 = -\phi_2 = -\phi_3$ gives again a double well potential (d) as in the three-Josephson-junction case.

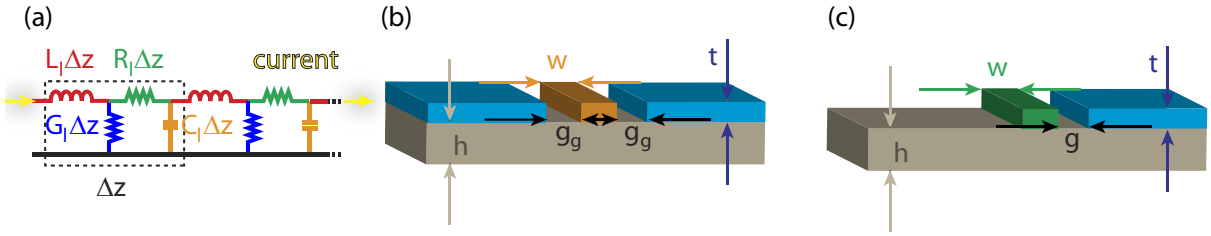

Figure 2.7: (a) Model of a transmission line. Each element of length Δz is modeled by a resistance per unit length R_l and an inductance per unit length L_l. The connection to ground is substituted by a conductance per unit length G_l and a shunt capacitance per unit length C_l. Sketch of a coplanar waveguide (b) and coplanar stripline (c). The layout parameters as the width of the signal line w, the gap between line and groundplane g_g and the thicknesses of the conducting material t and the substrate h influence the microwave properties such as the phase velocity v_{Ph} or the impedance Z_0.

harmonic oscillators. They are well known and studied in detail in textbooks, e. g., Ref [72]. This section will give an overview of the most important parameters. For a detailed description of microwave resonators, the author refers to Refs. [73–75]. A short excursion to transmission line theory will help to understand the technical point of designing two microwave resonators on a chip.

2.5.1 Transmission line theory in a nutshell

Harmonic oscillators can be realized using different kind of physical systems. Transmission line theory describes the wave propagation in waveguides such as microwave tubes, preferable for low frequencies, hollow-pipe waveguides for higher frequencies and surface waveguides. Various geometries of surface waveguides are well established such as microstrip transmission lines, coplanar waveguide (CPW) lines and coplanar stripline (CSL) designs. The two resonators are designed in a CSL layout and the feedlines in a CPW design [sketched in Figs. 2.7(b) and (c)]. Details about waveguides and waveguide designs are discussed in various textbooks as in Refs. [74–76].

In general, a transmission line can be modeled as an ideal signal line with a resistance per unit length R_l and an inductance per unit length L_l. A shunt conductance per unit length G_l and a shunt capacitance per unit length C_l connect the signal line with the ground, as sketched in Fig. 2.7(a). When using superconducting materials, G_l and R_l can be neglected and will not be considered in the following. L_l and C_l are defined by the layout of the network.

The phase velocity $v_{\mathrm{Ph}} = 1/\sqrt{L_l C_l} = c/\sqrt{\varepsilon_{\mathrm{eff}}}$ in a transmission line is the speed of light c reduced by the square root of the effective permittivity $\varepsilon_{\mathrm{eff}}$ [76]. The effective permittivity depends on the dielectric substrate and the geometry of the transmission line. Although v_{Ph} and $\varepsilon_{\mathrm{eff}}$ are defined by the geometric design, this design is chosen to fulfill another very important relation, namely reducing mismatches of the characteristic impedance between different parts of the network. The characteristic impedance of a transmission line Z_0 is given as $Z_0 = \sqrt{L_l/C_l}$. Microwave equipment is created with a characteristic impedance of $50\,\Omega$. To reduce reflections, the feed lines are realized in a $50\,\Omega$ matched coplanar waveguide design with a centerstrip and lateral groundplanes on

each side. The resonators themselves are in a coplanar stripline design. Reasons for this will be given later in subsection 5.1.1 where the layout of the chip will be discussed.

2.5.2 Coplanar stripline resonator

At the fundamental mode, the resonance frequency f_0 of a resonator with length l is given as $f_0 = v_{\mathrm{Ph}}/(2l)$. The wavelength λ_0 of the fundamental mode is $2l$. The general expression of the resonance frequency for the nth mode is

$$f_n = \frac{\omega_n}{2\pi} = \frac{nc}{2l\sqrt{\varepsilon_{\mathrm{eff}}}}.$$

The spectrum of each mode has a Lorentzian line shape where the full width at half maximum (FWHM) can be expressed by the cavity decay rate $\kappa_n = 2\pi \cdot \mathrm{FWHM}$. With these parameters, the quality factor Q_{L} is defined by $Q_{\mathrm{L}} = f_0/\mathrm{FWHM} = \omega_{\mathrm{R}}/\kappa$. Analyzing the measured Lorenzian gives only the *loaded* quality factor. It is a parallel combination of the *internal* and *external* quality factors [74]

$$\frac{1}{Q_{\mathrm{L}}} = \frac{1}{Q_{\mathrm{int}}} + \frac{1}{Q_{\mathrm{ext}}}. \tag{2.13}$$

$Q_{\mathrm{int}} = \omega_n RC$ and $Q_{\mathrm{ext}} = \omega_n R^* C/2$ [73] are the expressions of the individual parts, respectively. C is the total capacitance of the resonator, the contribution of the coupling capacitor is neglected as $C_\kappa \ll C$. R is the ohmic resistance and the resistance R^* is determined by the resistive load R_{L} and the coupling capacitor C_κ as $R^* = 1/(\omega_n^2 C_\kappa^2 R_{\mathrm{L}}) + R_{\mathrm{L}}$. This expression represents an internal impedance which is non-zero also in superconducting setups because of the presence of the $50\,\Omega$ resistive load and the comparably small coupling capacitance of a few fF. The capacity C is given by the layout and the used materials of the resonator. Formulas to calculate this value are given in Ref [76].

The quantum harmonic oscillator

In a first analysis, a distributed resonator can be modeled as a parallel lumped element circuit as described above. The classical Hamiltonian of such a system is

$$H_{LC} = \frac{Q^2}{2C} + \frac{\Phi^2}{2L} = \frac{1}{2}LI^2 + \frac{1}{2}CV^2. \tag{2.14}$$

By using $L = 1/(\omega_{\mathrm{R}}^2 C)$ and replacing the classical quantities, Q and Φ by the quantum mechanical operators $\hat{Q}$ and $\hat{\Phi}$, the quantum mechanical version of Eq. (2.14) reads

$$\hat{H}_{LC} = \frac{\hat{Q}^2}{2C} + \frac{1}{2}\omega_{\mathrm{R}}^2 C\hat{\Phi}^2. \tag{2.15}$$

By replacing these observables with the standard annihilation and creation operators

$$\hat{a} = \frac{1}{\sqrt{2C\hbar\omega_{\mathrm{R}}}}\left(\hat{Q} + iC\omega_{\mathrm{R}}\hat{\Phi}\right), \qquad \hat{a}^\dagger = \frac{1}{\sqrt{2C\hbar\omega_{\mathrm{R}}}}\left(\hat{Q} - iC\omega_{\mathrm{R}}\hat{\Phi}\right) \tag{2.16}$$

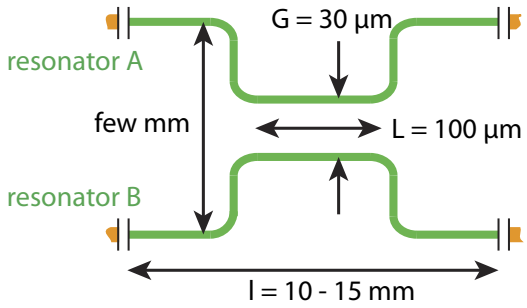

Figure 2.8: Schematic of the used two resonator design. In the center of the resonators at $l/2$ the otherwise well separated resonator lines are brought close together. This design only supports coupling of the fields where both resonators are close together. As the total length of the resonator l is much larger than the coupling length L one speaks of a point-like coupling.

Eq. (2.15) results in the standard one-dimensional quantum mechanical harmonic oscillator Hamiltonian

$$\hat{H}_{LC} = \hbar\omega_{\mathrm{R}} \left(\hat{a}^{\dagger}\hat{a} + \frac{1}{2} \right). \tag{2.17}$$

For the sake of completeness, the commutation relation $[\hat{a},\hat{a}^{\dagger}] = 1$ and the number operator $\hat{N} = \hat{a}^{\dagger}\hat{a}$ should be mentioned [77].

2.5.3 Two LC resonators

By adding a second resonator with the same eigenfrequency interacting with the first one, the system changes fundamentally. The Hamiltonian (2.17) is extended by a second harmonic oscillator and a coupling part. For coupling strength $g_{\mathrm{AB}} \ll \omega_{\mathrm{R}}$ the Hamiltonian reads

$$\hat{H}_{\mathrm{A,B}} = \hbar\omega_{\mathrm{R}} \left(\hat{a}^{\dagger}\hat{a} + \frac{1}{2} \right) + \hbar\omega_{\mathrm{R}} \left(\hat{b}^{\dagger}\hat{b} + \frac{1}{2} \right) + \hbar g_{\mathrm{AB}} \left(\hat{a}\hat{b}^{\dagger} + \hat{a}^{\dagger}\hat{b} \right). \tag{2.18}$$

Here, $\hat{a}$ ($\hat{b}$) and $\hat{a}^{\dagger}$ ($\hat{b}^{\dagger}$) are the annihilation and creation operators for resonator A (B). g_{AB} is the coupling rate that characterizes the coupling between the two resonators and depends, in the case of two CSL resonators on a single chip, on the geometry. The coupling coefficient of two resonators can be separated in a magnetic and a capacitive part $g_{\mathrm{AB}} = |g_{\mathrm{AB,m}} - g_{\mathrm{AB,c}}|$ [78]. As the geometry realized in this thesis only supports coupling of the fields at $l/2$, the coupling for every odd mode ($\lambda/2$, $3\lambda/2$, ...) is caused by a magnetic field coupling whereas the coupling of the even modes (λ, 2λ, ...) results from a capacitive coupling. These two coupling constants are in general not equal and labeled as $g_{\mathrm{AB,m}}$ and $g_{\mathrm{AB,c}}$ for an inductive and capacitive coupling, respectively. A schematic of the used design is depicted in Fig. 2.8.

Equation (2.18) can be diagonalized using the operators

$$\hat{c}_{\pm} = \frac{1}{\sqrt{2}} \left(\hat{a} \pm \hat{b} \right), \qquad \hat{c}_{\pm}^{\dagger} = \frac{1}{\sqrt{2}} \left(\hat{a}^{\dagger} \pm \hat{b}^{\dagger} \right) \tag{2.19}$$

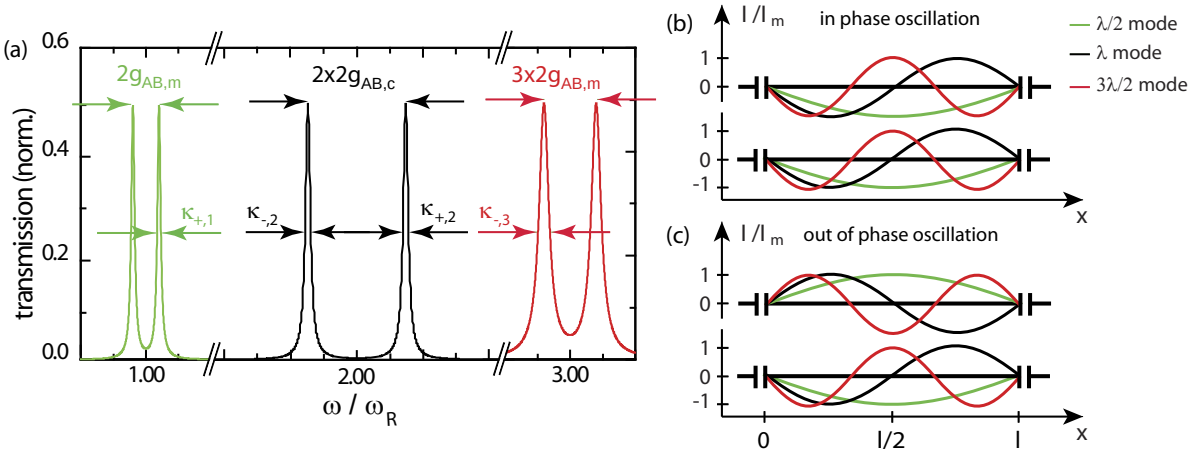

Figure 2.9: (a) Sketch of a calculated, normalized transmission spectrum of two coupled resonators for the fundamental and the two first harmonic modes. Close to the eigenfrequency ω_R the spectrum shows two peaks, one at $\omega_- = \omega_\mathrm{R} - g_\mathrm{AB,m}$ and one at $\omega_+ = \omega_\mathrm{R} + g_\mathrm{AB,m}$. Similar splitting occurs for higher harmonics. As (b) and (c) show, the current distribution for the $\lambda/2$ (fundamental at ω_R) and $3\lambda/2$ (second harmonic at $3\omega_\mathrm{R}$) is maximal at the center of the resonators. The current distribution of the λ mode is zero at $l/2$. The geometry of the sample investigated in this thesis only supports a coupling of the fields at $l/2$. Thus, a magnetic coupling of the $\lambda/2$ and $3\lambda/2$ and a capacitive coupling of the λ modes can be observed. The splitted eigenmodes oscillate in-phase at ω_- and out-of-phase at ω_+, respectively.

resulting in

$$\hat{H}_\mathrm{A,B} = \hbar(\omega_\mathrm{R} + g_\mathrm{AB})\left(\hat{c}_+^\dagger \hat{c}_+ + \frac{1}{2}\right) + \hbar(\omega_\mathrm{R} - g_\mathrm{AB})\left(\hat{c}_-^\dagger \hat{c}_- + \frac{1}{2}\right). \tag{2.20}$$

The result shows an oscillator-like behavior with two new eigenfrequencies. For the fundamental mode the capacitive coupling is neglected and the frequencies are $\omega_- = \omega_\mathrm{R} - g_\mathrm{AB,m}$ and $\omega_+ = \omega_\mathrm{R} + g_\mathrm{AB,m}$ which can be verified in transmission measurements. The lower eigenmode at the frequency ω_- is when the current distribution of both "single" resonators oscillate in phase [Fig. 2.9(b) and Fig. 2.10(a)] and the higher eigenmode at ω_+ shows an out-of-phase oscillation of the currents in the "single" resonators [Fig. 2.9(c) and Fig. 2.10(b)]. The out-of-phase oscillation causes a magnetic field gradient between the two lines. This field is not generated in the in-phase oscillating case, see Fig. 2.10.

Similar splittings occur at the higher harmonics. As the coupling of every even mode ($\lambda/2$, $3\lambda/2$, ...) is caused by a magnetic field due to the current antinode at $l/2$ the coupling constants for these higher harmonics are $g_\mathrm{AB,2n+1} = (2n+1)g_\mathrm{AB,m}$ for $n \in \mathbb{N}$. The coupling of the odd modes (λ, 2λ, ...) is caused by the electric field wich has an antinode at $l/2$. The coupling constants are here $g_\mathrm{AB,2n} = 2n g_\mathrm{AB,c}$ for $n \in \mathbb{N}$.

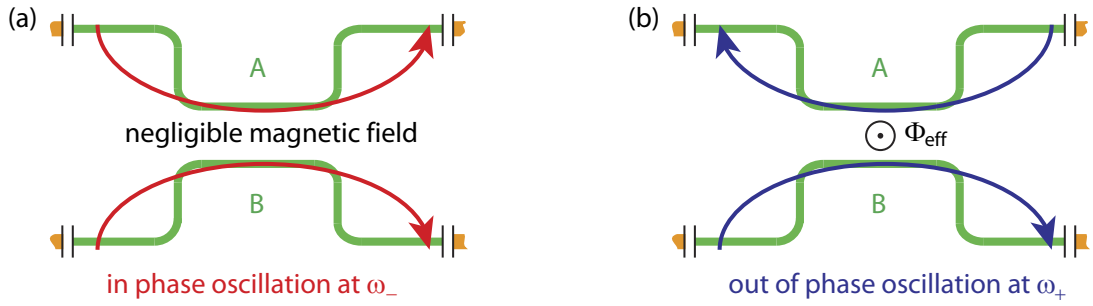

Figure 2.10: Schematic of the modes and their magnetic field. (a) The in-phase oscillating currents cause a negligible magnetic field between the two resonators at the center as the field generated by resonator A compensates the field generated by resonator B (b) The out-of-phase oscillating currents generate an effective magnetic field Φ_{eff} between the lines of the two resonators.

Chapter 3

Two-resonator circuit quantum electrodynamics

In the preceding chapter the components for the quantum switch - transmission line resonators and flux qubits - were introduced. In this chapter, the foundations of *circuit quantum electrodynamics* (circuit QED) are discussed briefly. In analogy to quantum optical cavity QED one resonator ("quantized light") is coupled to a Josephson-junction qubit ("matter"). Then, this scenario is extended to two-resonator circuit QED by taking the example of a flux mediating switchable coupling between two superconducting transmission line resonators.

3.1 Circuit quantum electrodynamics

The prototype system for studying light-matter interaction is a two-level atom interacting via a dipolar coupling with quantized electromagnetic modes of a cavity. Cavity QED systems often use Rydberg atoms or ions and couple these with three dimensional optical cavities. Systems in circuit QED consist of artificial atoms coupled to quasi-one-dimensional microwave transmission line resonators. In general, the artificial atoms are Josephson-junction based superconducting qubits. Recently, the term had been expanded to a semiconductor based system [79]. The general Hamiltonian of a qubit-resonator system, as it is depicted in Fig. 3.1, is given by

$$\hat{H} = \hbar\omega_{\mathrm{R}} \left(\hat{a}^{\dagger}\hat{a} + \frac{1}{2} \right) + \frac{\varepsilon}{2}\hat{\sigma}_{\mathrm{z}} + \frac{\delta_{\mathrm{Q}}}{2}\hat{\sigma}_{\mathrm{x}} + \hbar g\, \hat{\sigma}_{\mathrm{z}} \left(\hat{a}^{\dagger} + \hat{a} \right) + \hat{H}_{\gamma} + \hat{H}_{\kappa}. \tag{3.1}$$

The first term represents the energy of the quantized electromagnetic field stored in a resonator with the resonance frequency ω_{R} and the second and third term represent the qubit. The forth term describes the interaction between the resonator field and the two level system mediated by the coupling strength g. The two last terms represents the loss terms of the qubit and the resonator with the rates γ and κ, respectively. Here γ describes the decay of the qubit into modes other than the cavity mode and κ the escape rate of photons from the cavity. In circuit QED, the qubit-resonator coupling is designed to fulfill $g \gg \gamma, \kappa$ and the loss terms $\hat{H}_{\gamma}$ and $\hat{H}_{\kappa}$ in Hamiltonian (3.1) can be neglected in first approximation. Rotating the qubit into its eigenbasis and performing a rotating wave approximation (RWA) reduces the Hamitonian (3.1) to the Jaynes-Cummings

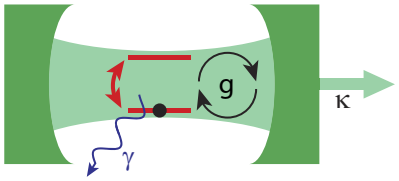

Figure 3.1: A two-level atom (red) interacting coherently with the field in a cavity at the rate g. Apart from the coherent process, relaxation processes of the qubit at a dacay rate γ and of the photon at a decay rate κ are depicted.

Hamiltonian [4, 80]

$$\hat{H}_{\mathrm{JC}} = \hbar\omega_{\mathrm{R}}\left(\hat{a}^{\dagger}\hat{a} + \frac{1}{2}\right) + \hbar\frac{\omega_{\mathrm{Q}}}{2}\hat{\sigma}_z + \hbar g \sin\theta\left(\hat{a}^{\dagger}\hat{\sigma}_- + \hat{a}\hat{\sigma}_+\right) \tag{3.2}$$

that describes the coherent behavior of the qubit and the microwave resonator. Here σ_+ and σ_- are the qubit raising and lowering operators. As in eq. 3.1 the first term is the resonator Hamiltonian. The second term represents the atom as a spin-1/2 system with transition energy $\hbar\omega_{\mathrm{Q}}$, the qubit. The third term describes the interaction where the atom (qubit) absorbs or emits a photon at the rate $g\sin\theta$, $\theta = \arctan(\delta_{\mathrm{Q}}/\varepsilon)$, while at the same time a photon is created or annihilated, respectively. The interaction term is the result of a rotating wave approximation of the more general dipole term $\hbar g \sin\theta(\hat{a}^{\dagger} + \hat{a})\hat{\sigma}_z$ from Eq. (3.1). This approximation is valid if $\omega_{\mathrm{Q}} + \omega_{\mathrm{R}} \gg g$, Δ, with the detuning $\Delta = |\omega_{\mathrm{Q}} - \omega_{\mathrm{R}}|$. The breakdown of this approximation was shown in Ref. [81] where the ultra-strong coupling regime has been accessed for the first time.

In addition to the coherent processes between a qubit and a cavity described by $\hat{H}_{\mathrm{JC}}$ (3.2) also incoherent phenomena are observable. In circuit QED coupled system fulfilling $g < \gamma$, κ can be very well modeled. Then, the last two terms of Eq. (3.1) can no longer be neglected and decoherence effects of the qubit at a rate γ and photon decay at a rate κ define the limits for coherent interaction processes and thus the limits of the strong coupling regime. To this effect, circuit QED is well suitable for studying quantum measurements and open systems. Although, this physics opens a wide field interesting experiments, it will not be discussed in detail. Within this work the strong coupling limit $g \gg \gamma, \kappa$ is fulfilled. Hence, loss processes are small and usually can be neglected.

The eigenstates of the Jaynes-Cummings Hamiltonian H_{JC} are neither qubit states ($|g\rangle$ or $|e\rangle$) nor photon number states $|n\rangle$ of the cavity, see Fig. 3.2. Good approximations of the resulting eigenstates can be provided in two regimes, the resonant and the dispersive regime.

3.1.1 The resonant regime

When the detuning Δ between the qubit transition frequency ω_{Q} and the resonator frequency ω_{R} is smaller than the coupling rate g one speaks of the resonant regime. In the absence of decoherence, an excitation placed in the system oscillates between a qubit excitation and a photon in the cavity. For such vacuum *Rabi oscillations*, the frequency is given by the coupling rate g. In the strong coupling limit, many oscillations can be completed before quantum coherence is lost.

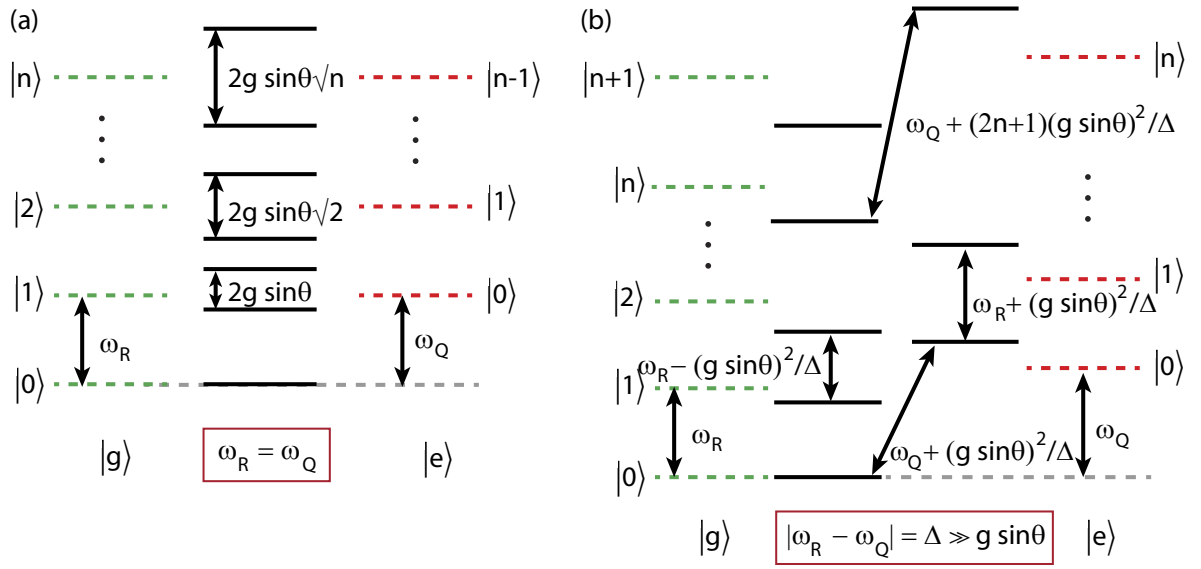

Figure 3.2: Schematic energy level diagram of the Jaynes-Cummings Hamiltonian. The dashed lines represent the eigenstates of the uncoupled systems. The states on the left side (green) are the states where the qubit is in the ground state, on the right side is the qubit is excited. $|n\rangle$ corresponds to the photon number states inside the cavity. (a) Resonant regime ($\Delta < g\sin\theta$); the coupled states split by $2g\sin\theta\sqrt{n}$. (b) Dispersive limit ($\Delta \gg g\sin\theta$); the resonator's frequency is shifted by $\pm g^2\sin^2\theta/\Delta$ depending on the qubit state while the qubit transition frequency is shifted by $\pm(2n+1)g^2\sin^2\theta/\Delta$. n is the photon number populating the cavity.

At $\Delta = 0$, the coupling rate g of the two systems leads to symmetric and antisymmetric superposition states having a splitting of $2g\sin\theta\sqrt{n}$, see Fig. 3.2(a). The resulting eigenstates, so called *dressed states*, are

$$|-,n\rangle = \cos\theta|g,n\rangle - \sin\theta|e,n-1\rangle$$

$$|+,n\rangle = \sin\theta|g,n\rangle + \cos\theta|e,n-1\rangle.$$

Although in the strong coupling limit the interaction can be observed, the relaxation cannot be neglected. Decay opens ways for new experiments such as atomic cooling using the Purcell effect [82]. Since excitations are equally shared between the qubit and the cavity the decay rate is $\Gamma = (\gamma + \kappa)/2$. By designing $\kappa \gg \gamma$ the cavity allows faster energy extraction. In this manner the qubit can be cooled to its ground state.

3.1.2 The dispersive limit

The dispersive limit ($|\omega_Q - \omega_R| \gg g\sin\theta$) opens possibilities for qubit detection which are also used within this thesis. Here, no atomic transitions occur but virtual photons mediate dispersive interactions. These lead to a level shift proportional to $(g\sin\theta)^2/\Delta$. The total Hamiltonian can be approximated as [83]

$$\hat{H} \approx \hbar(\omega_R + 2\chi\hat{\sigma}_z)(\hat{a}^\dagger\hat{a} + 1/2) + \hbar\omega_Q\hat{\sigma}_z/2. \tag{3.3}$$

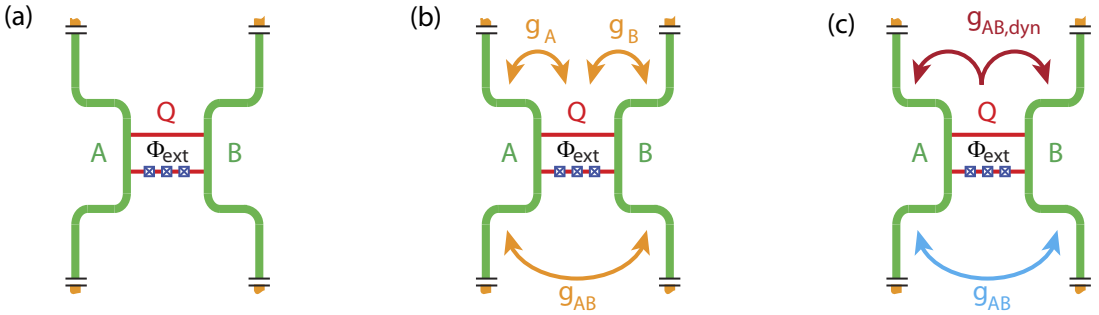

Figure 3.3: (a) Schematic of the quantum switch. (b) First order coupling channels (orange arrows). (c) From the analysis of the effective coupling Hamiltonian, one finds an effective coupling between the two resonators. It consists of a dynamic coupling mediated by the qubit (red arrow) and a geometric coupling defined mainly by the layout of the resonators (blue arrows).

Depending on the qubit state the resonator frequency is shifted by

$$\chi = \frac{(g \sin\theta)^2}{\Delta},$$

with the numbers of photons n inside the cavity, see Fig. 3.2(b). The relation between the resonator mode that is probed and the qubit state is presented in Ref. [84] and is used for qubit detection in a two-tone setup, see subsection 4.4.4.

Rearranging the terms of Eq. (3.3) yields

$$\hat{H} \approx \hbar\omega(\hat{a}^\dagger\hat{a} + 1/2) + \hbar[\omega_Q + 2\chi(\hat{a}^\dagger\hat{a} + 1/2)]\hat{\sigma}_z/2.$$

The qubit transition frequency is shifted by the photon number dependent AC-Zeeman shift $2n(g\sin\theta)^2/\Delta$ and the constant Lamb-shift $(g\sin\theta)^2/\Delta$. The former can be used to perform a quantum non-demolition measurement of the photon number inside the cavity and thus to calibrate the power in the system.

3.2 The quantum switch

After introducing into the basic concept of circuit QED, the system is extended to two-resonator circuit QED. This thesis concentrates on one specific device consisting of two on-chip microwave resonators and one flux qubit. The first part of this chapter analyzes the theory of the quantum switch by deriving and interpreting its Hamiltonian. Some simulations for different parameters are shown at the end of this section. They point out the criticality of the fabrication parameters of such a device.

3.2.1 Derivation of the quantum switch Hamiltonian

In this section a systematic formalism of two-resonator circuit QED is introduced. The qubit can function as a quantum switch between the two originally coupled resonators. The author refers to Ref. [43] where this device was proposed.

A schematic of the device is depicted in Fig. 3.3(a). The Hamiltonian of this three-

component system consists of the single components and the interaction terms

$$\begin{aligned}\hat{\tilde{H}} = &\frac{\varepsilon}{2}\hat{\tilde{\sigma}}_\mathrm{z} + \frac{\delta_\mathrm{Q}}{2}\hat{\tilde{\sigma}}_\mathrm{x} + \hbar\omega_\mathrm{A}\left(\hat{a}^\dagger\hat{a} + \frac{1}{2}\right) + \hbar\omega_\mathrm{B}\left(\hat{b}^\dagger\hat{b} + \frac{1}{2}\right) \\ &+ \hbar g_\mathrm{A}\,\hat{\tilde{\sigma}}_\mathrm{z}\left(\hat{a}^\dagger + \hat{a}\right) + \hbar g_\mathrm{B}\,\hat{\tilde{\sigma}}_\mathrm{z}\left(\hat{b}^\dagger + \hat{b}\right) \\ &+ \hbar g_\mathrm{AB}\left(\hat{a}^\dagger + \hat{a}\right)\left(\hat{b}^\dagger + \hat{b}\right).\end{aligned} \tag{3.4}$$

The interaction channels are depicted in Fig. 3.3(b). Here, $\hat{a}$ ($\hat{b}$) and $\hat{a}^\dagger$ ($\hat{b}^\dagger$) are the annihilation and creation operators for photons in resonator A (B). ω_A and ω_B ar the resonance frequencies of resonators A and B and g_A and g_B the first order coupling between between the qubit and the resonators A and B, respectively. For a flux qubit, the coupling between the qubit and the resonators is of inductive nature, meaning $\hbar g_\mathrm{A} = I_\mathrm{p} I_{\mathrm{A}0} M_\mathrm{QA}$ ($\hbar g_\mathrm{B} = I_\mathrm{p} I_{\mathrm{B}0} M_\mathrm{QB}$) where M_QA (M_QB) is the mutual inductance between resonator A (B) and the qubit. The vacuum (zero point) fluctuations of the current of resonators A (B) is given by the expression $I_{\mathrm{A}0} = \sqrt{\hbar\omega_\mathrm{A}/2L_\mathrm{A}}$ ($I_{\mathrm{B}0} = \sqrt{\hbar\omega_\mathrm{B}/2L_\mathrm{B}}$) and L_A (L_B) is the self inductance of resonator A (B).

Neglecting global energy offsets, assuming equal resonance frequencies ($\omega_\mathrm{A} = \omega_\mathrm{B} = \omega_\mathrm{R}$) and couplings ($g_\mathrm{A} = g_\mathrm{B} = g$) and rotating the Hamiltonian of Eq. (3.4) into the qubit energy eigenbasis $\{|g\rangle, |e\rangle\}$, one gets

$$\begin{aligned}\hat{H}' = &\frac{\hbar\omega_\mathrm{Q}}{2}\hat{\sigma}_\mathrm{z} + \hbar\omega_\mathrm{R}\left(\hat{a}^\dagger\hat{a} + \hat{b}^\dagger\hat{b}\right) \\ &+ \hbar g\cos\theta\hat{\sigma}_\mathrm{z}\left[\left(\hat{a}^\dagger + \hat{a}\right) + \left(\hat{b}^\dagger + \hat{b}\right)\right] - \hbar g\sin\theta\hat{\sigma}_\mathrm{x}\left[\left(\hat{a}^\dagger + \hat{a}\right) + \left(\hat{b}^\dagger + \hat{b}\right)\right] \\ &+ \hbar g_\mathrm{AB}\left(\hat{a}^\dagger + \hat{a}\right)\left(\hat{b}^\dagger + \hat{b}\right).\end{aligned} \tag{3.5}$$

Here $\omega_\mathrm{Q} = \sqrt{\delta_\mathrm{q}^2 + \varepsilon^2}$ is the qubit transition frequency and $\theta = \arctan(\delta_\mathrm{Q}/\varepsilon)$ the Bloch- or mixing angle.

In the dispersive limit ($\Delta = \omega_\mathrm{Q} - \omega_\mathrm{R} \gg g_\mathrm{AB}, g$) a Schrieffer-Wolff transformation [85] leads to an effective interaction Hamiltonian. Reference [44] compares two ways of calculating this effective Hamiltonian, within and beyond the rotating-wave approximation (RWA). Although, performing a Schrieffer-Wolff transformation after a RWA, the calculation becomes more clear, the result will deviate from a numerical simulation. Therefore, the more general calculation, beyond the RWA is sketched here.

The unitary transformation used to diagonalize the Hamiltonian of Eq. (3.5) up to second order is

$$\hat{U} = \exp\left(-\lambda_\Delta\mathcal{D} - \lambda_\Sigma\mathcal{S} - \lambda_\Omega\mathcal{W})\right).$$

The parameters read

$$\lambda_\Delta = \frac{g\sin\theta}{\Delta}, \qquad \Delta = |\omega_\mathrm{Q} - \omega_\mathrm{R}|$$

$$\lambda_\Sigma = \frac{g\sin\theta}{\Sigma}, \qquad \Sigma = \omega_\mathrm{Q} + \omega_\mathrm{R}$$

$$\lambda_\Omega = \frac{g\cos\theta}{\omega_\mathrm{R}}$$

and

$$\mathcal{D} = -\hat{\sigma}_+\hat{a} + \hat{\sigma}_-\hat{a}^\dagger - \hat{\sigma}_+\hat{b} + \hat{\sigma}_-\hat{b}^\dagger$$
$$\mathcal{S} = \hat{\sigma}_-\hat{a} - \hat{\sigma}_+\hat{a}^\dagger + \hat{\sigma}_-\hat{b} - \hat{\sigma}_+\hat{b}^\dagger$$
$$\mathcal{W} = \hat{\sigma}_z\left(\hat{a} - \hat{a}^\dagger\right) + \hat{\sigma}_z\left(\hat{b} - \hat{b}^\dagger\right).$$

Please note that in the dispersive limit the relation $\lambda_\Sigma, \lambda_\Omega < \lambda_\Delta \ll 1$ holds. These inequalities allow to neglect terms of higher order than $\lambda^2_{\Delta,\Sigma,\Omega}$. Thus, the effective second order Hamiltonian becomes

$$\begin{aligned}\hat{H}_{\text{eff}} = \hat{U}^\dagger\hat{H}'\hat{U} =& \hbar\frac{\omega_{\text{Q}}}{2}\hat{\sigma}_z + \hbar\omega_{\text{R}}\left(\hat{a}^\dagger\hat{a} + \hat{b}^\dagger\hat{b}\right) \\ &+ \hbar\hat{\sigma}_z g_{\text{dyn}}\left(\hat{a}^\dagger\hat{a} + \hat{b}^\dagger\hat{b}\right) \\ &+ \hbar\left(g_{\text{AB}} + g_{\text{dyn}}\hat{\sigma}_z\right)\left(\hat{a}^\dagger\hat{b} + \hat{a}\hat{b}^\dagger\right)\end{aligned} \tag{3.6}$$

with

$$g_{\text{dyn}} = \frac{(g\sin\theta)^2}{\Delta} + \frac{(g\sin\theta)^2}{\Sigma}. \tag{3.7}$$

This is the quantum switch Hamiltonian. The first two terms describe the qubit and the resonators, the third term represents the AC-Zeeman shift of the resonator modes due to the qubit. The last term describes the interaction between resonators A and B with an effective coupling coefficient. This coefficient consists of a geometric contribution g_{AB} due to the layout of the resonators on the chip, and a dynamic contribution $(g^2\sin^2\theta/\Delta + g^2\sin^2\theta/\Sigma)\hat{\sigma}_{\text{z}}$, see Fig. 3.3(c). Notably, the latter not only depends on the external applied magnetic field (due to the flux dependence of θ, Δ and Σ) but also on the qubit state. Consequently, depending on the qubit eigenstate, the effective coupling coefficient is

$$g_{\text{sw}}^{|\text{g}\rangle} = g_{\text{AB}} - \left(\frac{(g\sin\theta)^2}{\Delta} + \frac{(g\sin\theta)^2}{\Sigma}\right)$$
$$g_{\text{sw}}^{|\text{e}\rangle} = g_{\text{AB}} + \left(\frac{(g\sin\theta)^2}{\Delta} + \frac{(g\sin\theta)^2}{\Sigma}\right)$$

for $|\text{g}\rangle$ and $|\text{e}\rangle$, respectively. Since one part of the coupling is dynamic, the flux can be tuned such that

$$\frac{(g\sin\theta)^2}{\Delta} + \frac{(g\sin\theta)^2}{\Sigma} = g_{\text{AB}}. \tag{3.8}$$

This condition is called *switch setting condition* and represents the fundamental characteristic of the quantum switch. Depending on the qubit state, the resulting coupling is finite or vanishes. Hence, the two resonators are coupled and a normal mode splitting can be observed or they are completely decoupled and a signal entering one resonator cannot be transferred to the second resonator. Since a qubit is mediating the coupling between the two resonators, it may also be used to bring the switch into a superposition between "on" and "off". Interesting ideas for later measurement protocols will be given in chapter 6.

When performing a RWA in the Hamiltonian given by Eq. (3.5) prior to the second-order transformation, the contribution $(g\sin\theta)^2/\Sigma$ to g_{dyn} cannot be found. For realistic parameters one expects $g^2\sin^2\theta/\Delta = 10 - 100\,\text{MHz}$ and $g^2\sin^2\theta/\Sigma = 0.1 - 10\,\text{MHz}$.

Although the results differ only in the percent range, the $(g\sin\theta)^2/\Sigma$ contribution shall not be neglected.

Finally, insight into the physics beneath Eq. (3.5) can also be gained by analyzing the eigenmodes of the coupled resonators system. To this end, the operators

$$\hat{c}_\pm = \frac{1}{\sqrt{2}}\left(\hat{a} \pm \hat{b}\right), \qquad \hat{c}_\pm^\dagger = \frac{1}{\sqrt{2}}\left(\hat{a}^\dagger \pm \hat{b}^\dagger\right) \tag{3.9}$$

are introduced. Then, the Hamiltonian (3.5) can be expressed as

$$\begin{aligned}\hat{H}_{\text{eff}} =& \hbar\frac{\omega_{\text{Q}}}{2}\hat{\sigma}_z + \hbar(\omega_{\text{R}} + g_{\text{AB}})\hat{c}_+^\dagger\hat{c}_+ + \hbar(\omega_{\text{R}} - g_{\text{AB}})\hat{c}_-^\dagger\hat{c}_- \\ &+ \sqrt{2}\hbar g\cos\theta\hat{\sigma}_z\left(\hat{c}_+^\dagger + \hat{c}_+\right) - \sqrt{2}\hbar g\sin\theta\hat{\sigma}_x\left(\hat{c}_+^\dagger + \hat{c}_+\right).\end{aligned} \tag{3.10}$$

By performing a rotating wave approximation, the resulting Hamiltonian is

$$\begin{aligned}\hat{H}_{\text{eff}}^{\text{RWA}} =& \hbar\frac{\omega_{\text{Q}}}{2}\hat{\sigma}_z + \hbar(\omega_{\text{R}} + g_{\text{AB}})\hat{c}_+^\dagger\hat{c}_+ + \hbar(\omega_{\text{R}} - g_{\text{AB}})\hat{c}_-^\dagger\hat{c}_- \\ &- \sqrt{2}\hbar g\sin\theta\left(\hat{\sigma}_-\hat{c}_+^\dagger + \hat{\sigma}_+\hat{c}_+\right)\end{aligned} \tag{3.11}$$

The first term of this Hamiltonian describes the qubit and the two following terms two uncoupled resonator modes with different eigenfrequencies. The last term is an interaction term between the qubit and the higher $\hat{c}_+^\dagger$ mode mediated by a coupling constant $g_+ = \sqrt{2}g$. As Fig. 2.10(a) shows, the $\hat{c}_-^\dagger$ mode does not induce an effective magnetic field between the two resonator lines and thus cannot couple with the qubit. By comparing $\hat{H}_{\text{eff}}$ in Eq. (3.11) with H_{JC} in Eq. (3.2), it becomes clear that the terms concerning the qubit and the $\hat{c}_+^\dagger$ mode form a Jaynes-Cummings Hamiltonian.

3.2.2 Numerical simulation

For a better understanding of the system, the full Hamiltonian [Eq. (3.4)]

$$\begin{aligned}\hat{\tilde{H}} =& \frac{\varepsilon}{2}\hat{\tilde{\sigma}}_{\text{z}} + \frac{\delta_{\text{Q}}}{2}\hat{\tilde{\sigma}}_{\text{x}} + \hbar\omega_{\text{A}}(\hat{a}^\dagger\hat{a} + \frac{1}{2}) + \hbar\omega_{\text{B}}(\hat{b}^\dagger\hat{b} + \frac{1}{2}) \\ &+ \hbar g_{\text{A}}\,\hat{\tilde{\sigma}}_{\text{z}}(\hat{a}^\dagger + \hat{a}) + \hbar g_{\text{B}}\,\hat{\tilde{\sigma}}_{\text{z}}(\hat{b}^\dagger + \hat{b}) \\ &+ \hbar g_{\text{AB}}(\hat{a}^\dagger + \hat{a})(\hat{b}^\dagger + \hat{b})\end{aligned}$$

is diagonalized numerically. It is important to note, that although the effective coupling Hamiltonian of Eq. (3.6) only holds in the dispersive regime where $\Delta \gg g_{\text{AB}}, g$, the full Hamiltonian describes the dispersive and the resonant regimes.

The qubit and resonator parameters used in the simulation shown in Fig. 3.4 are chosen to be similar to the experimentally determined values. They are summarized in Tab. 3.1. In Fig. 3.4 the differences between the first three excited energy levels and the groundstate level are plotted versus the external magnetic flux Φ_{ext}. This spectrum is expected in a spectroscopy measurement. In the close-up [Fig. 3.4(b)] the switch setting condition is clearly visible in the form of a crossing of the two lowest transitions. At this flux value, the qubit is far detuned. This guarantees the quantum switch operation regime being in the dispersive limit. Thus, the decoherence time of the detuned qubit does not limit the

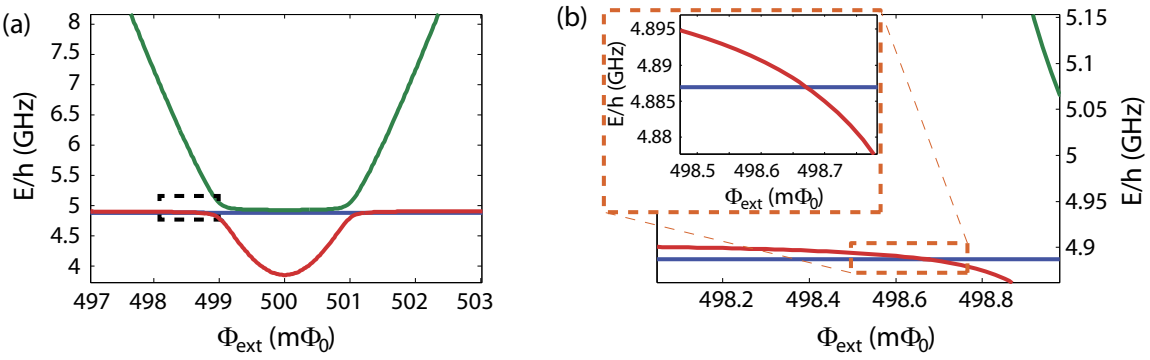

Figure 3.4: (a) Numerical simulation of energy eigenstates of the quantum switch as a function of Φ_{ext}. (b) Close-up of the area indicated by a dashed box in (a). The qubit (green) is far detuned from the resonator modes. The switch setting condition is in the dispersive limit. Close up in orange box: The crossing of the two resonator modes, indicating the switch setting condition is clearly visible.

decoherence of the quantum switch.

3.2.3 Critical parameters of the quantum switch

The simulation presented in the previous section is performed using the parameters listed in Tab. 3.1 which are also used in the experiment. Variations of the parameters may lead to a disappearance of the quantum switch behavior. Examples are also given in Tab. 3.1

Parameters	$\omega_{\text{R}}/(2\pi)$	$g_{\text{AB}}/(2\pi)$	L_{R}	δ_{Q}/h	I_{p}	$g/(2\pi)$
Sample (Fig. 3.4)	4.8957 GHz	8.5 MHz	4.8813 nH	3.9 GHz	490 nA	112 MHz
S 2 [Fig. 3.5(a)]	4.8957 GHz	8.5 MHz	4.8813 nH	4.3 GHz	540 nA	20 MHz
S 3 [Fig. 3.5(b-c)]	4.8957 GHz	8.5 MHz	4.8813 nH	5.9 GHz	540 nA	87 MHz

Table 3.1: Quantum switch parameters used for the simulation shown in Fig. 3.4 and Fig. 3.5. First parameter line gives the actual values realized in the experiment. Line two and three show variations of the qubit gap δ_{Q} and the coupling constant g.

where either the coupling g between the qubit and each resonator is reduced or the qubit gap is increased to 5.9 GHz.

Both scenarios are not unlikely. Experimentally, a sufficient coupling of $g \approx 100$ MHz is achieved by coupling the qubit galvanically to the resonator design. Thus, the qubit shares a line with each resonator as depicted in Fig. 2.3(b). A non-galvanically coupled qubit leads to coupling constants of only $10 - 30$ MHz [81]. Figure 3.5(a) shows that, although in this case the characteristic crossing of the energy levels is observable, the qubit is only detuned by a few MHz. As a consequence, some of the protocols suggested in Ref. [43] are more difficult to realize as their performance will suffer from the rather short coherence time of the qubit. The second scenario, a δ_{Q}-variation, to a larger gap energy, leads to a complete absence of the switch setting condiction. Here, the sum of the AC-Zeeman shift $2ng^2 \sin^2\theta/\Delta$ [33, 86] and the Lamb shift $g^2 \sin^2\theta/\Delta$ [87] is less

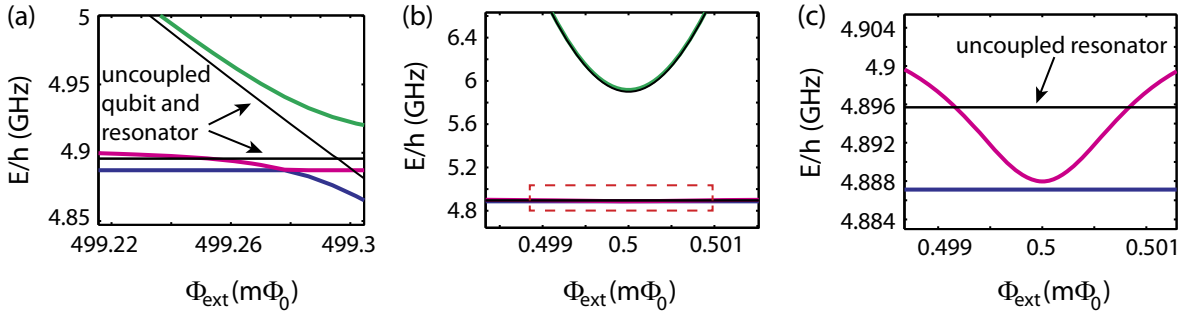

Figure 3.5: Spectra of devices with non-optimal parameters. For a better visibility the black lines in the figure show the undisturbed resonator and qubit energies. (a) Using parameters of S 2 (Tab. 3.1). The coupling g is too small, thus the switch setting condition is at a non-dispersive flux point. (b) and (c) Using parameters of S 3 (Tab. 3.1). The qubit gap δ_{Q} is increased to 5.9 GHz. AC-Zeeman and Lamb shift do not shift the higher mode such that a crossing is observable (c).

than $2g_{\mathrm{AB}}$ and a crossing is not observable. Similarly, one finds a qubit gap of less than 2.5 GHz to be unsuitable for the realization of a switch. Deviations of δ_{Q} are very likely since the gap energy is highly sensitive to fabrication parameters such as the Josephson junction size or the quality of the insulating oxidation layer.

The above examples illustrate that particular care has to be taken to fabricate a qubit with suitable parameters. A large portion of the next chapter is dedicated to this sensitive and critical fabrication process.

Chapter 4

Experimental Techniques

A well controlled fabrication process is of fundamental importance to realize operating devices. In this chapter, the experimental techniques to produce and measure a quantum switch sample are introduced. To this end, first the fabrication process of resonators and flux qubits are outlined. The exact fabrication parameters can be found in appendix B. Next, the fundamental cryogenic setups for qubit and resonator characterization are presented. These measurements are used to optimize the design parameters and the qubit fabrication process to obtain reproducible results. The 50 mK dilution unit that is used to characterize qubits is presented using the example of a four-Josephson-junction flux qubit. Here, a dc-SQUID is used to detect the magnetic field that is induced by the qubit. Finally, the setup and protocols for the quantum switch measurements are discussed.

4.1 Fabrication

A robust technique for the fabrication of thin layer structures with lateral dimensions in the µm-range, optical lithography with dry etching technology, is used for manufacturing the resonators. Another variant is the use of a lift-off process which is applied for the gold leads used for the dc-SQUID measurements. A lift-off process guarantees a smooth substrate surface after the first fabrication step which is useful for a good SQUID and qubit fabrication. Unfortunately, in the quantum switch experiment such a technique could not be implemented due to technical reasons. Tests of using a lift-off process to fabricate the two-resonator sample did not show the desired result. The resonators are made of 100 nm thick sputtered niobium which accumulates isotropic on the sample. As discussed in section 4.1.2 the lift-off process requires a well-defined undercut profile of the resist. As a result of the undercut and the isotropic distributed metal, the actual design is smeared a bit which has no significant impact on the gold leads but on the properties of the coupling capacitors of the resonators and thus directly on the quality factor of the resonators. A second risk factor lays in the thickness of the niobium. In the sputtering process the metal does not only sediment on top of the resist but also in the undercut profile. While the thin gold layer (20-30 nm) of the lead structures becomes very thin at the resist walls and leave a lot of pin holes that allow the lift-off process, the niobium layer is too thick and the absence of pin holes leaves no possibility for the lift-off step.

Since the fabrication process is complex and one might loose the overview, the outline for the fabrication is as follows: For the dc-SQUID detection of a qubit, first the dc-bias lines are fabricated using optical lithography and a lift-off process. Here, 36 samples are fabricated at once on a one-inch waver. In a second fabrication process, the qubit and

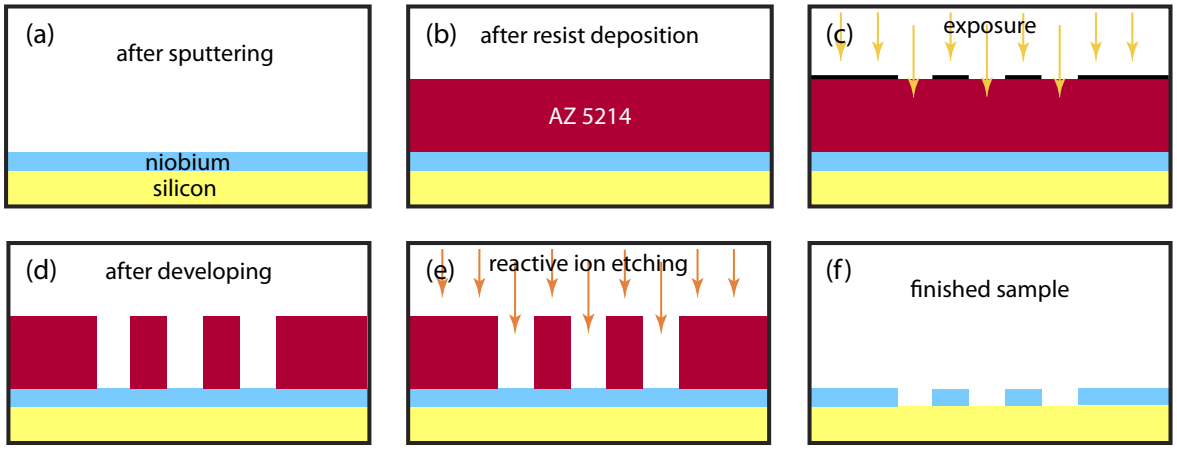

Figure 4.1: Schematic of the fabrication process: (a) Sputtering of 100 nm niobium on a silicon substrate; (b) Resist deposition: A 1.14 µm thick layer of AZ 5214 resist; (c) Exposure with UV-light though a chromium mask symbolized by the black line; (d) After developing the resist is an one-to-one image of the layout; (e) reactive ion etching removes metal; (f) Sample after final resist removal.

SQUID are placed onto the chips. In the end the waver is divided into 36 chips each with one sample. The fabrication of the quantum switch is similar. First the resonators are fabricated using a dry etching process and in a second process the qubit is placed onto the chip in between the resonators.

The three procedures, optical lithography with dry etching, optical lithography with lift-off and e-beam lithography are explained in the following.

4.1.1 Niobium resonators

The resonators are made of 100 nm sputtered niobium on a silicon substrate of $10 \times 6\,\mathrm{mm}^2$. The 250 µm thick silicon substrates are commercially available with a 50 nm thin, thermally grown oxide layer[1]. Optical lithography is used to define the geometric layout in the resist layer. The spatial resolution of the optical lithography is limited by the wavelength of the used UV-light, here 365 nm. This is suffizient to expose 2 µm small structures which are the smallest dimensions used in the resonator design. The niobium resonators are patterned using reactive ion etching (RIE).

A proper cleaning of a new substrate is an important step for a successful process. The commercially acquired substrates are covered with a layer of resist to protect the surface. This resist is removed in 70 °C warm acetone for at least 10 min. Afterwards, each substrate is cleaned by sonicating, twice in acetone and once in isopropanol. The substrate is dried with nitrogen and directly transferred into a high vacuum chamber for the deposition of 100 nm niobium, see Fig. 4.1(a). This is sputtered using a dc-magnetron. Here, a voltage of 500 V creates an Ar-plasma and accelerates the ions onto the niobium target. Niobium is emitted from the target and accumulates on the substrate. It is important to note that the sputtering process is an isotropic and not a directed process. The thickness of the resulting film was determined by X-ray diffraction and the quality by

[1] Crystec GmbH

measuring the residual resistance [88]. Using niobium instead of aluminum, which is used for the qubits, allows to characterize the resonators at 4.2 K as the critical temperature of niobium is 9.2 K.

Patterning the niobium film is achieved with optical lithography. An image reversal resist, AZ 5214[2] is spun onto the chip to a thickness of approximately 1.14 µm. A *soft bake* at 110° C for 70 s finishes the deposition step and the sample is ready for the exposure. The structures are copied from an optical mask by exposing the sample to UV-light trough the mask with a MJB3 Photomask Aligner from *Süss MicroTech*, see Fig. 4.1(c).

The exposed AZ 5214 is developed using an AZ 726 MIF Developer[3] which consists of 2.38 % tetramethylammoniumhydroxide (TMAH) in water. This developer is quite sensitive to exposed resist so that the developing time, typically between 55 s and 70 s, is not very critical. After that step, the structure of the resist is a one-to-one copy of the structure on the mask. Next, the uncovered niobium is removed in a RIE process. In general, two kinds of etching processes can be realized in a RIE system, chemical and physical etching. The first one implies a reactive SF_6 plasma and comparably low forward power in contrast to physical etching where the material is removed by an argon ion plasma and larger forward power. In this work, a mixture of both techniques is used, implying argon ions and moderate powers. This kind of etching ensures a good removal of the niobium whereas the resist layer is not affected dramatically. After the etching step, the niobium structure shows the layout of the resonators. After a last cleaning step, the sample can be either mounted into a sample box for measurements, see subsection 4.2.1, or used for quantum switch experiments which requires further fabrication steps to implement the qubit, see subsection 4.1.3.

4.1.2 Dc-bias lines

In the following, the layout and fabrication of the gold dc-bias lines will be shown. As mentioned before, 36 samples are fabricated at once on a one-inch waver, see Fig. 4.2. After the dc-bias lines are fabricated, 36 SQUIDs and qubits are implemented using a separate fabrication process before the waver is manually broken up into the 36 chips using a waver cutter.

Design of dc-bias lines

The on-chip dc lines made of gold are required to read out the SQUID. Two different designs of the bias lines are used in this thesis. The first one depicted in Fig. 4.2(a) is very robust against fabrication inaccuracies. In the blow-up one can see that although eight bias lines are designed for one chip, the layout provides enough space for different SQUID and qubit designs.

To provide the possibility of an on-chip RC-low pass filter, in a second layout [Fig. 4.2(b)] the ohmic resistance of the gold line on the chip is enhanced by increasing the line length and decreasing the line cross section. This layout is equivalent to the layouts presented in Refs. [81, 89]. The current lines are approximate 20 cm long and 5 µm wide, the voltage line are approximate 3 cm long. To double the thin meandered lines for voltage and current is reasonable since 30% of the lines, especially the long current lines, are broken.

[2]Microchemicals GmbH, AZ 5214
[3]Microchemicals GmbH, AZ 726 MIF

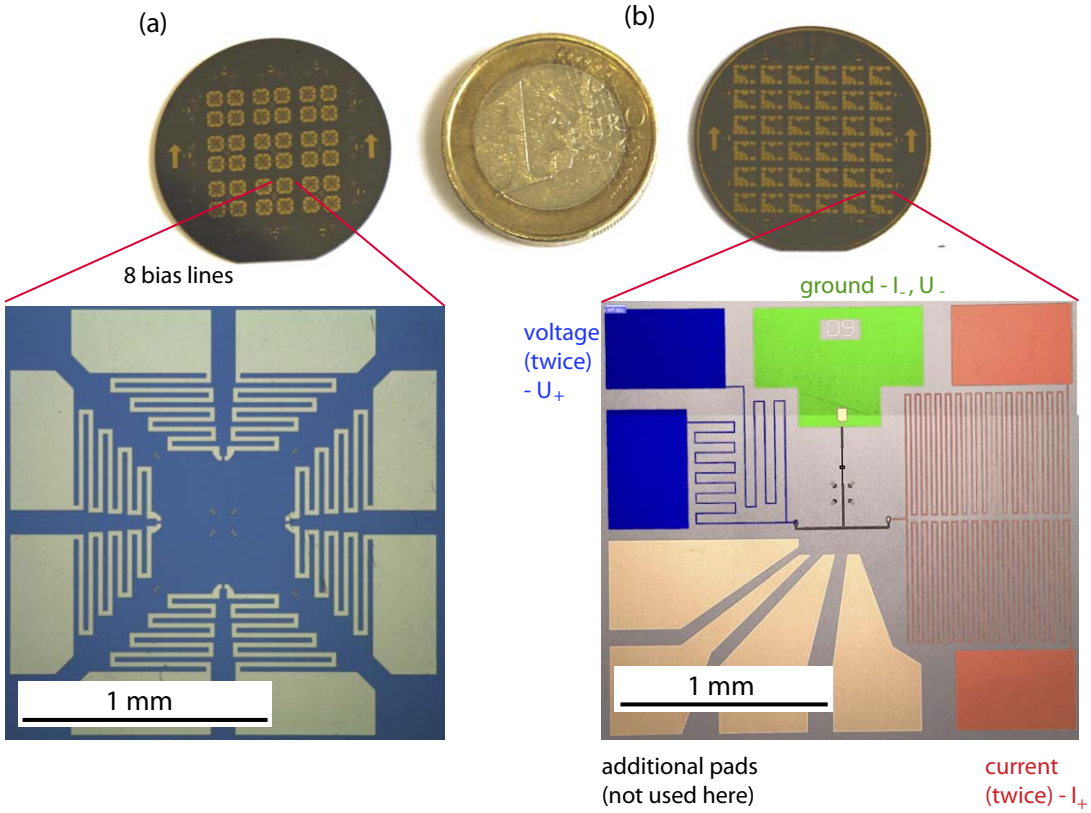

Figure 4.2: Two designs for the dc bias lines. (a) Photograph of a wafer with 9×4 chips in a first design. Blow-up: The on-chip resistance of the gold lines is low but the lines are robust against fabrication inaccuracies. The space in the middle guarantees the possibility of fabricating qubits and SQUIDS of various designs. (b) Photograph of a wafer with 36 chips. Magnified view of one chip (false color): The actual chip design with the meandered gold lines includes on-chip ohmic resistors. Since the thin meandering lines are very sensitive, two current (red) and two voltage (blue) lines were placed on the chip to connect I_+ and U_+ respectively. The ground (green) is used for the second current and the voltage connection, I_- and U_-.

For a four point measurement, only one meandered current (voltage) line is chosen to connect I_+ (U_+). I_- and U_- are connected to ground. The four additional pads on the chip are used for tunable flux qubits and are not relevant for this work.

Fabrication of gold bias lines

In contrast to the dry etching technique that is used in the two-resonator fabrication process, the on-chip bias lines for the dc-SQUID readout are made with a lift-off technique. This technique ensures a smooth surface of the silicon substrate after sample fabrication which is preferred for further qubit fabrication. The 525 µm thick silicon substrate is covered with a 50 nm thin thermally oxidized silicon layer, as the substrates for the two-resonator sample. Although, the substrate thickness varies in both cases, the thickness of the oxide layer is the same and the fabrication process of the qubit can easily be transferred.

The presented process is optimized to ensure a large undercut of the resist layer. Thus,

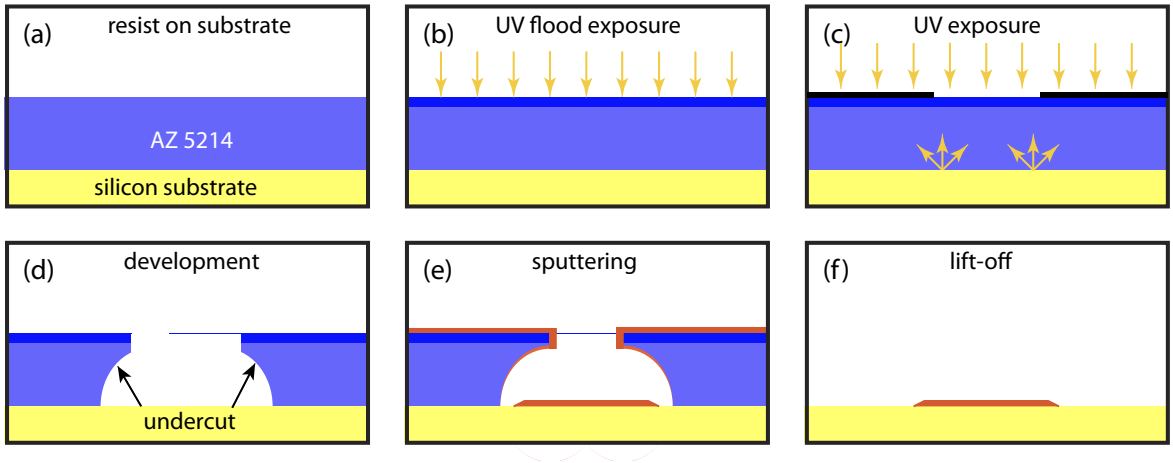

Figure 4.3: Schematic of the fabrication process used for the gold leads: (a) deposition of AZ 5214 followed by a soft bake; (b) UV flood exposure and followed by a reversal bake; (c) UV exposure using a chromium mask; (d) development for approximately 20 min; (e) in-situ sputtering of 5 nm chromium and 20 nm gold; (f) removal of remaining resist and metal in the lift-off step.

the sputtered gold structure shows a smooth edge profile in the end. Later in the SQUID fabrication, the aluminium leads of the SQUID must be connected galvanically with the gold lines, therefore sharp edges of the gold structure should be avoided. Gold is used as conductor due to two reasons: it shows a finite resistivity at low temperatures and it does not significantly oxidize at room temperature and atmospheric pressure.

Since the qubit is fabricated after the gold leads, the first cleaning step of the substrate is essential. In addition to the cleaning by sonicating, the plain substrate is ashed using an pure O_2 atmosphere in the RIE system. The following process steps are depicted in Fig. 4.3. For the optical lithography, the same resist[4] is used as for the etching process of the two resonators. By applying a flood exposure where the whole wafer is exposed briefly with UV-light, see Fig. 4.3(b), the resist at the surface is exposed with a higher dose than the resist close to the substrate. The following reversal bake leads to a hardening effect of the resist's surface. Later, these two steps will result in a well defined undercut.

The desired pattern is defined in the second UV exposure using a chromium mask and a MJB3 Photomask Aligner as in the fabrication process of the two resonators, see Fig. 4.3(c). The following development leaves the structure in the resist with a comparably large undercut. With the extra reversal bake, the developing time increases compared to the developing time of the etching process up to 20 min. The sample is now ready for the deposition of the metal as depicted in Fig. 4.3(d)

The principle of the gold-sputtering process does not differ from the principle of the niobium-sputtering process. Nevertheless, the table-top sputtering chamber used in this step allows for the sputtering of different materials in-situ. This is necessary since gold adheres very badly to the silicon substrate. Therefore, a 5 nm thin chromium adhesion layer is used before sputtering 25-30 nm gold, see Fig. 4.3(e). To remove the remaining resist and the additional metal the wafer is cleaned in warm acetone. This procedure is the so-called lift-off process, see Fig. 4.3(f). The result is a silicon substrate covered by

[4] AZ 5214E from *Microchemicals GmbH*

the golden bias lines which are used to connect a dc-SQUID.

4.1.3 Qubits and SQUIDs

The dimensions of the Josephson junctions of SQUID and qubit are in the submicrometer regime. Therefore, the patterning with an optical UV-light source is not possible. This section presents the fabrication of Josephson junctions using electron-beam lithography and shadow evaporation. The design of both qubits, the four-Josephson-junction qubit discussed in section 4.3 and the three-Josephson junction qubit implemented in the quantum switch, are shown and their differences are discussed.

Qubit designs

The qubit layout is adapted to the environment. The four-Josephson-junction qubit which is read out with a SQUID has a loop size of $20.5 \times 8.5\,\mu\text{m}^2$. The design is depicted in the lower part of Fig. 4.4(a). The exact design parameters were optimized within the diploma thesis of F. Bilger [90] and are listet in Tab. A.1 in appendix A. The areas of three of the Josephson junctions are $0.047\,\mu\text{m}^2$ while the fourth Josephson junction is reduced by a factor $\alpha = 0.65$. The final result depends on various parameters such as temperature, humidity and age of the used resist and the structure of the nearby environment. By writing proximity bars close to the Josephson junctions, see Fig. 4.4(c), the resist is exposed strongly at the junctions and proximity effects due to other structures or the other effects are almost negligible. With this functional element of the Josephson junctions, a transfer to other qubit layouts such as different qubit sizes is easy to perform. The Josephson junctions are created by overlaying two layers of aluminum with an aluminum oxide layer in between. Compared to former flux qubits designed and fabricated at the Walther-Meißner-Institut, Refs. [81, 89], these qubits are relatively large. The reason lies within the possible implementation of the qubits into the quantum switch. Although the design of the four-Josephson-junction qubit is not combined with the two-resonator sample within the scope of this thesis, the qubit is already designed to be easily implemented into the two resonators in the future.

The design of the Josephson junctions used in the SQUID and the three-Josephson-junction qubit differs completely. The layout parameters for this kind of Josephson junctions were already investigated by T. Niemczyk [81, 91]. As depicted in Fig. 4.4(d), proximity bars are also used to minimize inaccuracies. The areas of the Josephson junctions are $0.03\,\mu\text{m}^2$. The α-value is approximately 0.7. Apart from the Josephson junctions, also the design of the four-Josephson-junction qubit differs from the design of the three-Josephson-junction qubit, see Fig. 4.4(a). The latter is directly connected to the resonator. The gap in the niobium resonator line is closed by an aluminum line when fabricating the qubit. The interface between niobium and aluminum is critical since niobium builds a very hard oxide at ambient pressure and room temperature which cannot be avoided. Therefore, the overlap is chosen to be comparably large.

Electron-beam lithography

The Josephson junction is realized using shadow evaporation which requires a controlled undercut and a very hard top layer of the resist. The usage of a two layer resist combina-

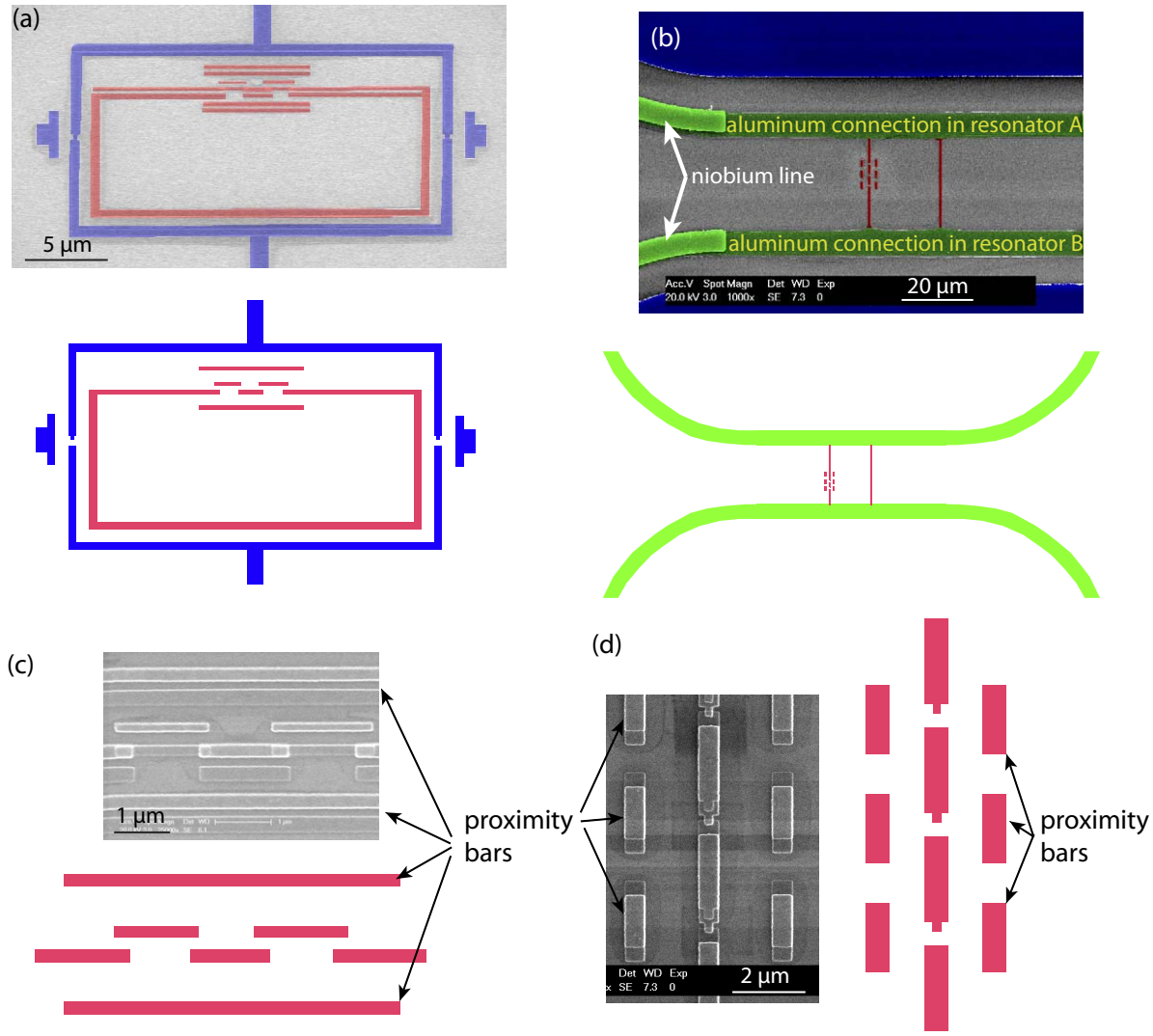

Figure 4.4: Scanning electron micrographs and e-beam layout of a four-Josephson-junction (red) and the read-out SQUID (blue) (a),(c) and a three-Josephson-junction (red) qubit embedded between the two resonator lines (green) (b), (d). (a) False color SEM picture of the qubit (red) and the SQUID (blue) and CAD design of the fabricated sample. (c) The magnified view of the Josephson junctions of the qubit clearly shows the proximity bars that are needed to guarantee a reproducible undercut. (b), (d) Analogous for the three-Josephson-junction qubit. The gap of the resonators are closed by a connection of aluminum (green). The qubit (red) is galvanically coupled to the two resonators.

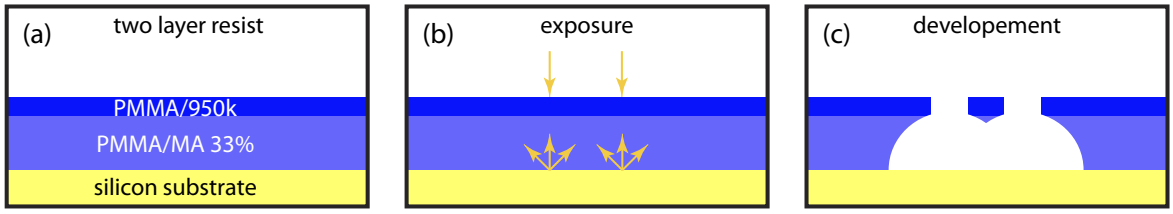

Figure 4.5: Electron-beam exposure of the resist for the qubit and SQUID pattern. (a) A two layer resist system consisting of PMMA/MA 33% and PMMA/950K is spun onto the wafer. (b) An electron beam is used to write the submicrometer structure into the resist. (c) After the development, the lower resist layer forms a well defined undercut.

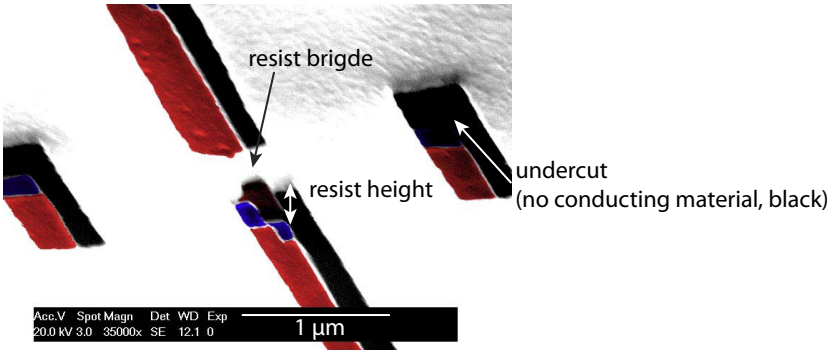

Figure 4.6: Slanted view from above on a free standing resist bridge. The already evaporated double layer structure can be seen (blue and red)

tion is a well established method at the WMI [81, 92, 93] and is depicted in Fig. 4.5(a). The bottom layer consists of PMMA/MA 33%[5] with a thickness of 680 nm. The resist of the top layer, PMMA/950k[6] is only 70 nm thin and less sensitive to high power electrons. The structure is written with an 30 kV electron beam onto the resist. The less sensitive top layer is only exposed at the exact position of the beam and thus defines the structure. The sensitivity to electrons of the lower layer results in the needed undercut, see Fig. 4.5(c). The proximity bars in the layout help to increase the undercut while the top layer of the resist is negligibly affected.

A critical part of a working qubit is the exact definition of the α-junction, the junction reduced by a factor of α compared to the other two (three) junctions. Since the dimensions of the fabricated structures are not exactly the designed dimensions of the layout, the manufacturer must know the exact e-beam behavior and readjust the designed sizes of the junctions. A deviation of the ideal size of the different Josephson junctions within one qubit of more than 10% leads, in general, to a non-working qubit as the gap energy δ_Q depends exponentially on α. The two Josephson junctions of the SQUID used in the readout of the four-Josephson-junction qubit are less sensitive than the Josephson junctions of the qubit.

After writing the layout into the resist and developing it, the layout is structured in the

[5] Allresist GmbH, PMMA/MA
[6] Allresist GmbH, PMMA/950k

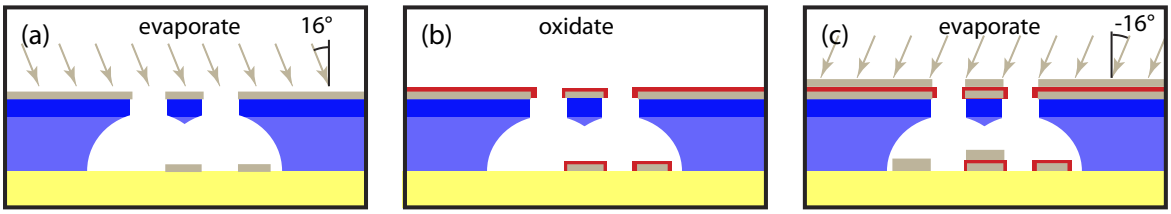

Figure 4.7: Schematic of shadow evaporation and oxidation (a) Aluminum evaporation under an angle of $\alpha = 16°$. (b) Oxidation for approximately 21-26 min. (c) Second evaporation using $\alpha = -16°$.

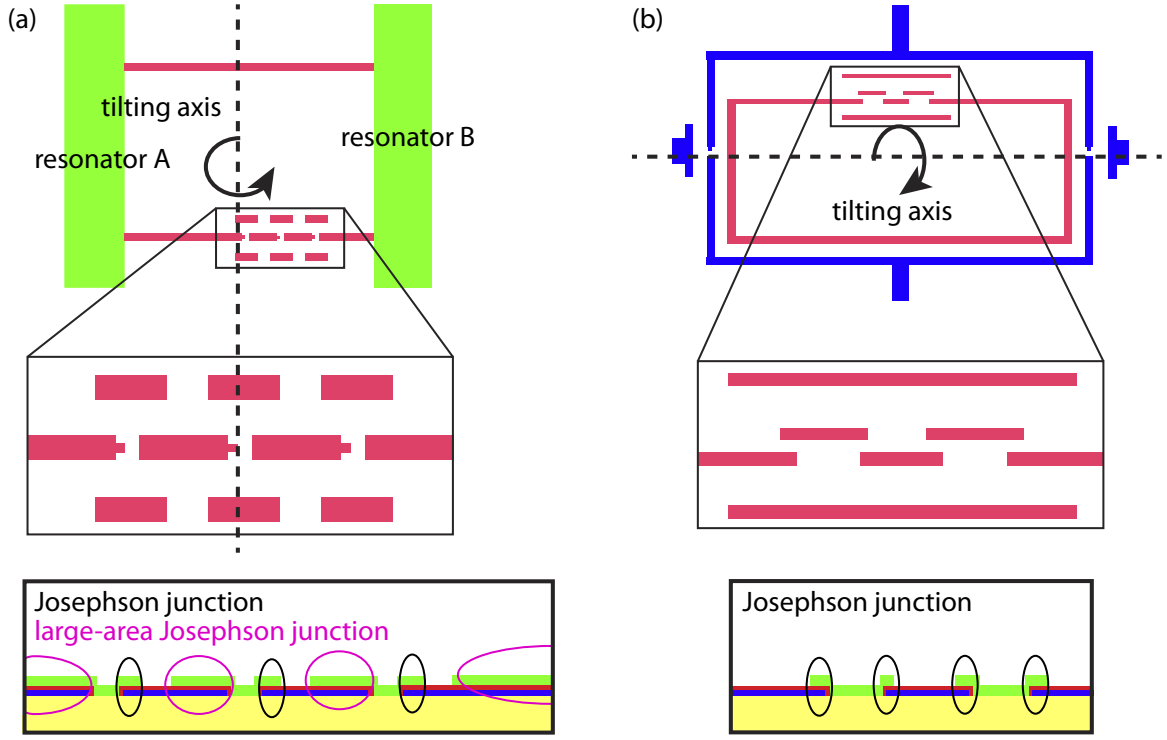

Figure 4.8: Schematic of the origin of extended Josephson junctions. (a) Since the current in all Josephson junctions goes from top (green) to bottom (blue) layer, it has to be transferred from top to bottom layer. This large Josephson junction is not taken into account as a qubit Josephson junction in theory. Nevertheless, it influences decoherence and dephasing times. (b) In the four-Josephson-junction design these extended Josephson junctions are avoided by using all layer transitions as well defined Josephson junctions.

top resist layer with a well defined undercut, see Fig. 4.5(c). This leads to free-standing bridges, as the SEM image of Fig. 4.6 shows.

Shadow evaporation and oxidation

For the shadow evaporation process, the wafer is mounted onto a sample holder and installed into the ultra high vacuum chamber used for this process. The system for the aluminium evaporation was installed by T. Brenninger [94]. In contrast to sputtering,

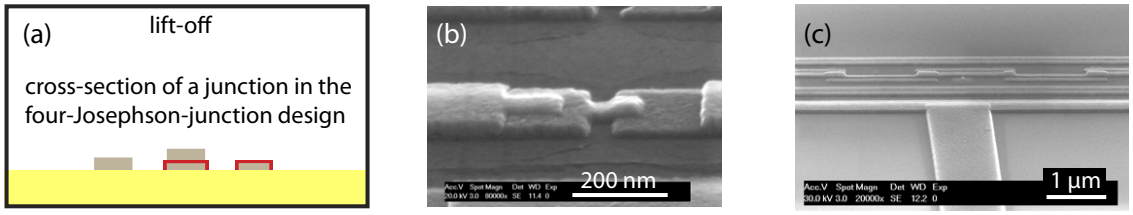

Figure 4.9: (a) shows the schematic of a Josephson junction after the lift-off process in the junction design of the four-Josephson junction qubit. (b) and (c) show scanning electron micrographs of typical Josephson junctions from a three-Josephson-junction qubit and a four-Josephson-junction qubit. The two layers of aluminum of the shadow evaporation can be easily seen.

electron-evaporation is a directed process. For the fabrication of the Josephson junctions, the sample holder can be tilted up to $\pm 90°$. In this case, the first aluminum layer is deposited under an angle of 16° and with a thickness of 40 nm, see Fig. 4.7(a). The next step is one of the most crucial steps in the fabrication process of Josephson junctions, the oxidation. The 1-2 nm thin oxide layer is fabricated by thermal oxidation in a dioxygen atmosphere at $p_{O_2} = 2 \times 10^{-4}$ mbar for 21-26 min. Since the critical current depends exponentially on the thickness of the oxide layer, small deviations of oxidation times and pressures easily leads to changes of the critical currents by a factor of two. Critical currents densities of 15 $\mu A/\mu m^2$ for the three-Josephson-junction qubit and 20 $\mu A/\mu m^2$ in the case of the four-Josephson-junction qubit are preferable but not compulsory. By evacuating the chamber again the oxidation process is stopped immediately. For the second evaporation, the sample holder is tilted by $-16°$ and the second aluminum layer is evaporated. To ensure a smooth connection over the edges from the first evaporation, the thickness of the second layer is 70 nm. So the total thickness of the qubit is around 110 nm and thus 10 nm thicker than the resonator thickness. That ensures a smooth coating at the resonator-qubit interface and the edges.

The shadow evaporation in combination with the design of the three-Josephson-junction qubit shows how the so-called large-area Josephson junctions are created. As the current in the Josephson junctions always flows from one to the other aluminum layer and the number of the layer transitions has to be even, a fourth large-area junction has to be included. Fig. 4.8 sketches how in the case of the three-Josephson-junction qubit the current has to be transferred back to the top layer. This large-area "Josephson junction" is around 50 times larger than the qubit Josephson junctions. The increased area of this junction leads to an enormous critical current and thus to a negligible phase drop. Therefore, this junction can be neglected in the theory of the qubit. Nevertheless, defects and impurities in the oxide layer influence the dephasing and thus the decoherence time of the qubit. The usage of four Josephson junctions allows to use all layer transitions as well-defined Josephson junctions. So the large-area Josephson junctions can be avoided. Although time-domain measurements were not realized within the scope of this thesis, the four-Josephson-junction qubit is already designed in view of optimizing decoherence times.

The fabrication of the qubit ends with removing the resist mask. This is again realized by a lift-off process in 70°C warm acetone. A sketch and a scanning electron micrograph of a Josephson junction is depicted in Fig. 4.9.

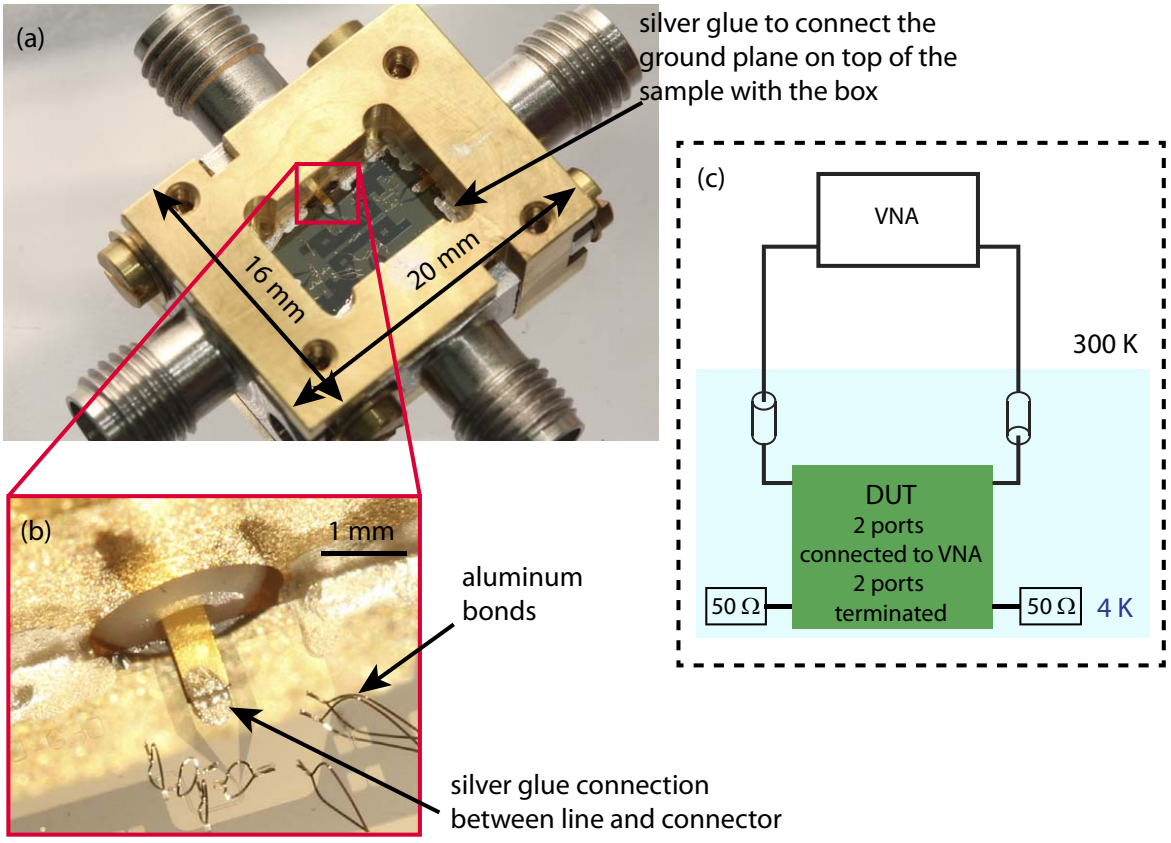

Figure 4.10: Setup to characterize the coupled resonators at 4 K. (a) Chip mounted in measurement box. The contacts between the niobium center strip and the box connectors is realized with silver glue (b). (c) Measurement scheme: a VNA HP 8722D is used to measure the transmission through two of the four ports. The remaining ports are terminated with 50 Ω RF-resistors.

4.2 Measurement setups for characterization

This section gives an overview on the measurement setups used for characterization: a ^{4}He bath cryostat used for measuring the two-resonators at 4.2 K in subsection 4.2.1 and a ^{3}He/^{4}He dilution unit used for the dc-SQUID measurements at 50 mK in subsection 4.2.2. Performing a transmission measurement on the coupled resonators is straight forward and does not need further explanation, in contrast to the dc-SQUID detection scheme. Therefore, the principle of the second setup is demonstrated in section 4.3 using a four-Josephson-junction qubit.

4.2.1 ^{4}He bath cryostat for transmission measurements

Compared with dilution cryostats and ^{3}He refrigerators, the ^{4}He bath unit is based only on ^{4}He which limits the cooling temperature to 1.5 K. The sample is cooled using liquid helium which is transferred from a transport vessel via an double-wall tube into the cryostat. The temperature can be decreased from 4.2 K to 1.5 K by pumping at the gas volume above the liquid ^{4}He. Although the cooling technique of this measurement is comparably plain, some issues have to be considered.

To characterize the sample at 4.2 K, the separated ground planes on the chip have to be connected via bonding wires. This step is very crucial to define a good common ground and thus to avoid groundplane modes. By mounting the chip into a gold plated copper box, see Fig. 4.10(a), and connecting the upper ground plane with silver glue at the sides of the chip with the box, the ground plane on top of the sample is well contacted with the box and thus also with the ground on the bottom of the chip. Silver glue is also used to contact the niobium center strip on the chip and the connectors in the box as shown in Fig. 4.10(b).

The sample box, see Fig. 4.10(a) is designed to avoid any spurious resonances below 8 GHz. Therefore, the inner dimensions are as small as possible and printed circuit boards (PCBs) are avoided. The dimensions of the two-resonator chips are $6 \times 10\,\mathrm{mm}^2$ that defines also the inner dimensions of the measurement box. As the room diagonal inside the box is approximate 11.5 mm and the effective permittivity of liquid is 1.05, the frequency of a λ mode inside the box is approximately 12.5 GHz. To place two 10-15 mm long resonators on the $6 \times 10\,\mathrm{mm}^2$ chip the resonator lines are meandered. The gold surface of the box suppresses the oxidation of the surface and ensures a good electric connection between the box and the ground planes on the chip. The CAD layout of the box is depicted in appendix C.

The setup for the first characterization of the two-resonator sample at 4.2 K is sketched in Fig. 4.10. A vector network analyzer (VNA)[7] measures the transmission through two of the four ports of the device. The device is mounted in the liquid helium dewar and the two measurement ports of the device are connected via stainless steel coaxial cables. The remaining ports are terminated with 50 Ω RF-resistors. This setup allows an easy and fast access to temperatures at which niobium is superconducting. For comparison, while in this setup cooling, measuring and warming up the sample can be performed within one day, it takes at least two days to cool the 50 mK cryostat.

4.2.2 50 mK setup for dc-SQUID measurements

To observe quantum phenomena such as characterizing the two lowest energy levels of a qubit, quasiparticle excitation in the superconductor has to be avoided and low temperatures are required ($2\Delta_\mathrm{s} \gg \hbar\omega_\mathrm{Q} \gg k_\mathrm{B}T$). The superconducting energy gap of aluminum $2\Delta_\mathrm{s} = 0.36\,\mathrm{meV}$ [47] corresponds to 87 GHz, a value that is confirmed in various SQUID measurements at the Walther-Meißner-Institut. With the qubit operating at approximately 5 GHz, $2\Delta_\mathrm{s} \gg \hbar\omega_\mathrm{Q}$ is easily fulfilled. Using a ^{3}He-^{4}He dilution cryostat that works at 50 mK, also the second requirement ($\hbar\omega_\mathrm{Q} \gg k_\mathrm{B}T$) is fulfilled.

The unit presented here is used to cool four chips at once. These are glued onto a silver sample holder and aluminum bonds are connecting the sample with the bronze bonding pads which are connected with the twisted-pair wiring of the cryostat. Figure 4.11(a) shows the bottom part of the dipstick where the sample holder with four samples is mounted. The 50 mK unit is a home-made dilution unit that was created for microwave spectroscopy on Josephson junction based devices. For this purpose a microwave antenna is included that allows signals up to 20 GHz. A simplified scheme of the measurement setup is shown in Fig. 4.11(b), a more detailed description of this dilution unit is given in Refs. [81, 90].

[7] Agilent, HP 8722D

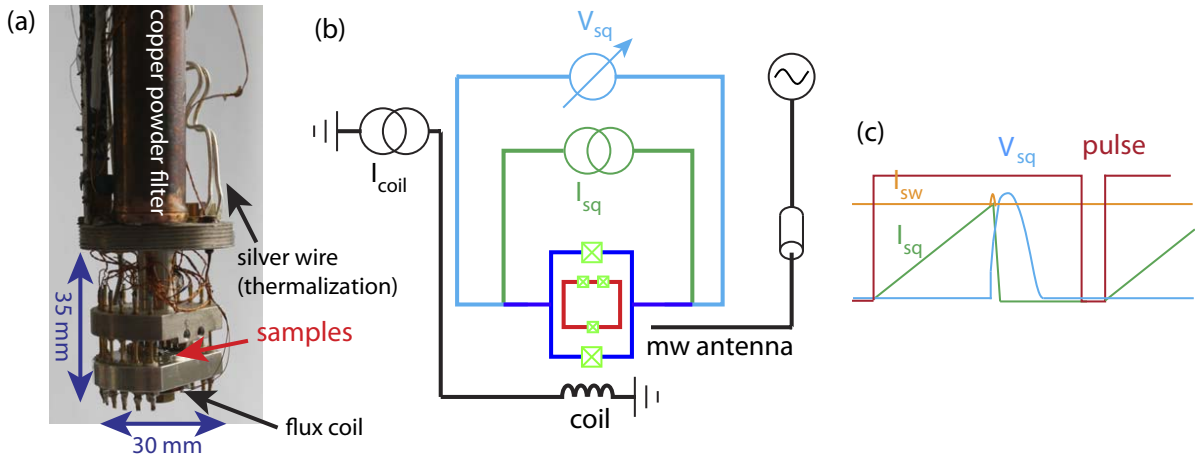

Figure 4.11: (a) Dipstick with sample holder of the 50 mK dilution cryostat. The coil for an external magnetic field is mounted below the sample holder. The copper powder filters are implemented in the dc lines and reduce rf-noise (cut-off frequency $\omega_c/(2\pi) = 2\,\mathrm{GHz}$, [81]). (b) Simplified schematic of the detection mode. The voltage of the SQUID is measured versus the applied bais current I_{sq}. A current I_{coil} in the coil generates an external magnetic field and a microwave antenna is used for exciting the qubit. (c) Signal sequence of a switching current measurement.

The detection of the switching current is sketched in Fig. 4.11(c). A linearly increasing current I_{sq} biases the dc-SQUID until it switches to the voltage state. The current value I_{sw} at which a voltage is detected by a threshold detector is recorded using a sample-and-hold circuit. The current I_{sq} decreases and the sequence is restarted. To get a good signal-to-noise ratio, the sequence has to be repeated for approximately 10-500 times. Apart from a time delay between the voltage drop and its detection the switching current I_{sw} is equal to $I_m = 2I_c|\cos(\pi\Phi_{ext,sq}/\Phi_0)|$, see section 2.2. The deviation lays in the percent regime.

Sweeping the applied field through the degeneracy point of the qubit, the current representing the qubit state is first reduced to zero, changes its direction, and increases again to the maximum value I_p. This results in a step-like structure on the $I_{sw}(\Phi_{ext})$ pattern, see Fig. 4.12(a). The positions of these steps within the $|\cos(\pi\Phi_{ext}/\Phi_0)|$ like pattern depend on the area ratio A_{sq}/A_Q of the SQUID area A_{sq} and the qubit area A_Q. By subtracting the SQUID pattern, the step becomes clearly visible and can be analyzed, see Fig. 4.12(b).

It is important to note that the step depicted here is the mean value of a large number of measurements and thus only shows the mean value of the current I_Q. Thus, the presence of the step is not a proof for a quantum mechanical behavior of the qubit. To distinguish between a "classical" qubit step where only values of $I_Q = \pm I_p$ are detected, see Fig. 4.12(c), and a "quantum mechanical" qubit step where also superpositions of the currents are possible, see Fig. 4.12(d), all measured current points have to be plottet in a histogram diagram. The absence of superposition states in Fig. 4.12(c) is caused by the fact that the tunnel barrier between the minima in the qubit's double well potential is too high. Thus, tunneling is not possible and the crossing of the energy levels $|R\rangle$ and $|L\rangle$ is not avoided ($\delta_Q = 0$).

An implemented microwave antenna close to the sample can be used to excite the

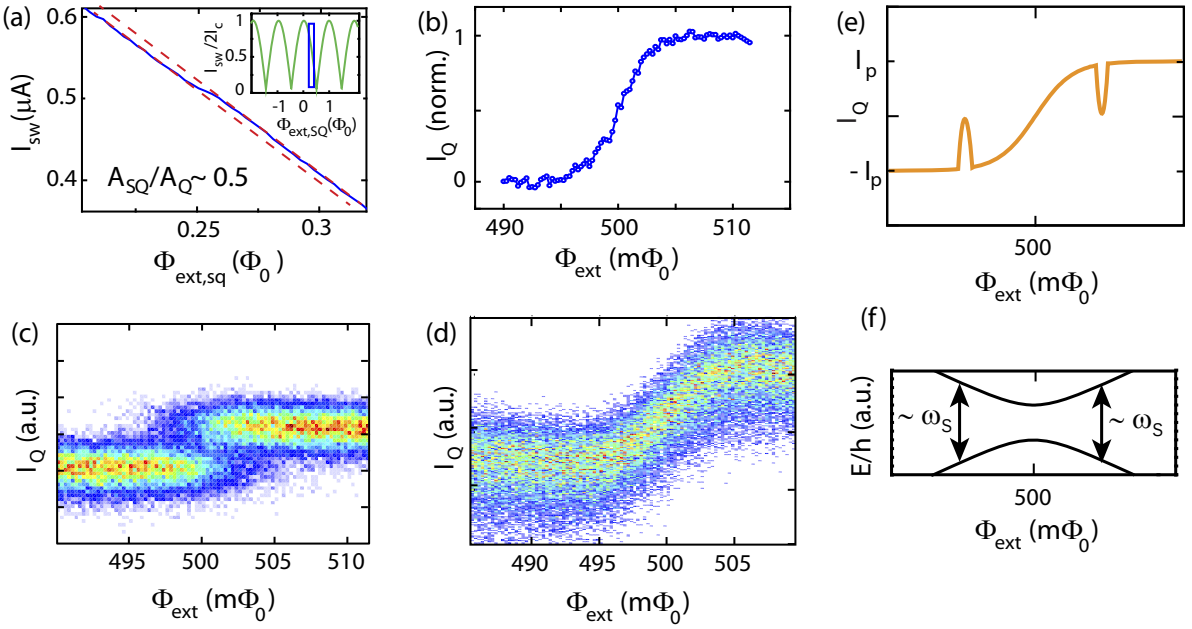

Figure 4.12: (a) Typical qubit in a $I_{\mathrm{sw}}(\Phi_{\mathrm{ext}})$ pattern of a SQUID. The deviation between the detected switching current I_{sw} and the theoretical I_{m} lays in the percent regime. The insert shows the location of the step in the $|\cos(\pi\Phi_{\mathrm{ext,sq}}/\Phi_0)|$-pattern. (b) By subtracting the SQUID modulation curve, the step gets clearly visible. Plotting the single switching events allows the differentiation between a classical step (c) or a quantum mechanical step (d) (Color code: red: high number of switching events, white: no switching events). (c) At a qubit with a vanishing gap energy δ_{Q}, the current values can be either $+I_{\mathrm{p}}$ or $-I_{\mathrm{p}}$. (d) The quantum mechanical qubit allows also superposition states. (e) and (f) Principle of a microwave spectroscopy detection. If $\omega_{\mathrm{s}} \approx \omega_{\mathrm{Q}}$ a dip and peak structure is observable at the corresponding flux position. The maximum peak or dip height is I_{Q}.

qubit. One induces a 50/50 occupation probability of the two qubitstates resulting in $I_{\mathrm{Q}} = 0$. The transition from the ground state to the excited state at a give flux value is represented by a change of I_{Q}. This causes a dip and peak structure symmetrically to $0.5\,\Phi_0$ as depicted in Fig. 4.12(e). The maximum peak or dip height is I_{Q}. The flux position of the response depends on the microwave frequency ω_{s} and the pair $(\Phi_{\mathrm{ext}}, \omega_{\mathrm{s}})$ are points on the qubit hyperbola. Repeating this measurement with different microwave frequencies ω_{s}, the transition frequency ω_{Q} and thus the gap energy δ_{Q} which is the minimum, and the persistent current I_{p} can be estimated.

The usage of this setup will be demonstrated in the next section using a four-Josephson-junction qubit.

4.3 Characterization of a four-Josephson-junction flux qubit

The setup described in the preceding section is used to characterize qubits and thus to optimize fabrication parameters bevor implementing a qubit into a circuit QED experiment. In the following this process will be demonstrated using a four-Josephson-junction

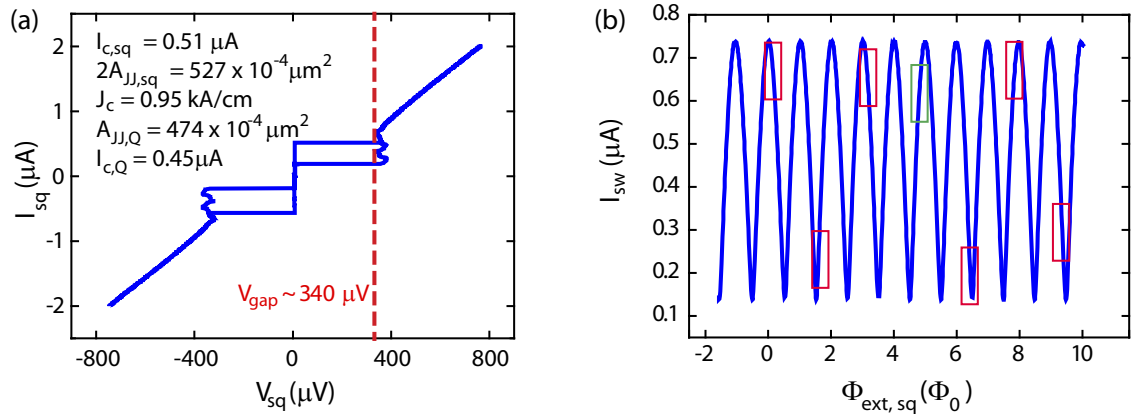

Figure 4.13: (a) $V_{\mathrm{sq}}(I_{\mathrm{sq}})$ measurement of a dc-SQUID used for the detection of a four-Josephson-junction qubit. The measurement is used to determine $J_{\mathrm{c}} = 0.95\,\mathrm{kA/cm^2}$, $V_{\mathrm{g}} = 340\,\mu\mathrm{V}$ and $R_{\mathrm{n}} = 333\,\Omega$ (b) I_{m} vs. the magnetic flux $\Phi_{\mathrm{ext,sq}}$. The colored boxes mark the positions of the qubit steps. The area ratio $A_{\mathrm{sq}}/A_{\mathrm{Q}}$ is approximately 1.52. The qubit step at $\Phi_{\mathrm{ext,sq}} = 5.805\,\Phi_0$ (green box) is chosen for further microwave spectroscopy.

qubit.

4.3.1 SQUID characterization

Before the qubit is characterized, knowledge about the SQUID is necessary. Parameters such as the critical current density J_{c} and the gap voltage V_{g} give information about the persistent current and the quality of the aluminum.

The current voltage measurement, Fig 4.13(a), yields $2I_{\mathrm{c}} = 0.51\,\mu\mathrm{A}$. The normal resistance R_{n} is extracted from the measurement to be $333\,\Omega$. As the measured sizes of the SQUID junctions is $A_{\mathrm{JJ,sq}} = 0.026\,\mu\mathrm{m}^2$ the critical current density is $J_{\mathrm{c}} = 0.95\,\mathrm{kA/cm^2}$. The same current density is assumed for the qubit. Using Eq. (2.12) the persistent current is calculated as $I_{\mathrm{p}} = 272\,\mathrm{nA}$. The red dashed line indicates a gap voltage of $340\,\mu\mathrm{V}$. This is a typical value for aluminum and also verified by Ref. [81].

In addition to the current voltage characteristics, the dependence of the SQUID critical current on an applied field and the qubit steps have to be measured and located. Thus, it is necessary to know the area ratio of the SQUID and the qubit. According to the layout, this is $A_{\mathrm{sq}}/A_{\mathrm{Q}} = 1.625$. The ratio of the applied magnetic field B_{Q} that is required to couple a single flux quantum Φ_0 into the qubit loop, and the applied magnetic field B_{sq} that is required to couple a single flux quantum into the SQUID loop holds $B_{\mathrm{sq}}/B_{\mathrm{Q}} = A_{\mathrm{sq}}/A_{\mathrm{Q}}$. The colored boxes in Fig. 4.13(b) show the step positions within the SQUID modulation curve. They are well separated by $1.52 \pm 0.06\Phi_0$. Thus, the designed area ratio of SQUID and qubit is approximately 6 % larger than the realized one.

The modulation depth indicates a small β_L parameter and thus a negligible loop inductance L. Microwave spectroscopy measurements shown in the following subsection are performed at the qubit step at $\Phi_{\mathrm{ext,sq}} = 5.805\,\Phi_0$. This step position is chosen because of the high signal-to-noise ratio of the detected critical current and because of the nearly linear SQUID modulation background.

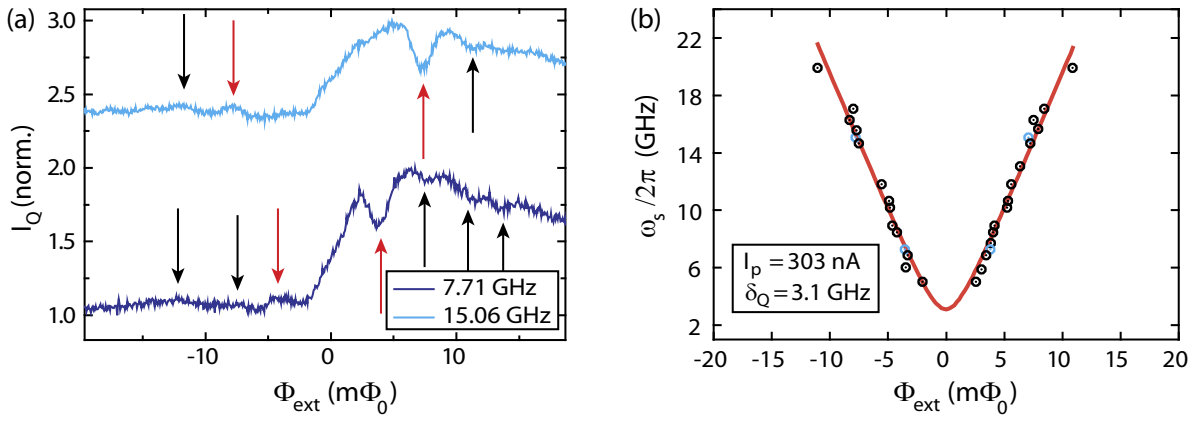

Figure 4.14: (a) Two measurements of the qubit step with $\omega_s/2\pi = 7.71\,\text{GHz}$ and $\omega_s/2\pi = 15.06\,\text{GHz}$. Apart from the one photon peaks and dips (red arrows) also two and sometimes three photon peaks and dips (black arrows) are visible. In general, these responses are weak and thus are not used for further investigations. (b) The (Φ_{ext}, ω_s) pairs of the dips and peaks (black dots) are plotted together with a fit according to Eq. (2.9) (red line). The two peak and dip pair depicted in (a) are symbolized by blue dots.

4.3.2 Qubit microwave spectroscopy

In this section, continuous-wave (cw) microwave spectroscopy is used to determine the qubit transition frequency $\omega_Q = E_Q/\hbar$ and the qubit gap energy δ_Q. The qubit step is measured in an interval of $\pm 20\,\text{m}\Phi_0$ around the degeneracy point while a cw spectroscopy tone with a fixed microwave frequency ω_s is applied. By subtracting the linear contribution of the SQUID the qubit step can be analyzed in more detail. Close to the maximum of the SQUID modulation, the linearization of the background breaks down and a decreasing slope can be observed in the SQUID pattern, see Fig. 4.14. At flux values fulfilling $\omega_s \approx n\omega_Q(\Phi_{ext})$, the qubit is excited. The change of the current $I_Q = I_p\langle\sigma_z\rangle$ of the qubit is recorded in a dip or peak. The visibility of the dip and the peak of each measurement depends on the detailed structure of the electromagnetic environment. Since the latter is only partially controlled in our experiment, only single photon transitions are reliably detectable. Multi photon transitions can be recorded in some measurements, see Fig. 4.14(a), but their signal is typically small. For this reason, they are not used for subsequent analysis.

Peak and dip positions of the one-photon transition extracted from the qubit step as shown in Fig. 4.14(a) are plotted for various values of ω_s in Fig. 4.14(b). Clearly, a hyperbolic shaped trend can be recognized. Numerical fitting of these points using Eq. (2.9) and Eq. (2.7) gives $\delta_Q/h = 3.2\,\text{GHz}$ and $I_p = 303\,\text{nA}$. The latter agrees well with the estimation presented in section 4.3.1. In conclusion, the extracted parameters provide a good foundation for further experiments based on four-Josephson-junction qubits.

4.4 Quantum switch setup

Apart from the setups used for characterizing the single components the main setup consists of a 30 mK dilution unit with larger sample space. An important part of this

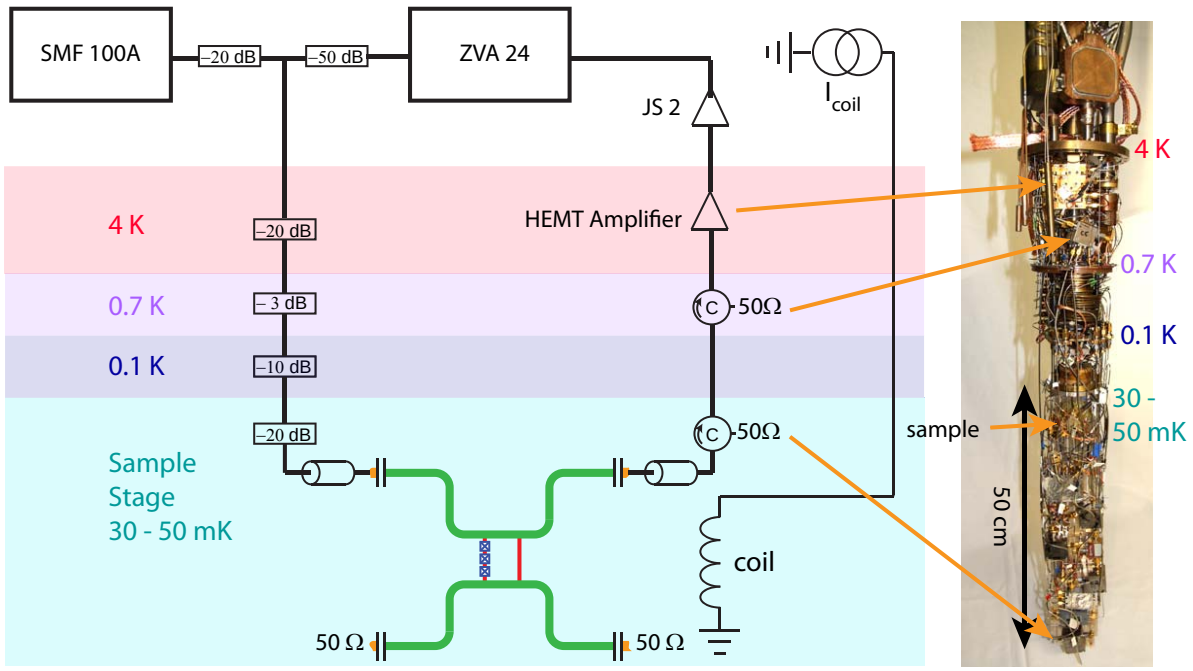

Figure 4.15: Schematic of the measurement setup of the 30 mK dilution refrigerator used for the quantum switch measurements. The input signals are attenuated by at least -53 dB distributed on 5 attenuators at the different temperature stages. The power of the outcoming signal is generally on the level of a single microwave photon and has to be amplified for detection. Due to noise minimization, this is done in two steps, using a HEMT amplifier at 4 K and a JS2 amplifier at room temperature. The signal is detected by a ZVA 24 VNA. The actual dimensions of the setup can be seen in the picture.

thesis is the preparation of this fridge for circuit QED measurements. In cooperation with three other PhD students, seven microwave input lines, four output chains equipped with high electron mobility transistors (HEMT amplifiers) and 64 twisted-pair dc wires are mounted. In this way, up to four circuit QED samples can be cooled down simultaneously, allowing for efficient usage of "fridge time".

In the following, an overview about the whole detection scheme is given and some crucial steps of the assembly process, where the author has undertaken a major part, is explained in detail. A schematic of the whole setup is shown in the appendix D.

4.4.1 Overview of the measurement setup

It is important to note that only two rf-cables were available to connect the four-port quantum switch, see Fig. 4.15. Thus, only two ports namely the two ports of one resonator are accessible in the measurement. Additional switches could not be implemented. The remaining ports are terminated with 50 Ω resistances. This configuration allows for transmission measurements through one resonator and spectroscopy of the qubit. A two port configuration is chosen as the remaining cables in the cryostat are used for different samples. Unfortunately, of the three quantum switch samples with varying design only the one with a galvanically coupled qubit and all three Josephson junctions on one qubit

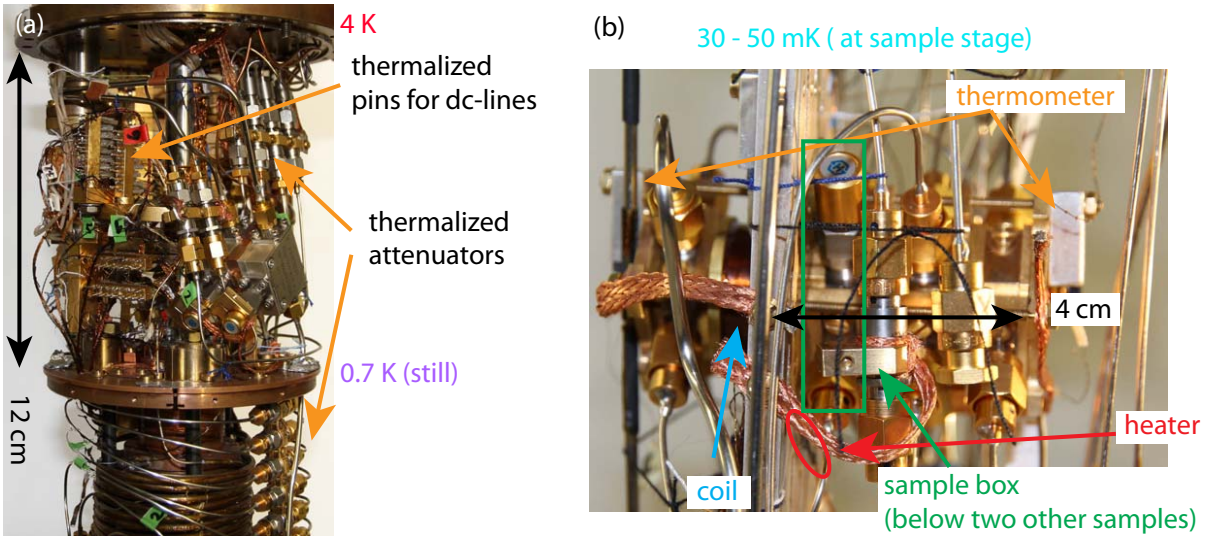

Figure 4.16: (a) Thermalized attenuators at 4 K (upper part) and still temperature (lower part). One can also see the connection pins for the 96 dc-lines used for heaters and thermometers. (b) Three samples mounted at the sample stage. The sample of interest is the closest one to the sample rod.

branch shows satisfying results. As the flux qubit parameters are very sensitive[8] against cooling cycles, the sample is not remounted before the spectroscopy measurements has been finished.

The high-frequency measurement signals are generated at power ranges between −40 dBm and 0 dBm (10^{-7} W - 10^{-3} W) at room temperature using a VNA[9] and a signal generator[10]. They need to be attenuated and after interacting with the sample, amplified and routed back to the data analysis circuit at room temperature, see Fig. 4.15. The following subsection gives details about the used input wires and amplification chain.

4.4.2 rf-wiring

The whole setup is optimized to minimize the amount of thermally populated photons and Johnson & Nyquist noise that reach the sample. This requires careful thermalization of all in- and output lines. To decrease any signal-losses and thermal conductivity, the used coaxial wires at temperatures below 4 K are made of superconducting niobium (inner conductor) and cupro-nickel (outer conductor) (UT47: SC-119/50-Nb-CN as input lines and UT85: SC-219/50-Nb-CN as output lines). The length of cables are adapted individually. To check the performance of the cables each cable and each connector is characterized using a time domain reflectometer (TDR) measurement. A mismatch of less than 5 Ω is acceptable.

To thermalize the input chain each used attenuator is thermally coupled to the corresponding temperature stage, see Fig. 4.16(a). In total, input signals generated at room temperature are attenuated by -103 dB. The cable loss is frequency dependent. At 5 GHZ the overall cable loss can be approximated by -10 dB. A power splitter (not shown in the

[8] E. g., from the first to the second cooling cycle the gap energy δ_Q shifted by 10%.
[9] R&S, ZVA 24
[10] R&S, SMF 100A

schematic of Fig. 4.15 but in the complete setup in Fig. D.1) with -3 dB loss have to be considered, too. Thus, an overall attenuation of −116 dB is a good approximation for the attenuation of the input chain at 5 GHz. The chosen attenuation configuration leads to 0.025 thermally populated photons at the sample input port, a number that can be neglected during the measurements.

The sample itself is mounted into the gold-plated copper box which is also used in the characterization measurements at 4 K shown in section 5.1.2. The box is mounted on a sample-stage made of silver. Silver is chosen due to its high thermal conductivity at millikelvin temperatures. In Fig. 4.16(b), the position of the sample box is right next to the coil which creates the magnetic field.

In general, the emitted signal from the resonators has a power between −130 dBm and −110 dBm (10^{-17} W and 10^{-15} W). A larger cross-section of the coaxial cables helps to avoid losses in the lines. Thus, UT 85 with an outer diameter of 2.2 mm are used for the output chain. The output chain includes two 4-8 GHz circulators from Pamtech. They are needed to reduce back-action of the amplifier noise on the sample and to thermalize the output lines, see Fig. 4.15. The signal is amplified in two steps, once at 4 K using a commercially available HEMT amplifier working in the 4-8 GHz regime and at room temperature using a Miteq JS2 amplifier.

4.4.3 dc-lines for thermometry

Apart from the sample measurement, the control and knowledge of the temperature is fundamental in low temperature experiments. Therefore, several thermometers at different stages adjusted to the used temperature range are installed as well as a heater close to the sample to control the sample temperature. 64 twisted-pair cables for the dc wiring are fed into the vacuum chamber from room temperature via the pumping port. The layout and CAD drawings of the used components, such as the connection box for example are shown in appendix D.2. A crucial issue here is the quality of the connector assembly, since the quality of the vacuum must not be affected.

Between room temperature and 1 K, the dc-lines consists of 0.15 mm thick manganin wires which ensures a good electrical conductivity paired with a relatively low thermal conductivity. Thermal conductivity has to be even more suppressed for lower temperatures. Therefore, between 1 K and lower temperature stages superconducting niobium-titanium wires, either in a bronze or cupro-nickel matrix, are used. The connection-pins at 1 K can be seen in Fig. 4.16(a).

At each temperature stage at least one thermometer is mounted. At the sample stage several thermometers are mounted to check for temperature gradients on the approximately 50 cm × 15 cm large stage. This is necessary since a heater, see Fig. 4.16(b), is located at the sample rod. Small temperature deviations of a few millikelvin on the sample rod require thermometers close to the samples.

This setup allows sufficient control of the temperature of the single stages of the cryostat and a precise knowledge of the sample temperature. The heater is used to stabilize the sample at a constant temperature. The temperature can be stabilized to values between 30 - 100 mK. The presented measurements are taken at 50 ± 0.1 mK. Although this is almost twice the base temperature of the cryostat, it is well sufficient to measure at this high temperature. In this way, the system is more stable against external vibrations and low frequency noise on the thermometry lines.

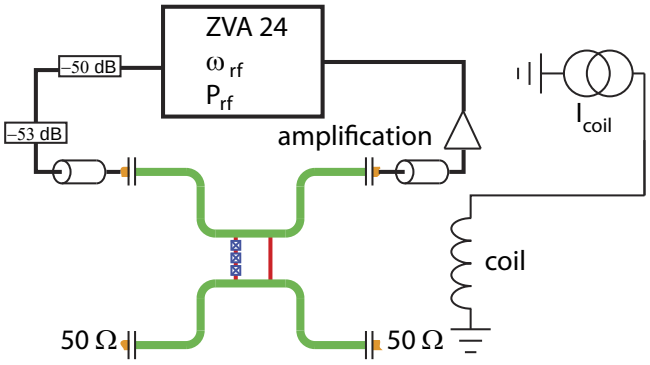

Figure 4.17: Schematic of transmission measurement setup. The frequency ω_{rf} at a power P_{rf} is swept and the transmission through the quantum switch is detected. This measurement is repeated for different flux values. The data is plotted in a flux-frequency plot where the z-axis shows the magnitude of the transmitted signal.

4.4.4 Spectroscopy protocols

The 30 mK-setup is used to perform transmission measurements through the two-resonator sample and two-tone spectroscopy to characterize the qubit. In the following both measurement schemes are discussed.

The transmission measurements described here are similar to the transmission measurements of the two-resonator sample at 4 K. As Fig. 4.17 shows a vector network analyzer, here the ZVA 24[11], is used for generating and detecting high frequency signals. The generated signal power at the output of the ZVA is between $P_{\mathrm{rf}} = -30\,\mathrm{dBm}$ and $P_{\mathrm{rf}} = -10\,\mathrm{dBm}$. Including all attenuators, loss of the coaxial lines and the splitter, the power at the input of the resonator is between $-146\,\mathrm{dBm}$ and $-126\,\mathrm{dBm}$ at 5 GHz. To take a concrete example, a power of $-140\,\mathrm{dBm}$ inside the cavity is equivalent to that of a single photon at 5 GHz. This power inside the cavity is generated using $P_{\mathrm{rf}} = -6\,\mathrm{dBm}$ at room temperature. For a fixed flux value, the frequency ω_{rf} of the signal is swept and the transmitted response through the quantum switch is detected. An external coil is used to generate a magnetic field that tunes the qubit transition frequency. The measurements show how the resonator modes change with respect to the external flux.

The second measurement scheme is two-tone spectroscopy. In the following, the protocol for this measurement technique is described. As Eq. (3.11) suggests only the interacting mode of the quantum switch at ω_+ and the qubit will be considered. The mode at ω_- which does not interact with the qubit does not affect the measurement scheme and can be neglected. Since Eq. (3.11) implies a Jaynes-Cummings like behavior of the higher mode, the treatment described in subsection 3.1.2 can be applied. In the dispersive regime ($|\Delta_+| = |\omega_+ - \omega_{\mathrm{Q}}| \gg g_+$) the total Hamiltonian can be approximated as in Eq. (3.3) by

$$\hat{H} \approx \hbar(\omega_+ + 2\chi\hat{\sigma}_z)(\hat{a}^\dagger\hat{a} + 1/2) + \hbar\omega_{\mathrm{Q}}\hat{\sigma}_z/2 \tag{4.1}$$

with $\chi = g_+^2 \sin^2\theta/\Delta_+$. The shift $2n\chi$ (n is the number of photon insider the cavity) of the resonator frequency is depicted in Fig. 4.18.

The shift can be detected using two signal sources, see Fig. 4.19. Here, the ZVA is used in the continuous mode at the frequency of the qubit-dependent mode ($\omega_{\mathrm{rf}} = 4.901\,\mathrm{GHz}$).

[11] R&S, ZVA 24

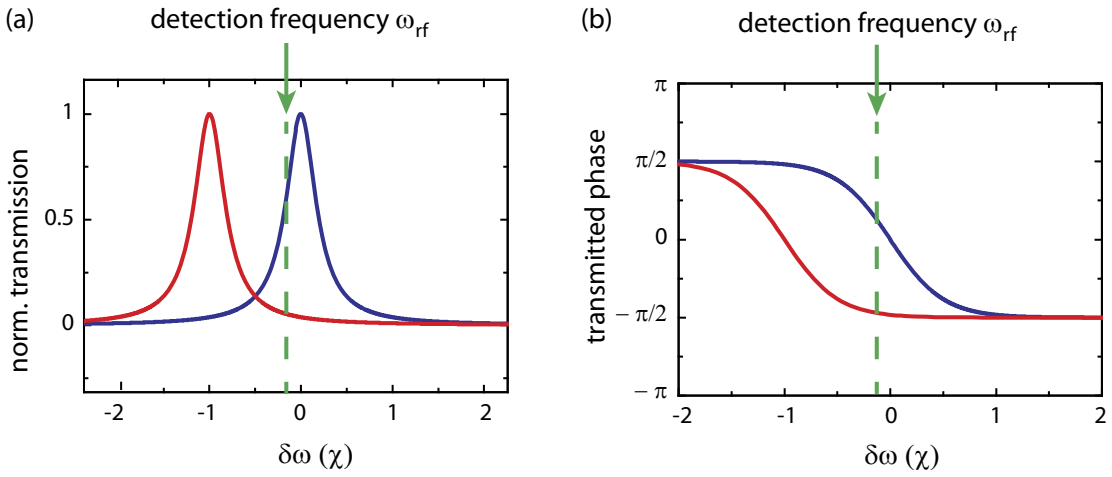

Figure 4.18: Schematic of the dispersive qubit readout: State dependent transmission amplitude (a) and phase (b) of the resonator. Comparing to the eigenfrequency of the resonator when the qubit is in the ground state (blue), the eigenfrequency of the resonator coupled to an exciting qubit is shifted by $2n\chi$.

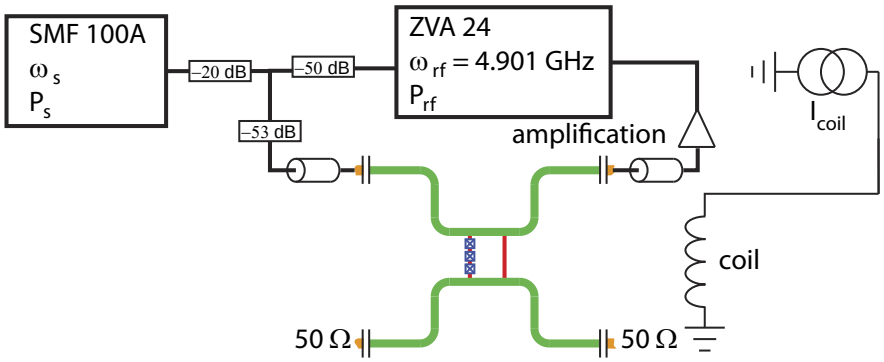

Figure 4.19: Schematic of transmission measurement setup used for two-tone spectroscopy. The frequency ω_{rf} is here at a constant value ($\omega_{\mathrm{rf}} = 4.901\,\mathrm{GHz}$) and a second tone with frequency ω_{s} and power P_{s} is applied to the system.

This signal is called probe or driving tone since it drives the cavity and is close to the maximum transmission of the qubit dependent mode. The SMF, is used to generate the spectroscopy tone which excites and saturates the qubit if $\omega_{\mathrm{s}} \approx \omega_{\mathrm{Q}}$ and the amplitude of the spectroscopy tone is sufficiently large. Eq. 4.1 shows that a qubit excitation leads to a frequency shift of $2n\chi$ which implies a change in the transmission amplitude and the phase of the probe tone as depicted in Fig. 4.18. Summarizing, at a given flux value the resonator response is measured continuously at a given frequency ω_{rf}. By tuning the spectroscopy tone, the qubit is excited if $\omega_{\mathrm{s}} \approx \omega_{\mathrm{Q}}$ and the resonator response (amplitude and phase) changes. Using the coil to tune the external magnetic field, the change of the transmission amplitude can be plotted versus the spectroscopy frequency ω_{rf} and the external flux Φ_{ext}.

Since the AC-Zeeman shift distorts the result of a two-tone spectroscopy by $\delta\omega_{\mathrm{Q}} = 2n\chi$ the measurements have to be performed below the one-photon limit. The one photon

limit is determined in a power calibration of the system. The rearranged Hamiltonian

$$\hat{H} \approx \hbar\omega_+(\hat{a}^\dagger\hat{a} + 1/2) + \hbar[\omega_\mathrm{Q} + 2\chi(\hat{a}^\dagger\hat{a} + 1/2)]\hat{\sigma}_z/2$$

shows how the shifts can be interpreted as shift of the qubit transition frequency due to the presence of the driven cavity. By performing a two-tone spectroscopy at a fixed flux value with varying probe tone power, the photon-number dependent shift is used to calibrate the power of the probe tone.

It is important to note that a two-tone measurement can only be performed in the dispersive regime. As the spectroscopy tone is off-resonant with the cavity, the power has to be 10^3 - 10^4 times higher than for the resonant probe tone. Therefore, a 30 times smaller attenuation at room temperature, see Fig. 4.15, is chosen.

Chapter 5

Experimental Results on the Quantum Switch

After discussing the theoretical background of the quantum switch and discribing the fabrication and the experimental setup, this chapter shows the experimental results. In the first section, the layout of the two-resonator sample without a qubit is specified and spectroscopy measurements performed at 4.2 K give an idea of the spectrum of two coupled resonators. Next, the qubit implemented in the quantum switch is discussed in detail based on two-tone spectroscopy measurements at 50 mK. Finally, transmission measurements through the resonators allow for a detailed description of the quantum switch behavior and the switch setting condition. This is analyzed in section 5.4.

5.1 Two Coupled Resonators

The quantum switch consists of three components; two resonators and one qubit. The direct coupling between the resonators is determined by the sample geometry and constitutes a crucial parameter for the quantum switch. These resonators are realized as superconducting on-chip transmission lines where frequencies up to 10 GHz or higher can easily be achieved.

5.1.1 Design

In this work, the resonators are designed using a coplanar stripline (CSL) geometry, see schematic in Fig. 5.1. In this geometry, a thin metallic line runs along a lateral groundplane. In contrast to coplanar waveguides (CPWs) where a lateral groundplane is on each side of the center strip, the CSL design helps to decrease the direct coupling of the two resonators since a shared groundplane is avoided, see Fig. 5.2. To minimize reflections at the transitions from the sample box connectors to the chip, the feed lines are chosen to be of CPW geometry. The center conductor is interrupted by two gaps. These *coupling capacitors* mark the beginning and the end of the resonator and act similarly to semi-transparent mirrors in optics - they reflect parts of the signal. Since the coupling capacitors do not match the 50 Ω impedance of all commercial components, the design transition from CPW to CSL at this point is not critical.

The characteristic impedance Z_0 of CSL and CPW lines depends mainly on the geometry of the center strip and the groundplane. Only minor contributions come from the used substrate. The geometric layout is optimized towards an eigenfrequency $\omega_R/(2\pi) \approx 5\,\text{GHz}$ for each resonator and a coupling of $g_{AB}/(2\pi) \approx 5 - 10\,\text{MHz}$. The width $w = 7\,\mu\text{m}$

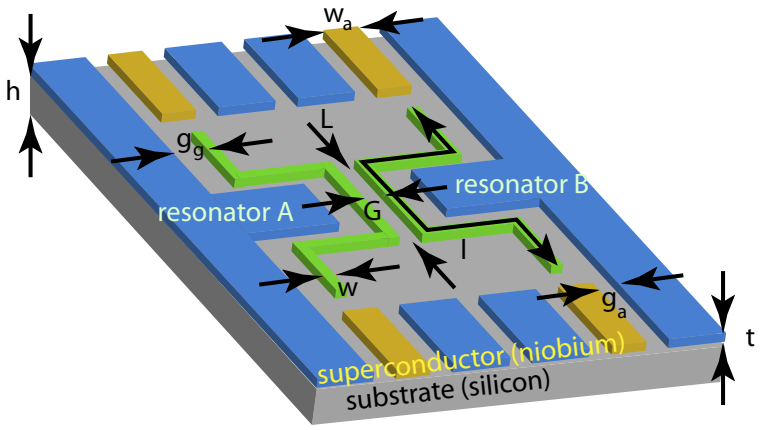

Figure 5.1: (a) Schematic of two CSL resonators (green) on one chip. Both resonators have the same layout (linewidth w, gap between line and groundplane g_g and length l). They are separated by a gap G. The feedlines (orange) are of CPW design (linewidth w_a and gap g_a). The thickness of the niobium structure is t and the thickness of the silicon substrate is h. The groundplane is depicted in blue.

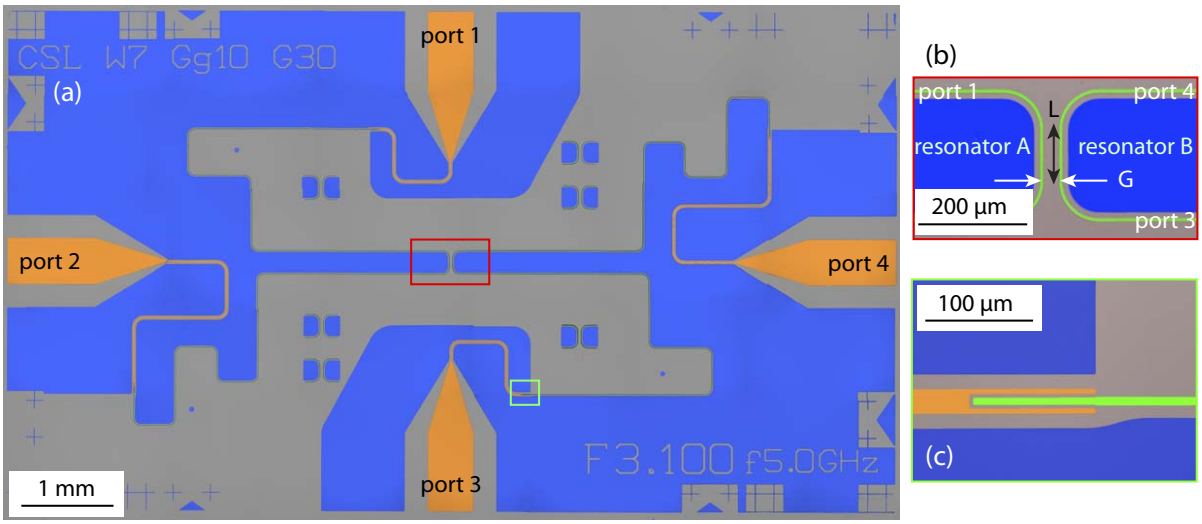

Figure 5.2: (a) False-color micrograph of a chip with two CSL resonators (green lines) and feedlines (orange lines). The blue areas are the ground planes. (b) Zoom of the coupling region. The lines of the resonators (green) are visible in this resolution. They are separated by a gap G and run parallel for a length L. (c) Zoom of one coupling capacitor with gap 3 µm and fingerlength 100 µm, $C_\kappa = 6.2\,\mathrm{fF}$.

of the center strip and the gap $g_g = 10\,\mu\mathrm{m}$ between center strip and ground plane result in a characteristic impedance $Z_0 = 80\,\Omega$ [76]. This mismatch with respect to the $50\,\Omega$-matched feed lines results in a reflection coefficient of 23% [95] at each coupling capacitor.

Comparing the gap width between center strip and groundplane of several micrometers with the length of the resonator ($10 - 20\,\mathrm{mm}$), the reason to call the resonator a quasi-one-dimensional device becomes clear. As a result the mode volume V_m is comparably small and, consequently, the electromagnetic field strength $\mathcal{E} \propto 1/V_\mathrm{m}$ becomes large.

The geometric design of the two-resonator sample is depicted as a false-color picture in Fig. 5.2. Both resonators come closely together at the center of the sample, the so called *coupling region*, see Fig. 5.2(b).

The resonators are fabricated with eigenfrequencies $f_0 = \omega_R/(2\pi)$ in the range of 3.5-6.5 GHz and coupling constants $g_{AB}/2\pi$ of 10-20 MHz. The range of eigenfrequencies results from the length of the resonator varying between 10.86 mm and 15.44 mm. The different capacitors are of finger [see Fig. 5.2(c)] or gap design and cover capacitance values in the range of $C_\kappa = 0.67 - 6.3$ fF[1].

The coupling region is one of the most crucial parts of the two-resonator sample. It defines the geometric coupling between the two resonators and the dimensions of the qubit that will be incorporated. In the coupling region, the two resonators approach each other up to a distance G on a coupling length L. Outside this region, the resonator-resonator coupling is negligible. Although the design values $G = 100\,\mu$m and $L = 400\,\mu$m result in the desired coupling constant of $g \approx 10$ MHz, the qubit dimensions would exceed feasible values. A narrower gap and a decreased length, $G = 30\,\mu$m and $L = 100\,\mu$m, result in similar coupling constants but allow for realistic qubit dimensions. The position of the coupling region at a current antinode and voltage node of the fundamental mode ensures an inductive coupling.

The last characteristic property of the used resonators is their material - niobium. Niobium is a superconductor with a critical temperature $T_c = 9.2$ K. This results in negligible ohmic dissipation [96] already at liquid helium temperature (4.2 K). A characterization at this temperature can be performed with fast turnaround times and thus allows one to refine the layout of the two-resonator chip to guarantee the optimal design of the quantum switch.

5.1.2 Spectroscopy measurements at 4 K

With the setup shown in section 4.2.1 transmission measurements of the two-resonator sample can easily be performed.

Equation (2.20) in section 2.5.3 shows that the transmission spectrum of the two-resonator sample without coupling due to a qubit has two Lorenzian peaks at the frequencies $\omega_- = \omega_R - g_{AB}$ and $\omega_+ = \omega_R + g_{AB}$ [81]:

$$P_{lin}(\omega_+,\omega_-) = \frac{A_+(\kappa/2)^2}{(\omega-\omega_+)^2+(\kappa/2)^2} + \frac{A_-(\kappa/2)^2}{(\omega-\omega_-)^2+(\kappa/2)^2}. \tag{5.1}$$

In general, the transmitted power P_{lin} is plotted on a logarithmic scale $P_{dB} = 10\log(P_{lin})$ and called magnitude. The position of the peaks does not depend on the configuration of the measured and terminated ports as Fig. 5.3 shows. The difference of the amplitude of the measured peaks and the additional dip in two of the spectra may result from classical interference effects or from uncontrolled mismatch at the connectors. This artefact is of minor interest and has no influence on the properties of the quantum switch. The averaged insertion loss of the two-resonator modes at 4 K is approximately -10 dB. The insertion loss depends mainly on two parameters, namely the coupling capacitors and the impedance mismatch between the feedlines and the resonator. While the mismatch simply reduces the transmission through the resonator by 23%, the effect of the coupling

[1] simulated by Sonet Suites ™

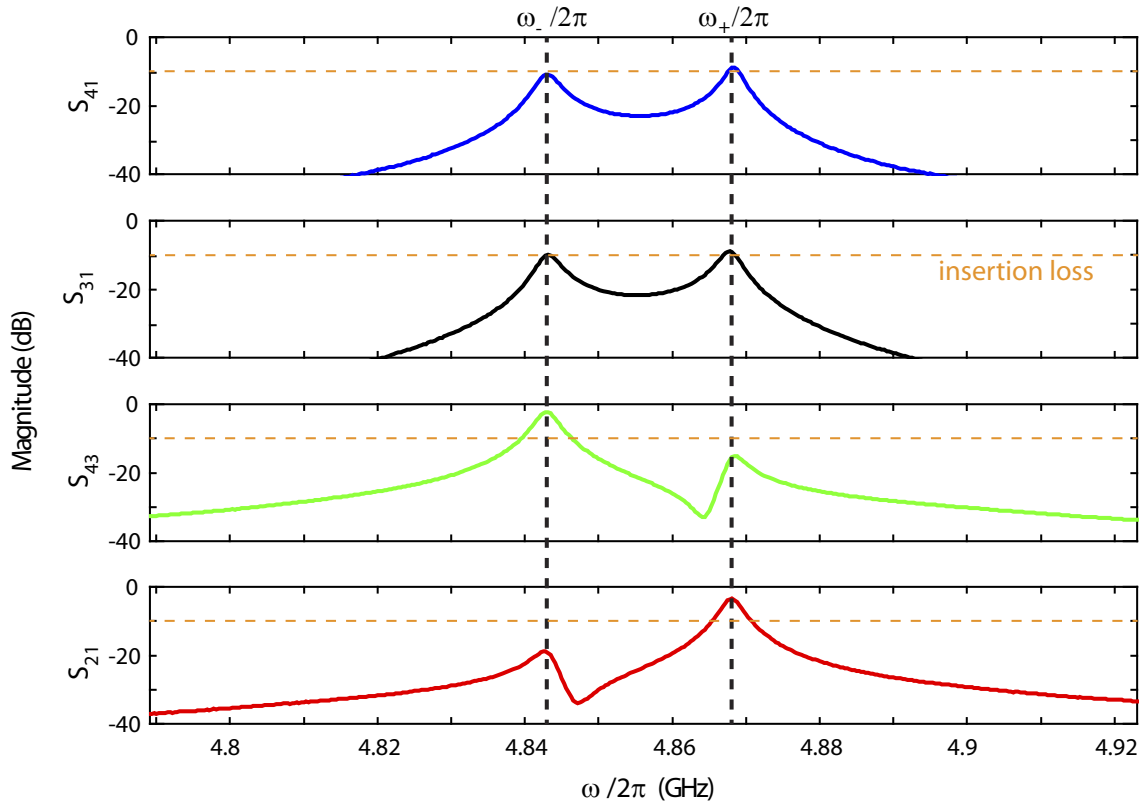

Figure 5.3: Typical transmission spectra of two coupled resonators at $T = 4.2\,\mathrm{K}$. The logarithmic scaled transmitted power P (denoted as magnitude) is plotted as a function of the frequency. Four measurements show that the center frequency ω_0 and the coupling g is independent of the measured port configuration. The design parameters are $w = 7\,\mu\mathrm{m}$, $g_\mathrm{g} = 10\,\mu\mathrm{m}$, $G = 30\,\mu\mathrm{m}$, $L = 100\,\mu\mathrm{m}$, and $l = 11.55\,\mathrm{mm}$.

capacitor on the insertion loss is more complicated. In the limit of $Q_\mathrm{int} \ll Q_\mathrm{ext}$ the insertion loss due to the coupling capacitors can be neglected whereas in the limit $Q_\mathrm{int} \gg Q_\mathrm{ext}$ the insertion loss increases with decreasing coupling capacitance [73]. For $Q_\mathrm{int} \gg Q_\mathrm{ext}$ Figure 5.4 shows how the insertion loss of the measured samples depends on the used coupling capacity. For later experiments, a high signal-to-noise ratio is preferable. Unfortunately, the capacitors with a $2\,\mu\mathrm{m}$ gap are less reproducible than the ones with a $3\,\mu\mathrm{m}$ gap. Therefore, the capacitor design of $100\,\mu\mathrm{m}$ long finger capacitors with a gap of $3\,\mu\mathrm{m}$ is used for the quantum switch, as depicted in Fig. 5.2(c).

5.2 Design of the quantum switch

Based on the design of the two coupled resonators, see section 5.1.1, the actual design for the quantum switch is chosen as follows. The linewidth of the resonators is $w = 7\,\mu\mathrm{m}$ and the gap to the ground planes $g_\mathrm{g} = 10\,\mu\mathrm{m}$. The resonator length $l = 11.55\,\mathrm{mm}$ results in $\omega_\mathrm{R}/(2\pi) = 4.9\,\mathrm{GHz}$. The coupling capacitor is chosen to contain a gap of $3\,\mu\mathrm{m}$ and a finger length of $100\,\mu\mathrm{m}$. The corresponding capacitance is $C_\kappa = 6.3\,\mathrm{fF}$. As the coupling constant is desired to be in the range of $10\,\mathrm{MHz}$, the coupling region is defined by $G = 30\,\mu\mathrm{m}$ and $L = 100\,\mu\mathrm{m}$.

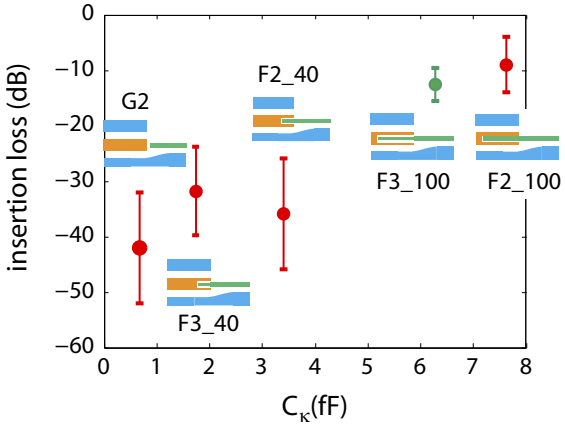

Figure 5.4: Insertion loss versus the calculated capacitances of the coupling capacitors. The inserts sketch the design of the corresponding capacitors. The label denotes the design of the capacitor (finger or gap), the gap distance (2 µm or 3 µm) and in case of a finger capacitor, the length (40 µm or 100 µm) of the finger. The green measurement point marks the design used for the quantum switch.

The qubit is directly implemented between the two resonators. Therefore, the niobium resonator lines have a gap in the coupling region, see Fig 5.5(a). The lines are closed by aluminum connections fabricated in the same step as the qubit, see Fig. 5.5(b). The finite width of the connection is chosen to be 7 µm, adapted to the width of the niobium lines of the resonators. Reducing the width of the connection and forming a constriction would increases the coupling constant g between each resonator and the qubit but reduces the fabrication yield.

The overlap between niobium and aluminum [hatched area in Fig. 5.5(b)] has an area of approximately 560 µm^2. Due to the hard natural oxide which covers the niobium surface, such a large overlap area is necessary. To avoid open circuits at the niobium edges, the two evaporated aluminum layers are altogether 110 nm thick, which is about 10 nm thicker than the niobium layer.

The qubit loop encloses an area of 20×30 µm^2, see Fig. 5.5(c). This is about a factor of two larger compared to former qubit designs at the Walther-Meißner-Institut [81]. This does not affect the qubit in principal but increases the demands on flux stability and might be a source of dephasing due to flux noise.

For two Josephson junctions [Fig. 5.5(d)] the areas are approximately $A_{\mathrm{JJ}} = 0.027$ µm^2 and the third junction is reduced by a factor of $\alpha = 0.70$. The sizes are estimated from SEM pictures taken from comparable qubits. With the measured persistent current, $I_{\mathrm{p}} = (490 \pm 5)$ nA $= \alpha I_{\mathrm{c}}$, see chapter 5.3.2, the estimated ratio of the energies results in $E_{\mathrm{J}}/E_{\mathrm{C}} = 97$.

5.3 Characterization of the components and the system

Before discussing the quantum switch functionality, the exact parameters of the individual components must be well known. A transmission measurement of the quantum switch at a given flux value gives details on the resonators centerfrequency ω_{R}, their coupling g_{AB} and the bandwidths of the individual modes. The qubit of the quantum switch is

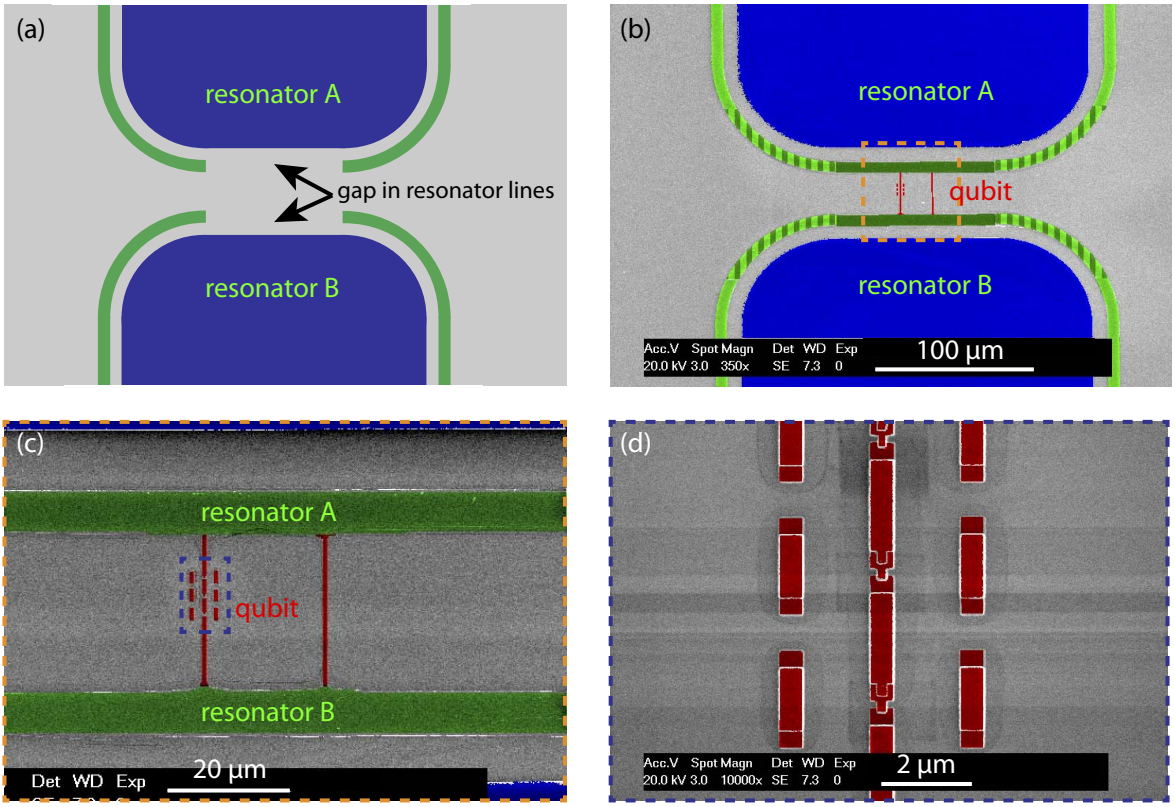

Figure 5.5: (a) CAD layout of the niobium structure of the quantum switch resonators (green) with the gap in the center. (b) Implementation of the qubit (red) between the two resonators. The transition (hatched area) between the niobium part of the resonators (light green) and the aluminum part (dark green) is large to guarantee a good electrical connection. (c) Close up of the qubit. The three Josephson junctions are on one side, the other line closes the loop. (d) Close up of the Josephson junctions.

analyzed in detail using two-tone spectroscopy measurements.

5.3.1 The coupled resonators

A transmission measurement of the coupled resonators at a given flux value Φ_{ext} far away from the qubit's degeneracy point, see Fig. 5.6, shows the *quantum switch modes*. The linear power transmission amplitude versus the frequency is fitted using two Lorenzians [see Eq. (5.1)]. Note that the linear amplitude and the logarithmic magnitude that is often shown Eq. (5.1) can be expressed by $P_{\text{dB}} = 10\log\left(P_{\text{out}}/P_{\text{in}}\right) = 10\log(P_{\text{lin}})$. P_{dB} is also called magnitude. The fitted frequencies are $\omega_-/(2\pi) = 4.8872\,\text{GHz}$ and $\omega_+/(2\pi) = 4.9042\,\text{GHz}$. Thus, the centerfrequency is $\omega_{\text{R}}/(2\pi) = 4.8957\,\text{GHz}$ and the geometric coupling $g_{\text{AB}}/(2\pi) = 8.510\,\text{MHz}$. The full widths at half maximum are fitted as $\kappa_-/(2\pi) = 2.66\,\text{MHz}$ and $\kappa_+/(2\pi) = 2.68\,\text{MHz}$ for the symmetric and antisymmetric mode, respectively. The different amplitudes of the two peaks lead to a lower signal-to-noise ratio concerning ω_+.

An external coil is used to apply an external field perpendicular to the quantum switch. As described in Eq. (3.11), the qubit between the two resonators couples to the ω_+ mode.

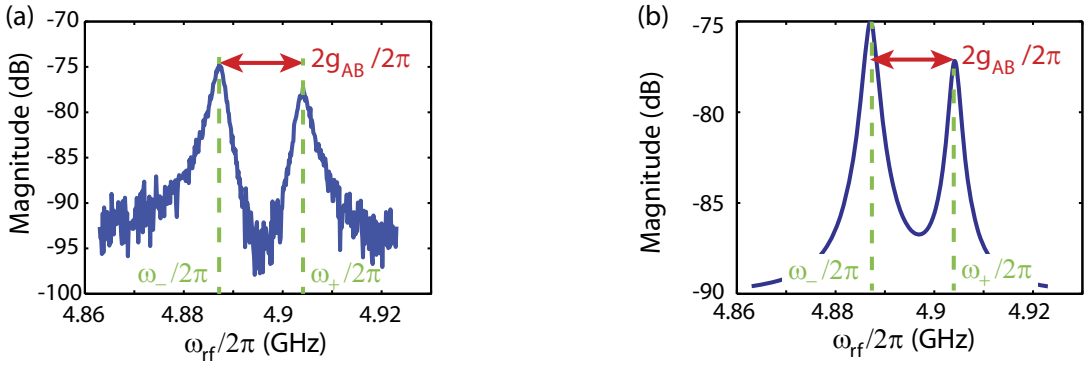

Figure 5.6: Transmission magnitude plotted versus frequency ω_{rf} of the two coupled resonators of the quantum switch. Parameters: $\omega_{\mathrm{R}}/(2\pi) = 4.8957\,\mathrm{GHz}$, $g_{\mathrm{AB}}/(2\pi) = 8.5\,\mathrm{MHz}$, $\kappa_-/(2\pi) = 2.66\,\mathrm{MHz}$ and $\kappa_+/(2\pi) = 2.68\,\mathrm{MHz}$. (a) Measured transmission through the quantum switch sample far away from the degeneracy point. The data is taken at $T = 50\,\mathrm{mK}$, $P_{\mathrm{rf}} = -20\,\mathrm{dBm}$. (b) Two-Lorenzian fit using Eq. (5.1).

This mode is shifted to lower frequencies at $\Phi_{\mathrm{ext}} \approx (n + 1/2)\Phi_0$. This flux periodicity is used to calibrate the applied flux.

5.3.2 Two-tone spectroscopy of the qubit

In the dispersive limit, two-tone spectroscopy is used to investigate the qubit properties. It is important that for a first qubit characterization the qubit frequency is not affected by the AC-Zeeman shift. Therefore, the probe power ω_{rf} for measuring the cavity transmission must be below the single photon limit. The power corresponding to a single photon on average inside the ω_+ mode is $P_{1\,\mathrm{ph}} = \hbar\omega_+\kappa_+/2\pi = 8.71 \times 10^{-15}\,\mathrm{mW} = -140\,\mathrm{dBm}$. Due to the presence of insertion loss, $P_{1\,\mathrm{ph}}$ constitutes an upper bound for the allowed power incident at a quantum switch input port such that the population of the ω_+ mode does not exceed the single-photon level. Based on the calibration procedure in subsection 5.3.3, the insertion loss is estimated to be approximately -20 dBm.

In the following, a two-tone spectroscopy, taken in the low-power range, is used to extract the qubit properties and the interaction parameters between the qubit and the cavity mode. A simple fit considering only one cavity mode can be used as Eq. (3.11) in subsection 3.2.1 implies only an interaction of the qubit and the higher quantum switch mode ω_+.

Measurement data

With a probe tone power of $P_{\mathrm{rf}} = -20\,\mathrm{dBm}$ and $\omega_{\mathrm{rf}} = 4.901\,\mathrm{GHz}$ the population inside the cavity is approximately 0.091 photons on average. A thorough power calibration is discussed in section 5.3.3. Two data sets are presented in Fig. 5.7(a) and Fig. 5.7(b). The spectroscopy power is $P_{\mathrm{s}} = -5\,\mathrm{dBm}$ in (a) which is enough to excite the qubit. Figure 5.7(b) shows a blowup around the cavity frequency. Here a lower power of $P_{\mathrm{s}} = -17\,\mathrm{dBm}$ is chosen. In order to achieve optimal plotting results, the data is normalized as follows. The mean amplitude of the measurements at each measured flux value is subtracted from each measurement at the given flux. In the figure, this procedure is denoted as "deviation of magnitude". The result is a rich spectrum which partly resembles

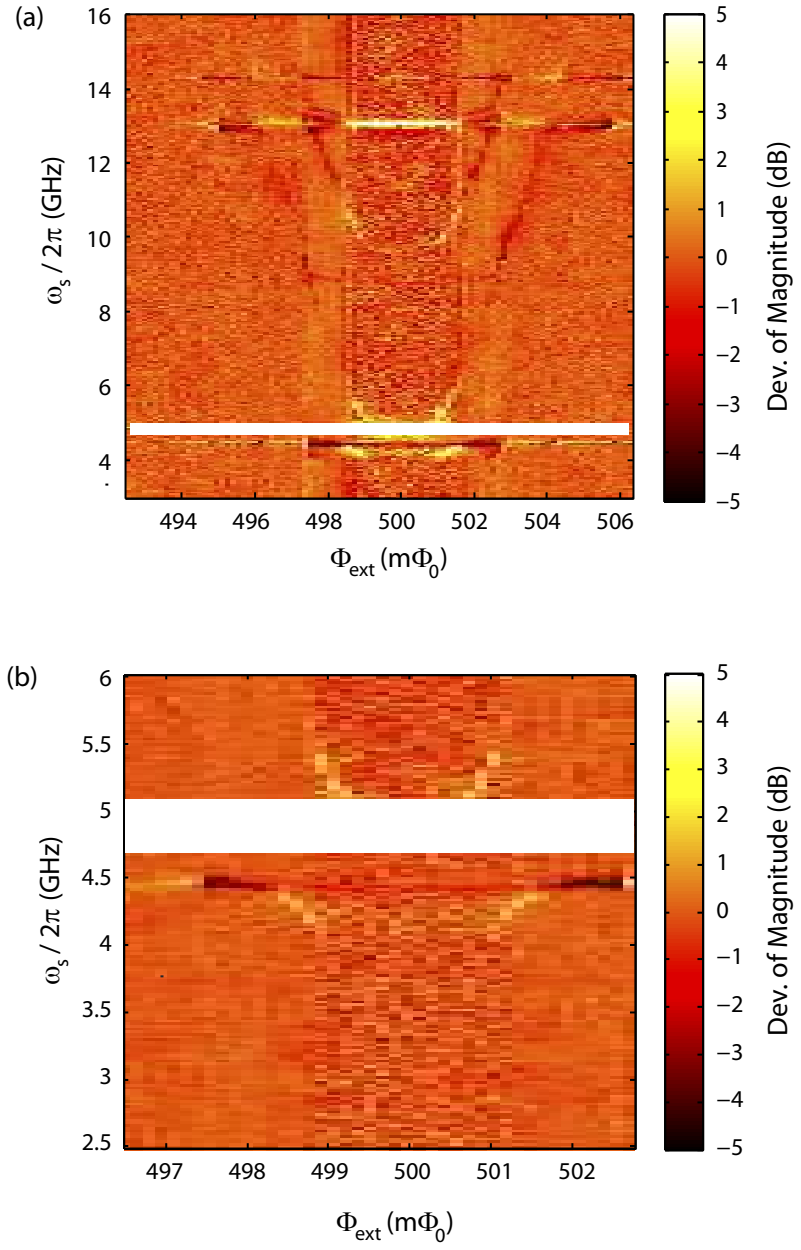

Figure 5.7: Two-tone spectroscopy data in the low-power limit ($T = 50\,\mathrm{mK}$, $P_{\mathrm{rf}} = -20\,\mathrm{dBm}$, $\omega_{\mathrm{rf}} = 4.901\,\mathrm{GHz}$) white areas denote resonant regions. (a) wide range ($P_{\mathrm{s}} = -5\,\mathrm{dBm}$) (b) close-up near the resonator ground mode ($P_{\mathrm{s}} = -17\,\mathrm{dBm}$)

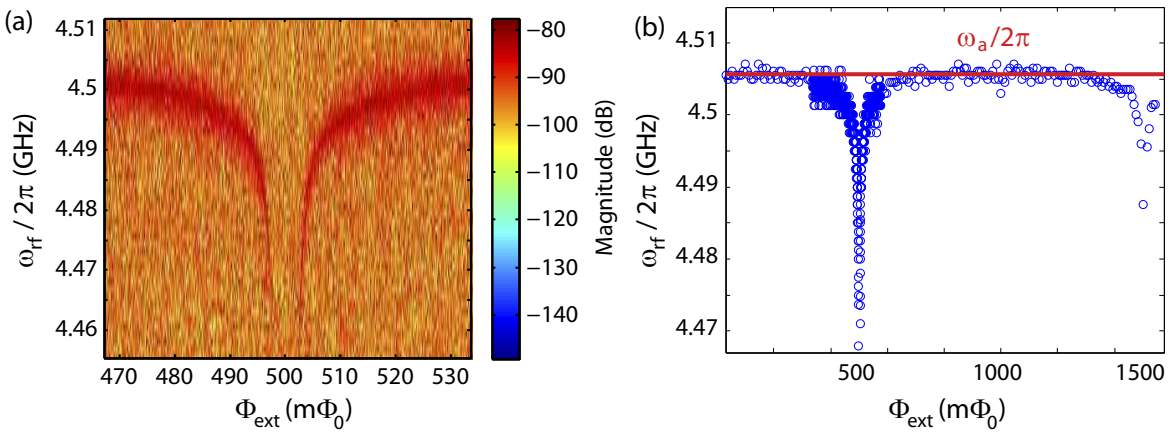

Figure 5.8: (a) Transmission spectroscopy of the additional mode ($T = 50\,\mathrm{mK}$, $P_{\mathrm{rf}} = -20\,\mathrm{dBm}$) (b) Transmission ($T = 50\,\mathrm{mK}$, $P_{\mathrm{rf}} = -20\,\mathrm{dBm}$) on a larger flux range. The red line denotes ω_{a}.

the expected spectrum determined using the quantum switch Hamiltonian Eq. (3.4), see Fig. 3.4.

When discussing the features of this spectrum, one has to keep in mind that two-tone spectroscopy is a dispersive measurement technique. With a coupling constant $g \approx 112\,\mathrm{MHz}$ the frequency range of $4.7 - 5.2\,\mathrm{GHz}$ should not be taken into account. Furthermore, only the ω_+ mode can be used as probing mode because higher harmonics do not fall within the frequency range of $4 - 8\,\mathrm{GHz}$ of the detection chain.

Additional mode

In the two-tone spectroscopy measurements of Fig. 5.7, an *additional mode* which is clearly distinguishable from the quantum switch modes described by Eq. (3.5), appears at $\omega_{\mathrm{a}}/(2\pi) = 4.505\,\mathrm{GHz}$. The existence of this mode is confirmed by transmission spectroscopy, see Fig. 5.8. Its origin lies in the geometry of the sample, namely the galvanic coupling of the qubit to the resonators.

Figure 5.9 depicts a schematic overview of the individual modes. Fig. 5.9(a) and Fig. 5.9(b) are equivalent to the modes discussed in section 2.5.3 (Fig. 2.10). These two modes are the original quantum switch modes that are fully described by the Hamiltonian (3.5). The two additional modes [Fig. 5.9(c) and Fig. 5.9(d)] occur due to the presence of the galvanically coupled qubit. The flux, which is mediated by currents of the out-of-phase oscillating mode, cancels inside at the qubit loop. This mode is equivalent to the mode shown in Fig. 5.9(b) and requires no further investigation. In the case of the in-phase oscillating mode, a finite current is transmitted via the qubit. A detailed analysis of the data shown in Fig 5.8 indicates that this mode cannot be explained by an rf-SQUID-like structure modulating the resonance frequency ω_{R} as a function of the external flux. Instead, the data is consistent with a flux-independent mode, whose frequency is reduced by a Josephson inductance $L_{\alpha\mathrm{J}}$ of the qubit α-junction and which interacts with the qubit at a coupling strength g_{a}. Based on this phenomenological model, the system parameters are derived in the following.

To confirm the model for the modes at ω_{a} it is assumed that the three Josephson

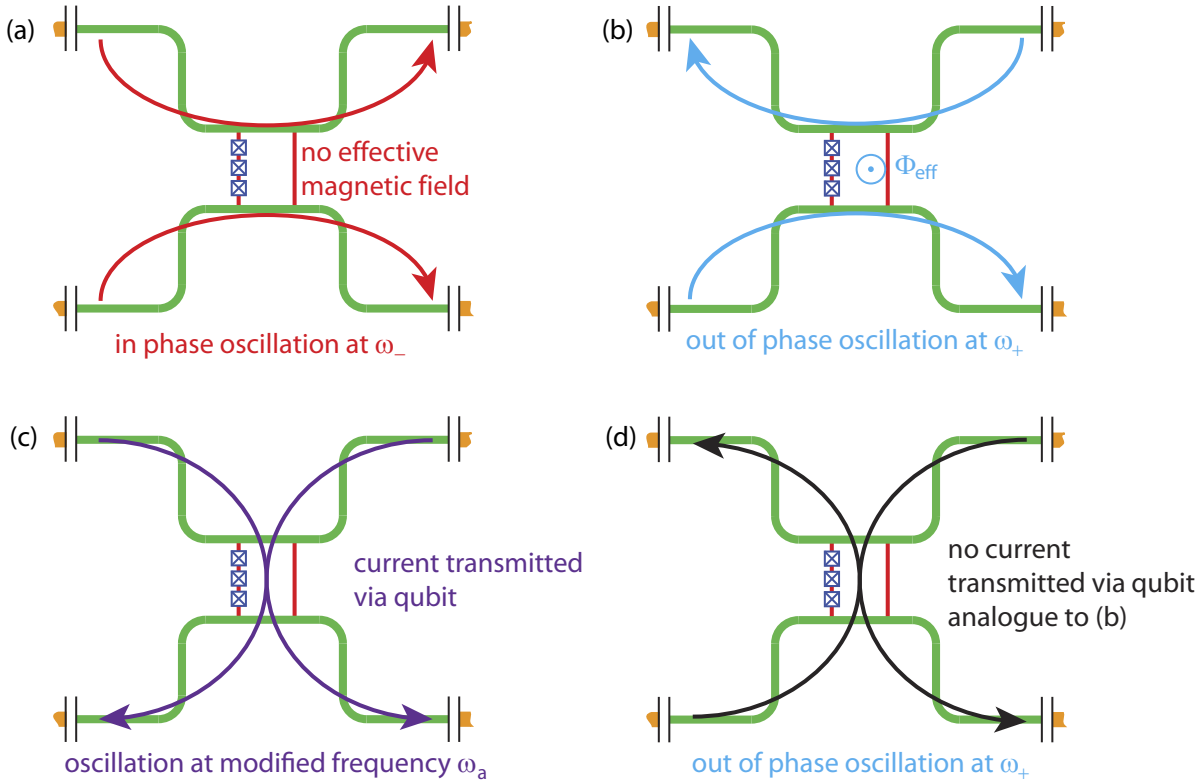

Figure 5.9: Schematic of the quantum switch modes with a galvanically coupled qubit. (a) and (b) are the same modes depicted in Fig. 2.10. In-phase oscillating currents on the resonators lines cause a negligible effective magnetic field between the two resonators as the field generated by resonator A compensates the field generated by resonator B. (b) Out-of-phase oscillating currents on the resonator lines generate an effective magnetic field Φ_{eff} between the lines of the two resonators. (c) In-phase oscillating currents transmitted via the flux qubit. The frequency of this mode is modified by the additional inductance of the qubit resulting in the new eigenfrequency ω_{a}. (d) Out-of-phase oscillating currents flowing over the qubit. The effective transmitted current at the qubit is zero. A modification of the frequency due to the qubit inductance is not necessary. This mode is equivalent to the mode depicted in (b).

junctions add an effective Josephson inductance to the self inductance $L_{\mathrm{tot}} = L_{\mathrm{res}} + L_{\mathrm{eff,JJ}}$. Here, L_{res} is the self inductance of the transmission line parts [see Fig. 5.9(c)], which coincides with the self-inductance of a single resonator. Using

$$\omega_{\mathrm{a}} = \frac{\omega_{\mathrm{R}}}{L_{\mathrm{tot}}/L_{\mathrm{res}}},$$

in analogy to Ref. [97] and Ref. [98], the inductance ratio of $L_{\mathrm{tot}}/L_{\mathrm{res}} = 1.08$ can be derived. Using further $L_{\mathrm{res}} = 7.9\,\mathrm{nH}$ estimated from the resonator design, the effective Josephson inductance is $L_{\mathrm{eff,JJ}} = 0.65\,\mathrm{nH}$. Considering that the Josephson inductance of the α-junction is $L_{\alpha\mathrm{J}} = \Phi_0/(2\pi\alpha I_{\mathrm{c}}) = 649\,\mathrm{pH}$ where $\alpha = 0.7$ and $I_{\mathrm{c}} = 700\,\mathrm{nA}$ is found from the slope of the qubit hyperbola shown in Fig. 5.7, $L_{\mathrm{eff,JJ}} = L_{\alpha\mathrm{J}}$ is found as expected. This is remarkable because it implies that an internal degree of freedom of the three-Josephson-junction arrangement, the qubit, couples to an external one mediating a coupling to the resonator mode ω_{a}. As one will see later, this results indeed in an ultra-strong coupling scenario similar to the one posted in Ref. [81] and Ref. [99].

Due to the geometry of the additional mode, a coupling between this mode and the qubit is expected and the Hamiltonian has to be extended. The resulting Hamiltonian reads

$$\begin{aligned}\hat{H}_{\mathrm{eff}} =& \frac{\varepsilon}{2}\hat{\tilde{\sigma}}_{\mathrm{z}} + \frac{\delta_{\mathrm{Q}}}{2}\hat{\tilde{\sigma}}_{\mathrm{x}} + \hbar\omega_{-}\hat{c}_{-}^{\dagger}\hat{c}_{-} \\ &+ \hbar\omega_{+}\hat{c}_{+}^{\dagger}\hat{c}_{+} + \sqrt{2}\hbar g\hat{\tilde{\sigma}}_{\mathrm{z}}\left(\hat{c}_{+}^{\dagger} + \hat{c}_{+}\right) \\ &+ \hbar\omega_{\mathrm{a}}\hat{d}^{\dagger}\hat{d} + \hbar g_{\mathrm{a}}\hat{\tilde{\sigma}}_{\mathrm{z}}\left(\hat{d}^{\dagger} + \hat{d}\right) \\ &+ 2 \text{ more modes coupled to the qubit,}\end{aligned} \tag{5.2}$$

where $\omega_{\pm} = \omega_{\mathrm{R}} \pm g_{\mathrm{AB}}$. Rotating the Hamiltonian (5.2) into the qubit eigenbasis leads to

$$\begin{aligned}\hat{H}_{\mathrm{eff}} =& \hbar\frac{\omega_{\mathrm{Q}}}{2}\hat{\sigma}_z + \hbar\omega_{-}\hat{c}_{-}^{\dagger}\hat{c}_{-} \\ &+ \hbar\omega_{+}\hat{c}_{+}^{\dagger}\hat{c}_{+} + \sqrt{2}\hbar g\cos\theta\hat{\sigma}_z\left(\hat{c}_{+}^{\dagger} + \hat{c}_{+}\right) - \sqrt{2}\hbar g\sin\theta\hat{\sigma}_x\left(\hat{c}_{+}^{\dagger} + \hat{c}_{+}\right) \\ &+ \hbar\omega_{\mathrm{a}}\hat{d}^{\dagger}\hat{d} + \hbar g_{\mathrm{a}}\cos\theta\hat{\sigma}_z\left(\hat{d}^{\dagger} + \hat{d}\right) - \hbar g_{\mathrm{a}}\sin\theta\hat{\sigma}_x\left(\hat{d}^{\dagger} + \hat{d}\right) \\ &+ 2 \text{ more modes coupled to the qubit.}\end{aligned} \tag{5.3}$$

Here $\hat{d}^{\dagger}$ and $\hat{d}$ are the creation and annihilation operator of the additional mode, respectively. To obtain useful results, it is important not to perform a RWA in first order.

In order to explain the details of Fig. 5.7 at higher spectroscopy frequencies, two more additional modes are added to the Hamiltonian (5.3). Their resonance frequencies $\omega_{2\mathrm{a}}$ and $\omega_{3\mathrm{a}}$ are near two times and three times ω_{a}, respectively. The spectrum of the Hamiltonian is shown in Fig. 5.10(a) and Fig. 5.10(c). To show the clear difference between the original and the modified Hamiltonian, the spectrum of Eq. (3.10) is plotted in Fig. 5.10(b) and Fig. 5.10(d). Both simulations show a switch setting condition, but at different flux values. While the difference between the two Hamiltonians is not very obvious near the fundamental mode, they differ fundamentally in the range of $8 - 10\,\mathrm{GHz}$ and above $13\,\mathrm{GHz}$. High-power measurements in subsection 5.3.4 show that most of the individual

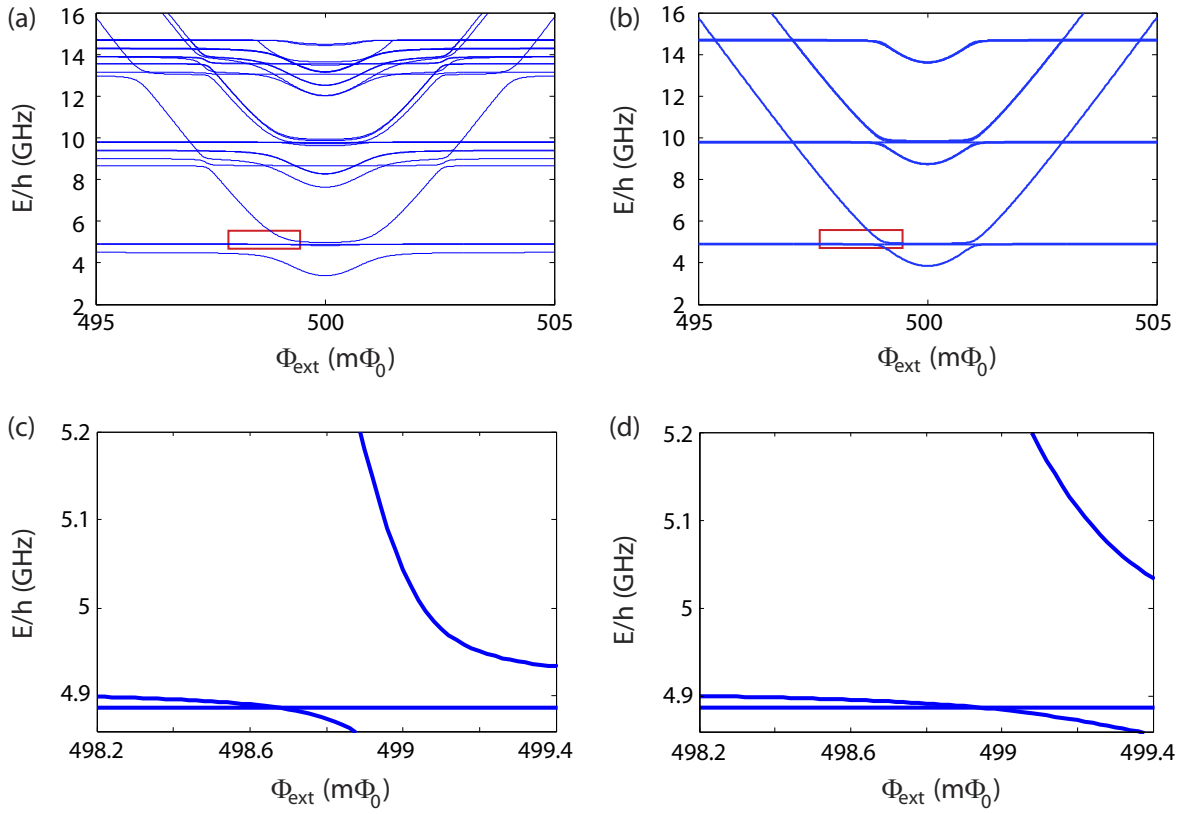

Figure 5.10: Comparison between Hamiltonian (3.10) and Hamiltonian (5.3). Left panel: Mode spectrum of the modified Hamiltonian (5.3) considering the additional mode and two higher harmonics with frequencies ω_{2a} and ω_{3a}. Right panel: Original quantum switch Hamiltonian (3.10) derived in subsection 3.2.1. Lower row: close up of the switching condition. Both models show a crossing of the two resonator modes. Only the exact flux point and the slope show the difference.

features predicted by the extended Hamiltonian of Eq. (5.3) are actually observed. The corresponding frequencies of the individual modes are depicted in Fig. 5.11(a). One sees that the coupling between the qubit and a two photon excitation of the fundamental ω_- mode (labeled as $2\omega_-$) the qubit and the first harmonic of the ω_- mode (labeled as ω_{2-}) vanishes. So does the coupling between the first harmonic of the ω_+ mode (labeled as ω_{2a}) and the qubit. The coupling between the two photon excitation of the ω_+ mode and the qubit is small but finite. The coupling between the qubit and the first harmonic of the additional mode (ω_{2a}) or between the qubit and the two photon excitation of the additional mode ($2\omega_a$) is still present Fig. 5.11(c). Although also for higher modes the switch setting conditions appears, the signals in the actual experiment are typically weak there.

Fitting procedure

Here, the procedure to fit the spectra of Hamiltonian (5.3) to the data shown in Fig. 5.7 is discussed. As two-tone spectroscopy provides no information about the ω_+ cavity mode, which is essential for a proper fit, this lack of information is filled using transmission

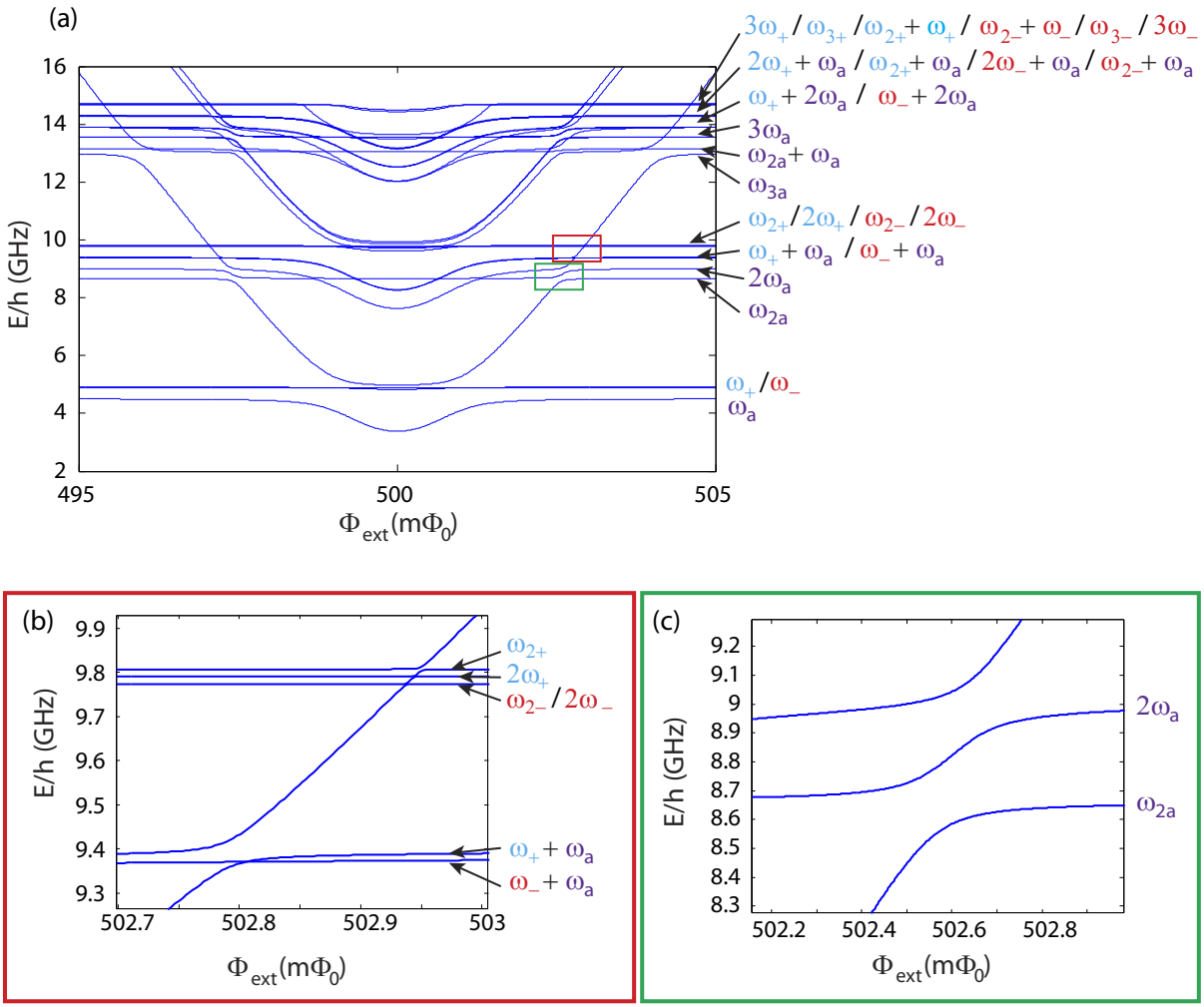

Figure 5.11: (a) As Fig. 5.10(a) but with the transition frequencies indicated. Multiple labels mean that the lines cannot be distinguished due to the limited resolution of the plot. The subscripts + and − denote the splitting of degenerate modes due to the coupling g_{AB}. The different colors (red, blue, violet) denote the different natures of the modes ("−", "+", "a"). Red box / (b): small coupling between the qubit and the original quantum switch modes. Green box / (c): larger coupling between the qubit and the additional $\omega_{2\mathrm{a}}$ mode and large coupling between the qubit and the higher excitation of the ω_{a} mode (labeled as $2\omega_{\mathrm{a}}$).

spectroscopy data which will be discussed in section 5.4. To reduce inaccuracies, the additional mode is fitted using the transmission spectroscopy data shown in Fig. 5.8. The lower quantum switch mode at ω_-, which does not couple to the qubit, can be neglected in the fitting procedure. This reduces the size of the Hilbert space and the fitting becomes more efficient.

Figure 5.12 shows the data points used for the fitting procedure (open circles) and the fit. The measurement from Fig. 5.7 is depicted as background. The fitting parameters are summarized in Tab. 5.1. The resulting qubit parameters are $I_{\mathrm{p}} = (490 \pm 5)\,\mathrm{nA}$ and $\delta/h = (3.9 \pm 0.1)\,\mathrm{GHz}$. The fitted coupling $g_+/(2\pi) = (159 \pm 10)\,\mathrm{MHz}$ of the ω_+ mode with the qubit gives the coupling between a single resonator and the qubit as $g/(2\pi) = (112 \pm 7)\,\mathrm{MHz}$.

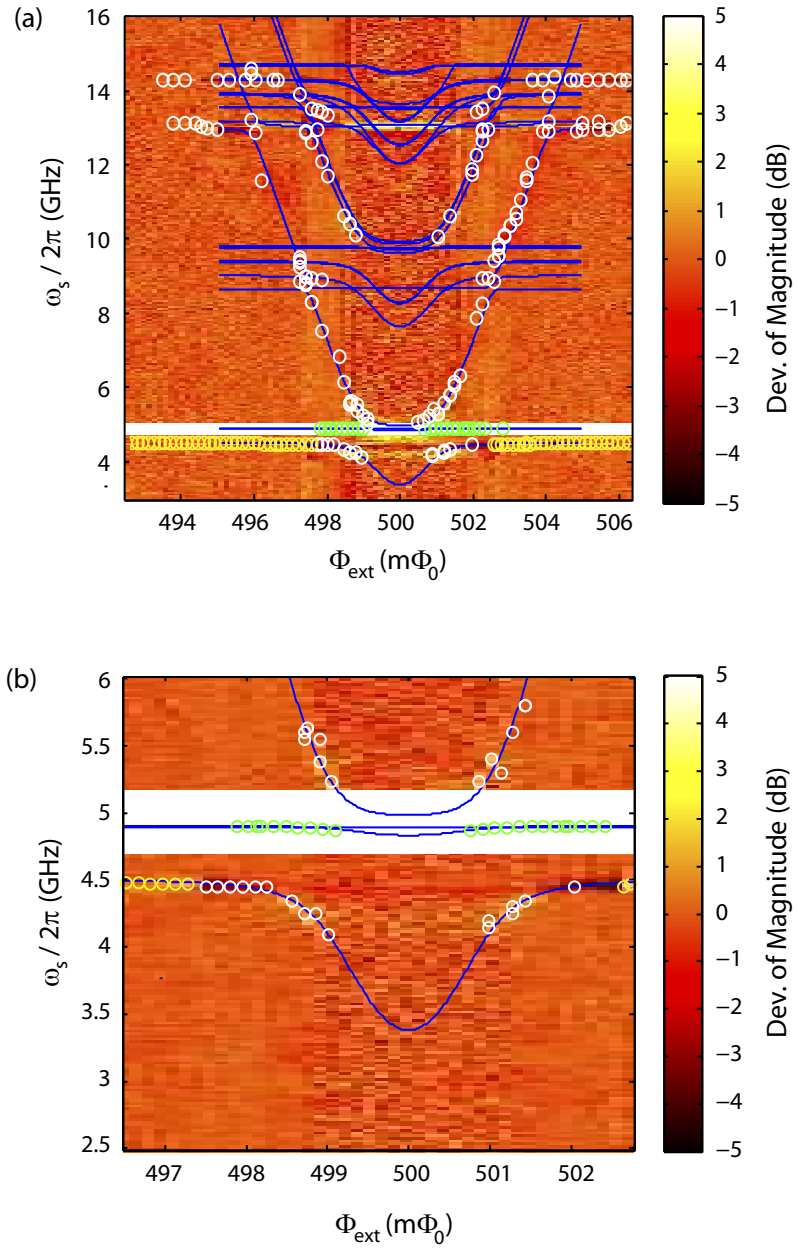

Figure 5.12: Fit (blue lines) of the spectrum of Hamiltonian (5.3) to the data from Fig. 5.7 ($T = 50\,\mathrm{mK}$, $P_{\mathrm{rf}} = -20\,\mathrm{dBm}$, $\omega_{\mathrm{rf}} = 4.901\,\mathrm{GHz}$, $P_{\mathrm{s}} = -5\,\mathrm{dBm}$ [Fig. 5.7(a)] and $P_{\mathrm{s}} = -17\,\mathrm{dBm}$ [Fig. 5.7(b)]) (white circles) and Fig. 5.8 ($T = 50\,\mathrm{mK}$, $P_{\mathrm{rf}} = -20\,\mathrm{dBm}$) (yellow circles). Transmission data on the ω_+-mode is indicated by green open circles ($T = 50\,\mathrm{mK}$, $P_{\mathrm{rf}} = -20\,\mathrm{dBm}$).

Parameters	Fitted value	Comment
$\omega_\mathrm{R}/(2\pi)$	4.8957 GHz	
$g_\mathrm{AB}/(2\pi)$	8.5 MHz	
δ_Q/h	3.87 GHz	
ε/h	$3.075(\Phi_\mathrm{ext} - 0.5\Phi_0)$GHz	$\Rightarrow I_\mathrm{p} = 490\,\mathrm{nA}$
$g_+/(2\pi)$	159 MHz	$\Rightarrow g/(2\pi) = 112\,\mathrm{MHz}$
$\omega_\mathrm{a}/(2\pi)$	4.5 GHz	
$g_\mathrm{a}/(2\pi)$	670 MHz	
$\omega_\mathrm{2a}/(2\pi)$	8.66 GHz	
$g_\mathrm{2a}/(2\pi)$	$100 - 600\,\mathrm{MHz}$	Not reliable
$\omega_\mathrm{3a}/(2\pi)$	13 GHz	
$g_\mathrm{3a}/(2\pi)$	$1.1 - 1.2\,\mathrm{GHz}$	Not reliable

Table 5.1: Characteristic parameters of the quantum switch. The parameters are found using the described fitting procedure with three different datasets.

The coupling of the additional mode turns out to be $g_\mathrm{a} = 670\,\mathrm{MHz}$ which implies $g_\mathrm{a}/\omega_\mathrm{a} = 0.15$. According to Ref. [81], this corresponds to the ultrastrong coupling regime where the rotating wave approximation (RWA) breaks down. This is not unreasonable because, as in Ref. [81], the qubit-mode coupling is mediated by a Josephson inductance. However, a check for unambiguous spectroscopy features providing the RWA violation cannot be performed. The used amplification chain does not allow for transmission spectroscopy of higher modes. The values for the coupling strength between qubit and higher modes are not reliable, as only a few points are found in the measurements which are used for fitting. Especially the coupling between the qubit and the ω_2a mode cannot be fitted reliably. Nevertheless, these values are stated as order-of-magnitude estimations. Although the current distribution of ω_2a-mode is expected to be zero at the center of the resonators, the coupling is not negligible but finite. The nature of this coupling is presently not understood yet.

The coupling of the second harmonic of the additional mode is of the same nature as the coupling of the fundamental one. Thus, this mode is identified with the higher mode of ω_a and the coupling constant g_3a can be determined as

$$g_\mathrm{3a} = \sqrt{\frac{\omega_\mathrm{3a}}{\omega_\mathrm{a}}}\, g_\mathrm{a}.$$

The result of 1.14 GHz agrees very well with the coupling constant found in the fit (see Tab. 5.1).

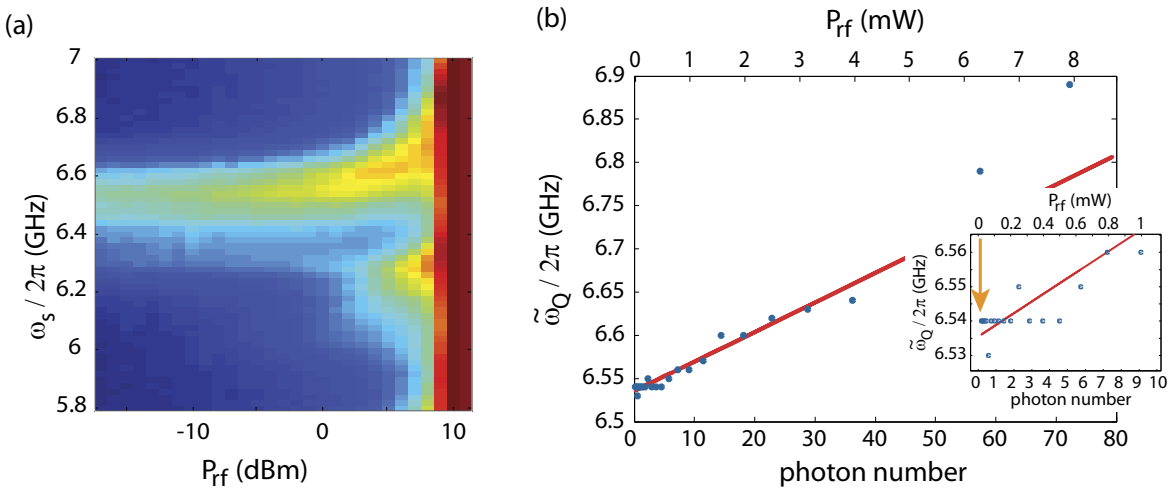

Figure 5.13: Qubit AC-Zeeman shift: (a) Spectroscopy tone versus probe tone power P_{rf} ($T = 50\,\mathrm{mK}$, $\omega_{\mathrm{rf}} = 4.901\,\mathrm{GHz}$, $P_{\mathrm{s}} = 8\,\mathrm{dBm}$). The qubit response is at constant frequency values for $P_{\mathrm{rf}} < P_{\text{one photon in cavity}}$. (b) Shifted frequency $\tilde{\omega}_{\mathrm{Q}}$ as a function of the photon number inside the cavity. Red line: Fit of the linearly increased frequency shift. Close-up: The orange arrow marks the power P_{rf} of Fig. 5.7.

5.3.3 Power calibration

For the exact interpretation of the following measurements, knowledge on the probe power is essential. Unfortunately, a power calibration is not performed during the cooldown where the spectroscopy data has been measured. One of the main reasons for the missed measurement is the absence of flux stability. During a second cooldown approximately 30 datasets are measured and averaged. The attenuation of the rf-signal lines and the insertion loss of the resonators can be assumed to be nearly unchanged between the cooldowns. The attenuator configuration is well known in both cooldowns. Hence, this calibration measurement can be used to identify the population of the readout mode for the data from the first cooldown with sufficient accuracy.

Using the setup of a two-tone measurement, the qubit frequency is detected while the power of the probe mode is tuned. According to Ref. [84], the ac-Zeeman shift of the qubit mode does not only depend on the qubit state but also on the number of photons n inside the cavity, see Eq. (3.3),

$$\tilde{\omega}_{\mathrm{Q}} = \omega_{\mathrm{Q}} + (2n+1)\chi,$$

where $\chi = (g_+ \sin\theta)^2/\Delta_+$, Δ_+ denotes the detuning between the qubit and the ω_+ mode and g_+ the coupling between the qubit and this mode. The approximation holds at low photon numbers as long as $n < \Delta_+^2/(4g_+^2 \sin^2\theta)$.

The qubit AC-Zeeman shift is measured at $\Phi_{\mathrm{ext}} = 498.12\,\mathrm{m}\Phi_0$, see Fig. 5.13. In general, it is useful to perform this measurement at the qubit degeneracy point since there flux noise is minimal. However, the visibility of the qubit at this flux point is suppressed, possibly due to the existence of the additional mode. The AC-Zeeman shift at $\Phi_{\mathrm{ext}} = 498.12\,\mathrm{m}\Phi_0$ for one photon is found to be $2\chi = 3.41\,\mathrm{MHz}$. Using the data presented

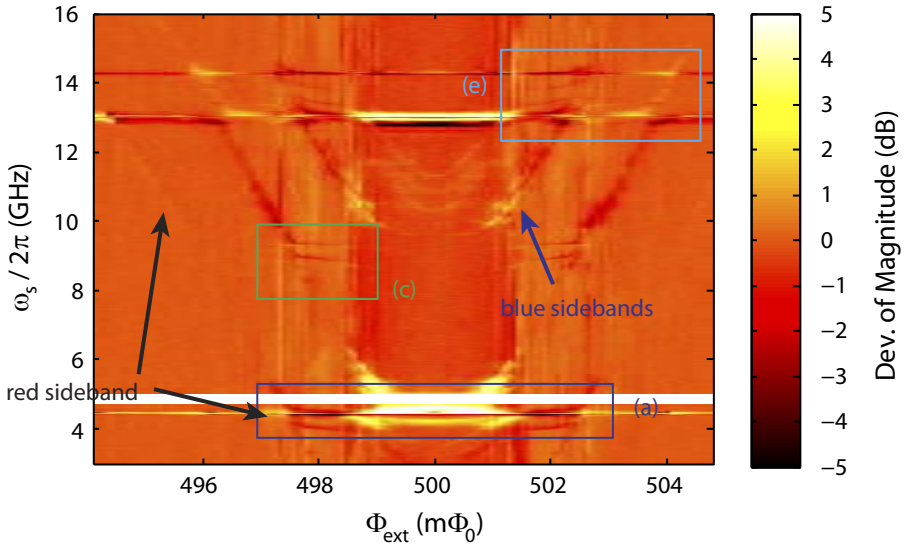

Figure 5.14: Wide range two-tone spectroscopy in the high power regime. Using a probe power of $P_{\mathrm{rf}} = -2\,\mathrm{dBm}$, the cavity is populated with 5.7 photons on average. The spectroscopy power is chosen to be $P_{\mathrm{s}} = -9\,\mathrm{dBm}$ ($T = 50\,\mathrm{mK}$, $\omega_{\mathrm{rf}} = 4.901\,\mathrm{GHz}$). The colored boxes mark the flux and frequency rage that is chosen for the measurements depicted in Fig. 5.16.

in Fig. 5.13 and fitting the linear part, the frequency shift corresponding to the power of n photons is given by the relation $2n\chi = \xi P_{\mathrm{rf}}$, where $\xi = 31\,\mathrm{MHz/mW}$ denotes the slope of the linear increase. Using this relation, the power required to populate the cavity with one photon is $P_{\mathrm{rf}} = 0.11\,\mathrm{mW}$. This power value is equivalent to $P_{\mathrm{rf}} = -9.6\,\mathrm{dBm}$. The used probe tone power of Fig. 5.7, which is $P_{\mathrm{rf}} = -20\,\mathrm{dBm}$, is marked by an orange arrow in Fig 5.13(b). This power populates the cavity with approximately 0.091 photons. This shows that the AC-Zeeman shift during the calculation of χ can be neglected and does not affect the qubit or the cavity frequency ω_{Q} or ω_{+}.

5.3.4 Entering the high power regime

By increasing the power of the probe tone, the AC-Zeeman shift can no longer be neglected. Despite sideband transitions a few other aspects make measurements in the high power regime attractive. The signal-to-noise ratio is increased so that some low visibility features can be resolved more precisely. In the following, these features will be discussed and compared with the theory.

Sidebands

Based on the resonator frequencies, the additional mode frequency and the qubit transition frequency, sideband transitions can be allocated. Figure 5.14 shows a complete spectrum in a wide flux and frequency range. The probe power P_{rf} here is chosen as $P_{\mathrm{rf}} = -2\,\mathrm{dBm}$; the cavity is populated by 5.7 photons on average. The spectroscopy power is $P_{\mathrm{s}} = -9\,\mathrm{dBm}$.

The qubit hyperbola can be identified with the blue sideband transitions for the

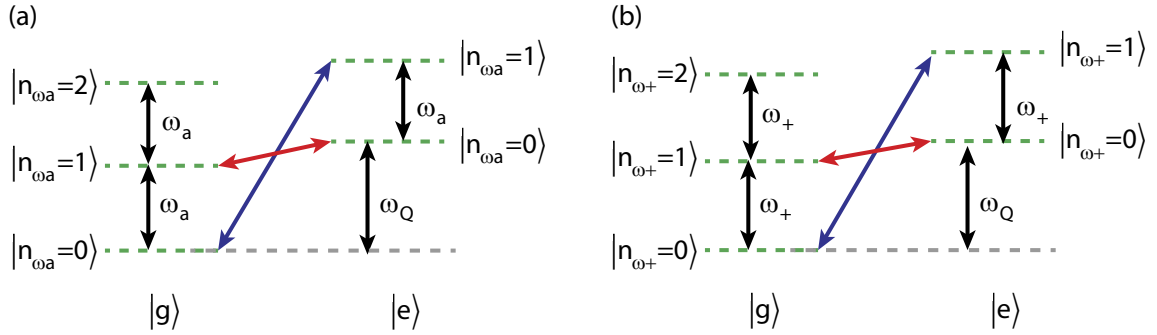

Figure 5.15: Sideband transitions. Not only the qubit transition $|g\rangle \rightarrow |e\rangle$ occurs in two-tone spectroscopy. Also sideband transitions as blue sideband transitions $|g,n_{\omega a}=0\rangle \rightarrow |e,n_{\omega a}=1\rangle$ (a) and $|g,n_{\omega+}=0\rangle \rightarrow |e,n_{\omega+}=1\rangle$ (b) and red sideband transitions $|g,n_{\omega a}=1\rangle \rightarrow |e,n_{\omega a}=0\rangle$ (a) and $|g,n_{\omega+}=1\rangle \rightarrow |e,n_{\omega+}=0\rangle$ (b) are activated.

frequencies $\omega_+ + \omega_Q$ [$|g,n_{\omega+}=0\rangle \rightarrow |e,n_{\omega+}=1\rangle$, see Fig. 5.15(b)] and $\omega_a + \omega_Q$ [$|g,n_{\omega a}=0\rangle \rightarrow |e,n_{\omega a}=1\rangle$, see Fig. 5.15(a)]. This sideband can also be verified in low power measurements as a pre-excitation of the qubit or the resonators is not necessary.

In contrast to the blue sideband transition, the red sideband is only visible in high power spectroscopy data. Figure 5.14 shows the red sideband transition $|g,n_{\omega+}=1\rangle \rightarrow |e,n_{\omega+}=0\rangle$.

Better resolution of individual features

Using a high power probe tone and therefore a good signal-to-noise ratio, the resolution of the measurements can be increased. Figure 5.16 provides insight into transitions between the states. As the data is detected using a high power probe tone, the actual datapoints may differ from the theoretical prediction. The overview in Fig. 5.14 helps to find the different close ups in the spectrum. The different energy modes are labeled in the form of their excitations as $|Q,n_{\omega+},n_{\omega 2+},n_{\omega 3+},n_{\omega a},n_{\omega 2a},n_{\omega 3a}\rangle$. Q marks the excitation of the qubit as $|g\rangle$ or $|e\rangle$ followed by the excitations of the three lowest quantum switch modes. The excitations of the flux independent ω_- mode is not taken into account as it is not detectable using two-tone spectroscopy. The last three numbers correspond to the excitation of the three additional modes.

In a high resolution measurement, the low-frequency range [Fig. 5.16(e) and Fig. 5.16(f)] shows exactly the flux response of the additional mode. Again, the resonant regime should not be taken into account as two-tone spectroscopy is a dispersive measurement technique. Despite blue sideband transitions $|g,n_{\omega+}=0\rangle \rightarrow |e,n_{\omega+}=1\rangle$ and $|g,n_{\omega a}=0\rangle \rightarrow |e,n_{\omega a}=1\rangle$ which are detectable for low spectroscopy power, the red sideband transition $|g,n_{\omega+}=1\rangle \rightarrow |e,n_{\omega+}=0\rangle$ is visible only in the high-power regime.

At approximately 9−10 GHz the ω_{2a} mode interacts with the qubit, see Fig. 5.16(c) and Fig. 5.16(d). As the magnetic field for this mode is zero at the center of the resonators, it is not plausible to identify this mode with the first harmonic of the additional mode as the frequency range would suggest. Therefore, the exact nature of this mode remains unclear. The qubit transition frequency and two blue sideband transitions can also be observed.

Above 13 GHz, the non-linear frequency spacing of the additional mode starts to play

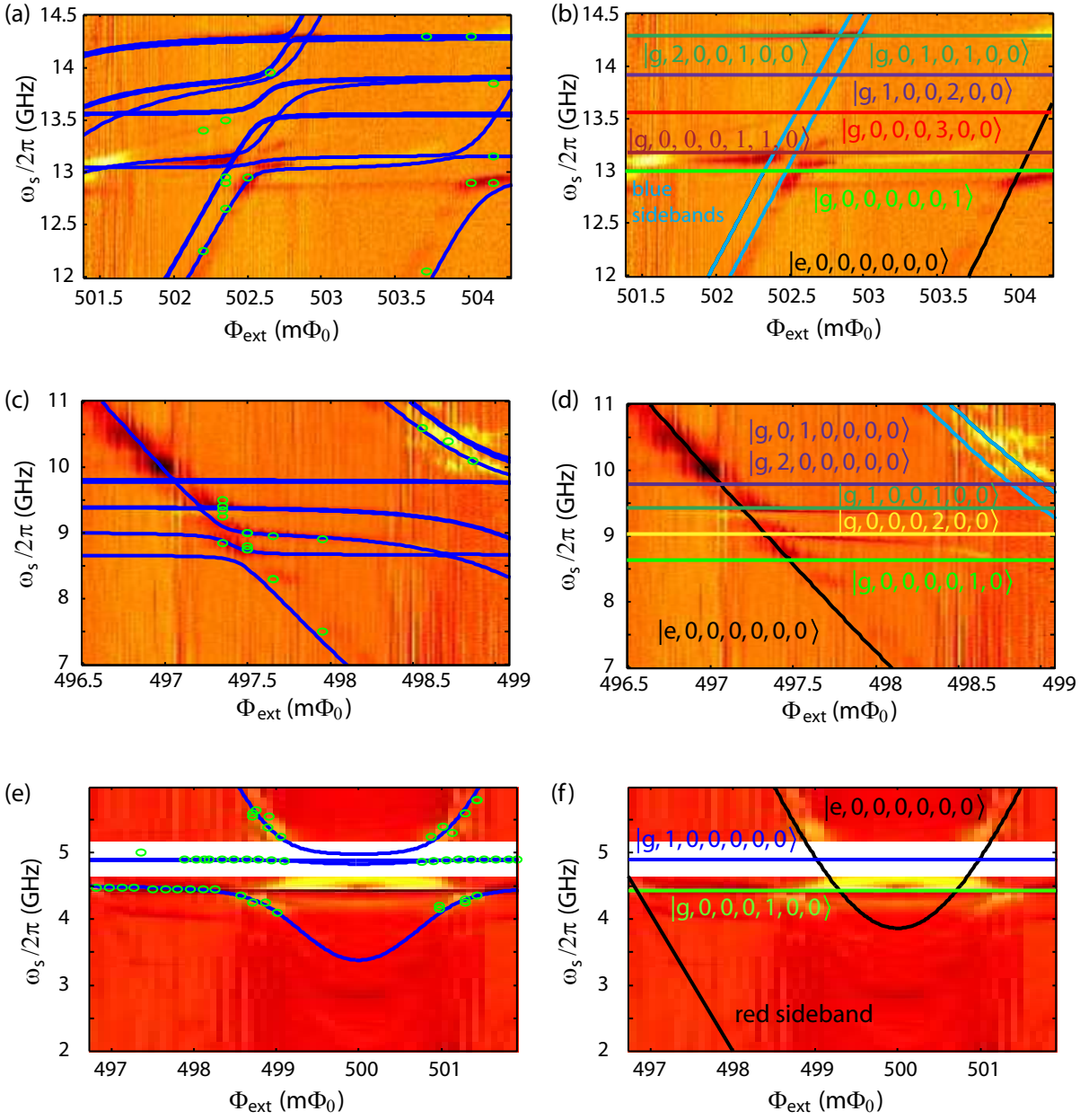

Figure 5.16: High resolution data of individual transitions taken at $T = 50\,\mathrm{mK}$, $\omega_{\mathrm{rf}} = 4.901\,\mathrm{GHz}$, (a) $P_{\mathrm{s}} = -16\,\mathrm{dBm}$, $P_{\mathrm{rf}} = -10\,\mathrm{dBm}$ (0.91 photons inside the cavity), (c) $P_{\mathrm{s}} = -7\,\mathrm{dBm}$, $P_{\mathrm{rf}} = 0\,\mathrm{dBm}$ (9.1 photons inside the cavity), (e) $P_{\mathrm{s}} = -7\,\mathrm{dBm}$, $P_{\mathrm{rf}} = 0\,\mathrm{dBm}$ (9.1 photons inside the cavity). The colored boxes in the overview in Fig. 5.14 depicts where the individual plots are located in the flux frequency plane. The corresponding states are labeled as $|Q, n_{\omega+}, n_{\omega 2+}, n_{\omega 3+}, n_{\omega \mathrm{a}}, n_{\omega 2\mathrm{a}}, n_{\omega 3\mathrm{a}}\rangle$. Left panel: measured data (color coded) and simulation. The dots are depicting the data taken in the low power limit. Right panel: Uncoupled levels of the qubit, the resonator modes and their higher harmonics. Blue lines in (b) are the blue sideband transitions $|g,n_{\omega+} = 0\rangle \rightarrow |e,n_{\omega+} = 1\rangle$ and $|g,n_{\omega a} = 0\rangle \rightarrow |e,n_{\omega a} = 1\rangle$.

an important role. The spectrum becomes very feature rich. As the theoretical prediction of the Hamiltonian (5.3) follows qualitatively the measurements, and the mode spectrum at $13 - 14\,\mathrm{GHz}$ does not significantly influence the quantum switch parameters near the fundamental modes, further investigations on the nature of the additional mode are of minor interest for this work.

Summarizing, the high power measurements confirm, despite small shifts induced by the drive itself, the spectrum of the Hamiltonian in Eq. (5.3).

5.4 Resonator transmission of the quantum switch

After discussing the resonator and the qubit in the previous section, in this section the transmission of the quantum switch and its properties are analyzed.

5.4.1 Transmission through the quantum switch

The transmission through the device is for technical reasons always measured between port one and two of the same resonator, whereas port three and four are $50\,\Omega$-terminated, see Fig 4.15. Away from the qubit degeneracy point, the transmission spectroscopy shows a double peak spectrum with $\omega_\mathrm{R}/(2\pi) = 4.8957\,\mathrm{GHz}$ and $g_\mathrm{AB}/(2\pi) = 8.510\,\mathrm{MHz}$.

In the following transmission measurements, the spectroscopy tone was chosen to be in the low power regime at $P_\mathrm{rf} = -20\,\mathrm{dBm}$ to ensure the qubit being in the ground state. This is necessary since the switch setting condition $g^2 \sin^2\theta/\Delta + g^2 \sin^2\theta/\Sigma = g_\mathrm{AB}$ can only be fulfilled when the qubit is in its ground state $|\mathrm{g}\rangle$ and the ω_+-mode is negligibly populated.

The result of the transmission measurements versus applied flux is shown in Fig. 5.17. Tuning the external flux through the degeneracy point of the qubit, the frequency of the ω_+ mode starts to decrease, and crosses the ω_- mode, see Fig. 5.17(a). This crossing appears twice, symmetrically with respect to the degeneracy point at $498.9\,\mathrm{m}\Phi_0$ and

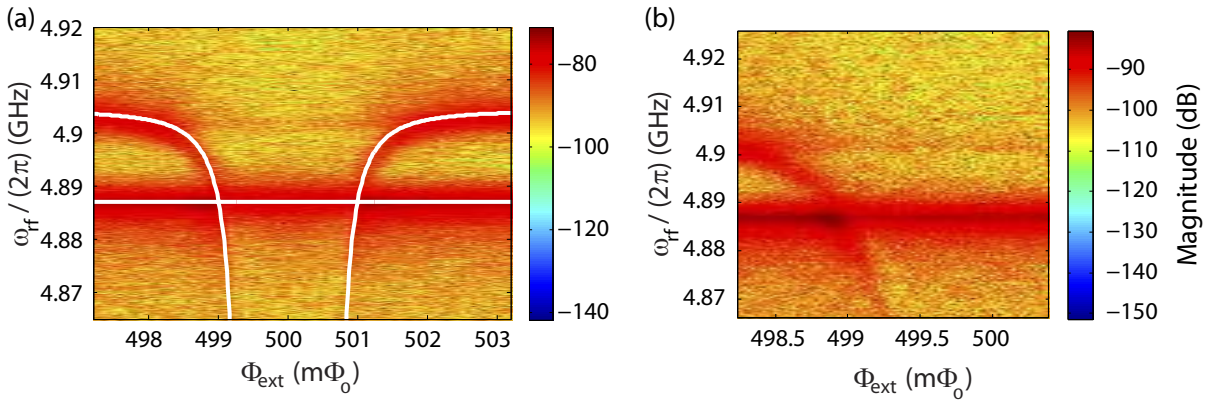

Figure 5.17: Transmission spectroscopy of the quantum switch versus the applied flux at $T = 50\,\mathrm{mK}$ and $P_\mathrm{rf} = -20\,\mathrm{dBm}$. (a) Flux range from $497\,\mathrm{m}\Phi_0$ to $512\,\mathrm{m}\Phi_0$; White line: theory prediction based on the full Hamiltonian (5.3) (b) Close-up on the switch setting condition. Due to the absence of an anti-crossing, the two resonators can be assumed to be decoupled.

501.1 mΦ_0. These points fulfill the switch setting conditions. The high resolution measurement in Fig. 5.17(b) shows with the resolution set by κ_+ and κ_-, a clear crossing and not an anti-crossing of the two modes at this point.

Using the relation of the switch setting condition derived from the original model (see chapter 3.2) the comparison with the measurements holds some surprises. Here, $\Delta = 240\,\mathrm{MHz}$, $\Sigma = 10.05\,\mathrm{GHz}$ and $g\sin\theta = 84\,\mathrm{MHz}$ gives $g^2\sin^2\theta/\Delta + g^2\sin^2\theta/\Sigma = 30.3\,\mathrm{MHz}$. This number differs by a factor of approximately 3.5 from $g_{\mathrm{ab}} = 8.5\,\mathrm{MHz}$. The deviation between the measurement, where the switch setting condition is obviously fulfilled, and the theoretical prediction from chapter 3.2 shows that the geometry and thus, the existence of the additional mode has to be included into the model. Theory prediction [see Fig. 5.17(a)] using the full Hamiltonian agrees quite well with the measured mode. This is another indication that the Hamiltonian (5.3) describes the quantum switch properly.

5.4.2 Fitting procedure of the transmission spectrum

Further analysis concerning the mode splitting requires consolidated knowledge about the parameters of the cavity Lorentzians. Using Eq. (5.1)

$$P_{\mathrm{lin}}(\omega_+,\omega_-) = \frac{A_+(\kappa/2)^2}{(\omega-\omega_+)^2+(\kappa/2)^2} + \frac{A_-(\kappa/2)^2}{(\omega-\omega_-)^2+(\kappa/2)^2},$$

each spectrum at a given flux value is fitted independently. It is important to note that the Lorentzian double peak spectrum of Eq. (5.1) defines the magnitude of the linear power. The data depicted in Fig. 5.17 is shown in a logarithmic scale. Close to the switch setting condition, the distance of the Lorentzians is smaller than their full width at half maximum $\kappa/(2\pi)$. To perform a fit also in this region, the procedure is divided into two steps. First the flux-independent mode at $\omega_- = 4.887\,\mathrm{GHz}$ is fitted and an averaged mode of the undisturbed ω_- peak is calculated using the fitting results away from the switch setting condition. This averaged mode is subtracted from the complete spectrum and only the fingerprint of the flux dependent ω_+ mode is left, see Fig. 5.18(b). This procedure ensures that influence of the ω_+ mode close to the switch setting condition is conserved. Then, in a second fitting step, the ω_+ mode is fitted. The starting parameters of the fitting procedure are essential to get good results.

The fitted data, depicted in Fig. 5.18, shows good agreement with the measured spectroscopy. In Figs. 5.18(d)-(f) exemplary fit results are presented for flux values where the fitting procedure is comparably difficult. Although the magnitude of one peak is one order higher than the lower one [Fig. 5.18(e)] or the bandwidths of the two Lorentzians are on the order of the frequency splitting [Fig. 5.18(d)], the fitted curves match the measurement data.

5.4.3 Analyzing the coupling constant $\mathbf{g}_{\mathrm{sw}}^{|\mathbf{g}\rangle}$

The fitted mode splitting $|\omega_+ - \omega_-|$ from Fig. 5.18(b) is used to calculate the coupling constant $g_{\mathrm{sw}}^{|g\rangle} = |\omega_+ - \omega_-|/2$, see Fig. 5.19(a). The dependence of the experimentally determined coupling strength on the applied flux follows the theoretical prediction as expected.

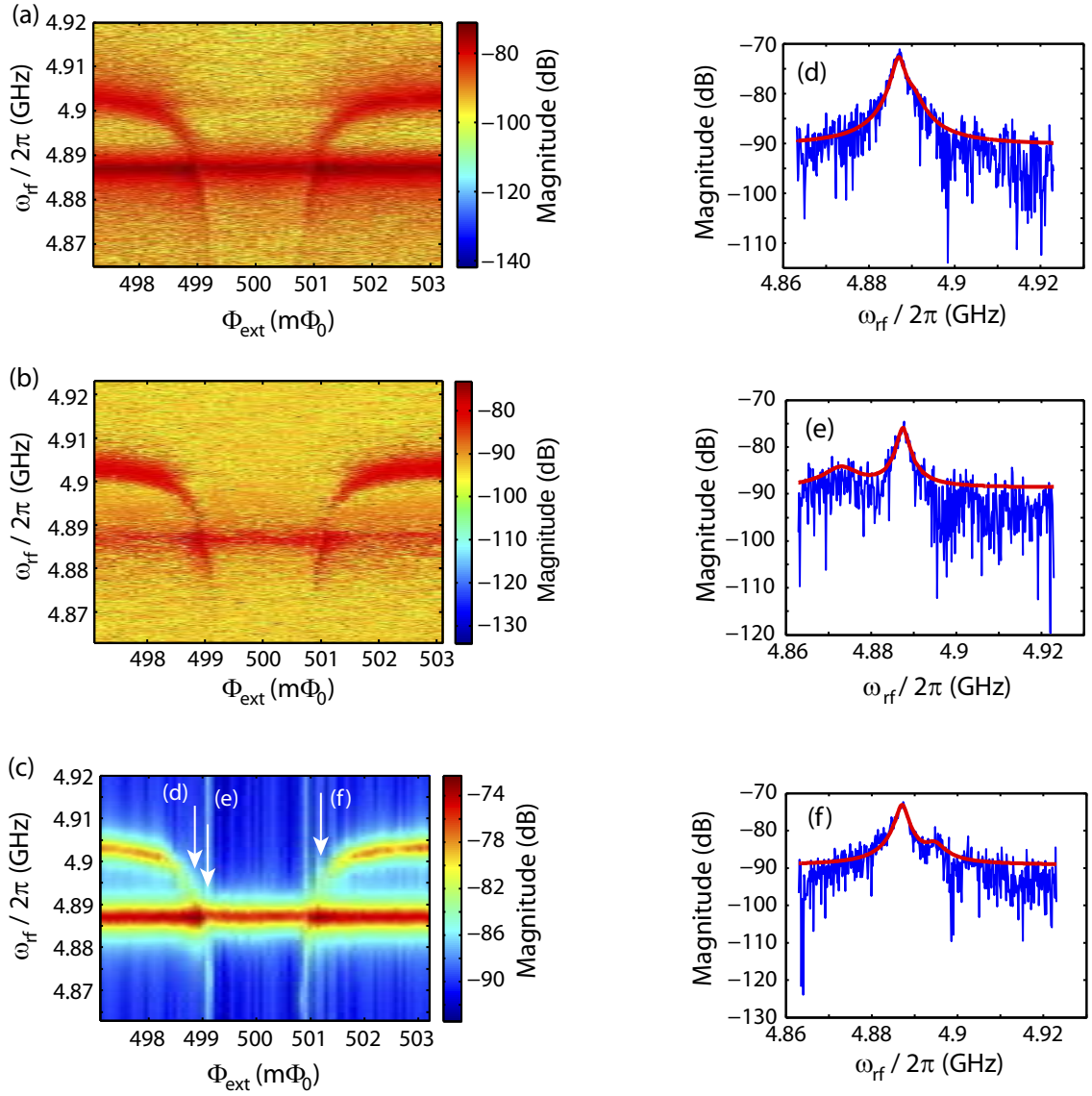

Figure 5.18: (a) Transmission spectroscopy measurement ($T = 50\,\mathrm{mK}$, $P_{\mathrm{rf}} = 136\,\mathrm{dBm}$) of the quantum switch in comparison to a data fit (c). Beside minor deviations the fitted spectrum matches the measured one. Close to the switch setting conditions, three flux points are chosen to compare the data with the fitted curve (d)-(f). (b) Modified measurement data, the averaged ω_- mode is subtracted from the original spectroscopy data shown in (a).

Theory predicts $g_{\mathrm{sw}} = 0$ at the switch setting condition. The data plotted in Fig. 5.19(b) shows that the two measurement points close to $498.9\,\mathrm{m}\Phi_0$ and $501.1\,\mathrm{m}\Phi_0$ are close to zero, to be accurate $(41.6 \pm 21.4)\,\mathrm{kHz}$ and $(166 \pm 20.0)\,\mathrm{kHz}$. The corresponding on-off-ratios $[10\log(g_{\mathrm{sw}}^{|g\rangle}/g_{\mathrm{AB}})]$ are $-23\,\mathrm{dB}$ and $-17\,\mathrm{dB}$, respectively. It is mainly limited by the measurement resolution, flux stability, and the fitting procedure. Nevertheless, the observed values are sufficient for practical applications.

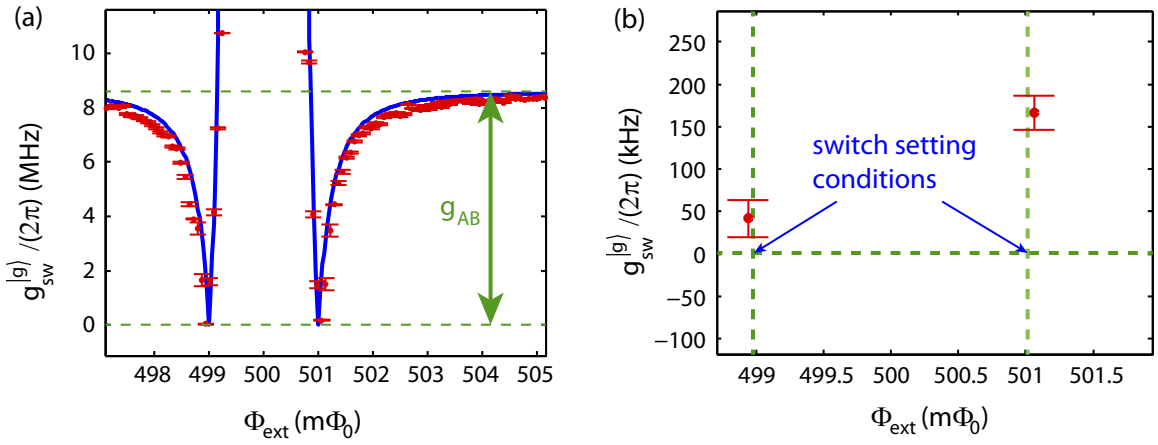

Figure 5.19: (a) $g_{\mathrm{sw}}^{|g\rangle}$ versus applied field. The frequency difference $g_{\mathrm{sw}}^{|g\rangle} = |\omega_+ - \omega_-|/2$ of the fitted Lorentzians (red dots) is in agreement with the simulations (blue line). Error bars are calculated from the statistical errors of ω_- and ω_+ using Gaussian error progressing. (b) Two measurements close to the switch setting condition show coupling strengths close to zero.

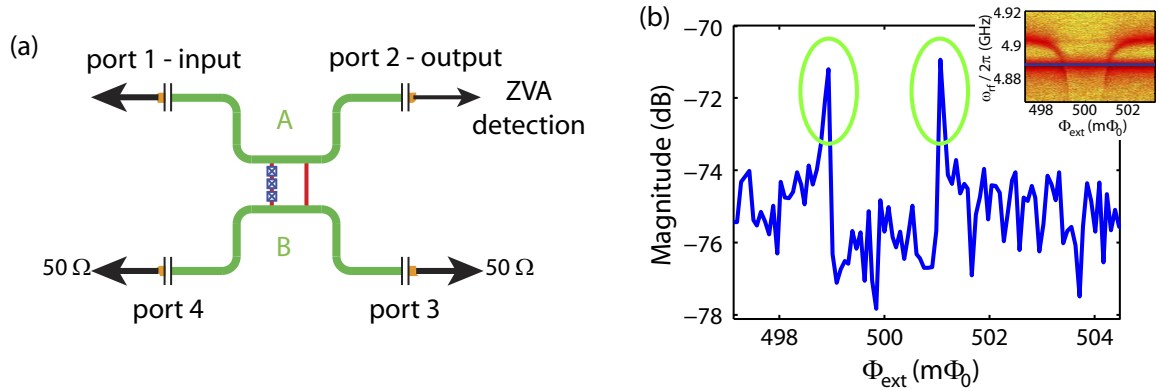

Figure 5.20: (a) Transmission measurement configuration. Port three and port four are not directly accessible. (b) Magnitude of the ω_- mode versus the external flux. Insert: Full transmission spectrum. The blue line indicates the cross section shown in the main graph.

5.4.4 Transmission at the switch setting condition

Despite the fact that for technical reasons, only the transmission through one of the resonators can be detected in the presented setup [see Fig. 5.20(a)], it is possible to analyze the beam splitting behavior of the quantum switch device. The latter expected to act as a near 50:50 beam splitter using input-and-output-formalism [100, 101] and the decay of the resonator wave function. More precisely, 51 % of the input signal at resonator A should be transmitted to resonator B and therefore port 1 and port 2 should emit 24.5 % and port 3 and port 4 should emit 25.5 % of the signal. A detailed calculation can be found in App. E.

Figure 5.20(b) depicts the flux dependent transmission at $\omega_- = 4.8872\,\mathrm{GHz}$. While the spectrum is almost constant for most flux values, the magnitude at $498.9\,\mathrm{m}\Phi_0$ and

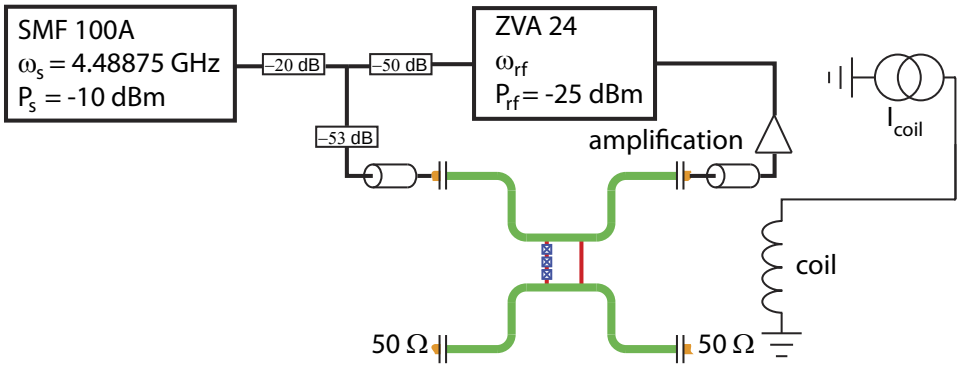

Figure 5.21: The investigation of $g_{\mathrm{sw}}^{\mathrm{mixed}}$ is performed with a transmission spectroscopy measurement. A second, high power signal using the SMF 100A is fed into the two-resonator sample at $\omega_{\mathrm{s}} = 4.8875\,\mathrm{GHz}$ and $P_{\mathrm{s}} = -10\,\mathrm{dBm}$ to excite the qubit into a dressed state.

$501.1\,\mathrm{m}\Phi_0$ is sharply increased by approximately 3.6 dB. Thus, slightly more than twice the power is transmitted through one resonator and not transferred to the second one. This increase in transmission is in good agreement with the value of 3.1 dB expected from the calculated splitting ratio. The small deviation is attributed to the not well-controlled reflection caused by the silver-glue-based connector-chip transitions at the sample box.

Later measurements, namely the second cooldown that has been used for the power calibration in subsection 5.3.3, provide access to both resonators. Indeed, in these measurements it is observed that at the switch setting condition the transmission to the other resonator is decreased.

In summary, the increased power transmission of 3.6 dB is a good indicator for the decoupling of the two resonators at the switch setting condition.

5.4.5 Switching the quantum switch by changing the qubit state

Here, the reader is reminded that the two resonators can also be decoupled at the switch setting condition by changing the qubit state from $|g\rangle$ to $|e\rangle$. To excite the qubit, a high power signal is inserted at $\omega_{\mathrm{s}} = 4.8875\,\mathrm{GHz}$ using the SMF signal source as sketched in Fig. 5.21. At this frequency, the signal is on resonance with the ω_--mode. The high power ($P_{\mathrm{s}} = -10\,\mathrm{dBm}$) creates approximate 10^3 photons inside the cavity which is sufficient to excite the qubit despite the detuned drive.

The outcome shown in Fig. 5.22(b), are two coupled resonators. Compared to the transmission shown in Fig. 5.22(a) where the qubit is in the ground state, the data in Fig. 5.22(b) indicates neither a crossing between the two modes nor a significant variation of ω_+. The cross sections of the spectra at the switch setting conditions are plotted in the lower panel. While Fig. 5.22(c) only shows one peak, Fig. 5.22(d) clearly exhibits a double peak spectrum.

The transmission behavior can be explained with the following model. The used excitation signal is not a π-pulse but a coherent continuous wave signal. Hence, the qubit is not excited into $|e\rangle$ but into a mixed state between $|g\rangle$ and $|e\rangle$, $p_{\mathrm{g}}|g\rangle\langle g| + p_{\mathrm{e}}|e\rangle\langle e|$. The resulting coupling constant is not $g_{\mathrm{sw}}^{|e\rangle}$ but $g_{\mathrm{sw}}^{\mathrm{mixed}}$. For a strong drive $p_{\mathrm{e}} = p_{\mathrm{g}} = 1/2$ for ground and excited state can be safely assumed. Considering the original Hamilto-

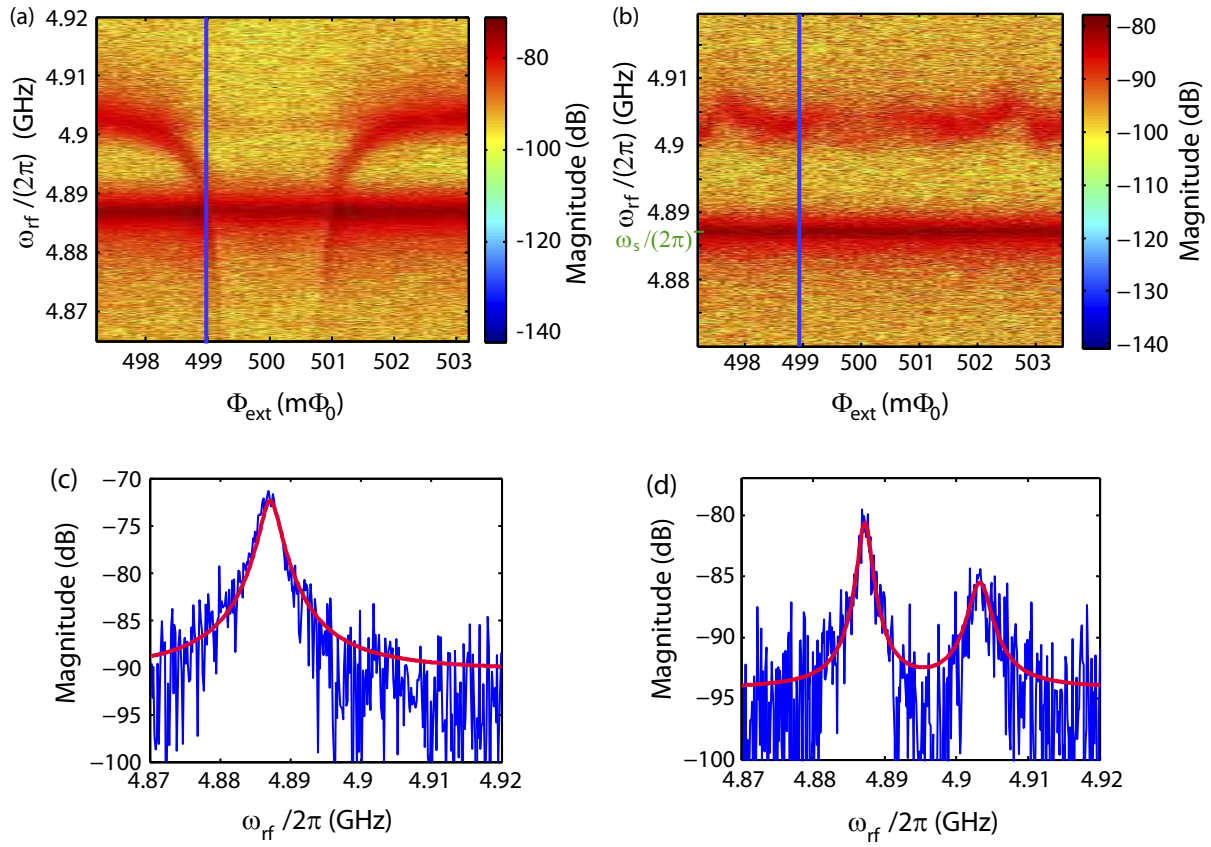

Figure 5.22: Transmission measurement of the quantum switch versus the applied magnetic flux for two different qubit states: (a) qubit in ground state, (b) qubit in mixed state. (c), (d) show the spectroscopy measurement at 498.93 mΦ_0, the exact position of the switch setting condition that in indicated by the blue lines in (a) and (b). (c) Only one peak is detectable, thus, the two resonators are decoupled. (d) the modes are clearly separated, thus, the two resonators are coupled.

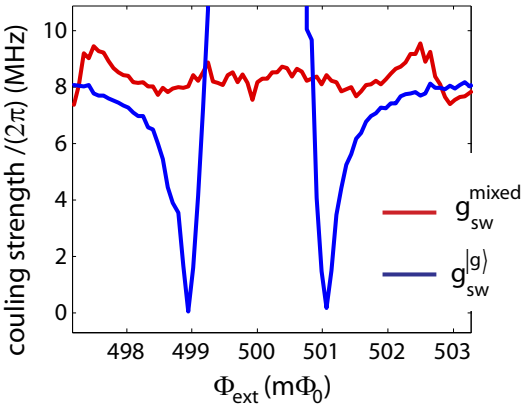

Figure 5.23: Comparison between $g_{\mathrm{sw}}^{|g\rangle}$ and $g_{\mathrm{sw}}^{\mathrm{mixed}}$. While $g_{\mathrm{sw}}^{|g\rangle}$ reduces to zero, $g_{\mathrm{sw}}^{\mathrm{mixed}}$ stays in the range of $7-9.5\,\mathrm{MHz}$. Both resonators are always coupled.

nian (3.6) of the quantum switch where the additional mode is neglected, the interaction between the two resonators in the dispersive limit is described by

$$\hat{H}_{\mathrm{int}}^{\mathrm{eff}} = \hbar\left(g_{\mathrm{AB}} + g_{\mathrm{dyn}}\hat{\sigma}_z\right)\left(\hat{a}^\dagger\hat{b} + \hat{a}\hat{b}^\dagger\right) + \hbar\hat{\sigma}_z g_{\mathrm{dyn}}\left(\hat{a}^\dagger\hat{a} + \hat{b}^\dagger\hat{b}\right)$$

see section 3.2.1. For the two qubit eigenstates $|g\rangle$ and $|e\rangle$ the expected transmission spectroscopy is that of the reduced Hamiltonians

$$\langle g|\hat{H}_{\mathrm{int}}^{\mathrm{eff}}|g\rangle = \hbar\left(g_{\mathrm{AB}} - g_{\mathrm{dyn}}\right)\left(\hat{a}^\dagger\hat{b} + \hat{a}\hat{b}^\dagger\right) - \hbar g_{\mathrm{dyn}}\left(\hat{a}^\dagger\hat{a} + \hat{b}^\dagger\hat{b}\right) = -\hbar g_{\mathrm{dyn}}\left(\hat{a}^\dagger\hat{a} + \hat{b}^\dagger\hat{b}\right)$$

and

$$\begin{aligned}\langle e|\hat{H}_{\mathrm{int}}^{\mathrm{eff}}|e\rangle &= \hbar\left(g_{\mathrm{AB}} + g_{\mathrm{dyn}}\right)\left(\hat{a}^\dagger\hat{b} + \hat{a}\hat{b}^\dagger\right) + \hbar g_{\mathrm{dyn}}\left(\hat{a}^\dagger\hat{a} + \hat{b}^\dagger\hat{b}\right)\\ &= 2\hbar g_{\mathrm{AB}}\left(\hat{a}^\dagger\hat{b} + \hat{a}\hat{b}^\dagger\right) + \hbar g_{\mathrm{dyn}}\left(\hat{a}^\dagger\hat{a} + \hat{b}^\dagger\hat{b}\right).\end{aligned}$$

Here, the brackets can be interpreted as tracing out the qubit degrees of freedom from $\hat{H}_{\mathrm{int}}^{\mathrm{eff}}$. For an incoherent classical mixture, the reduced Hamiltonian is

$$p_{\mathrm{g}}\langle g|\hat{H}_{\mathrm{int}}^{\mathrm{eff}}|g\rangle + p_{\mathrm{e}}\langle e|\hat{H}_{\mathrm{int}}^{\mathrm{eff}}|e\rangle = \hbar g_{\mathrm{AB}}\left(\hat{a}^\dagger\hat{b} + \hat{a}\hat{b}^\dagger\right).$$

The interaction strength in the dispersive limit is given by g_{AB} for all flux values (see Fig. 5.23)

The two resonators are always coupled. The small deviations of the ω_+-mode in the flux are found for flux values where the dispersive assumption for $\hat{H}_{\mathrm{int}}^{\mathrm{eff}}$ is violated.

Chapter 6

Summary and Outlook

The interaction between light and matter is one of the fundamental processes in physics. In the research field of cavity quantum electrodynamics (QED) this process is investigated by coupling single atoms to single photons that are trapped in three-dimensional optical cavities. An important prerequisite to investigate the coherent atom-photon interaction is that the coupling of the two systems is much larger than the photon loss rate of the cavity and the atom decay rate into modes other than the cavity mode. To this end, in the research field of circuit QED, the light matter interaction is studied using superconducting circuits, acting as two-level systems, so called qubits, and microwave resonators, acting as one-dimensional cavities. These systems provide various design parameters, and thus, various ways to couple the qubit to microwave resonators. During the last decade, the number subsystems interacting with each other and thus, the number if signal on a chip has increased. This trend asks for controlled directing of quantum signals between the different subsystems in the network. Consequently, a quantum switch is needed to take the part of a classical switch in classical networks. For this purpose, a quantum switch, consisting of two superconducting microwave resonators with equal eigenfrequencies ω_{R} and one flux qubit, is introduced within this work. Here, in the dispersive limit the qubit mediates a second-order coupling between the two resonators. Apart from the possibility of switching the coupling between the two resonators, the device itself can be used to create an entangled superposition state between the resonators. This is especially interesting as the qubit, working off-resonant, makes only minor contributions to the dephasing of the resulting states.

In this thesis a quantum switch is fabricated, measured and analyzed. The theoretical description of the device requires knowledge about the individual components which are shortly described in chapter 2. Here, two different designs of a flux qubit are introduced, a three-Josephson-junction flux qubit and a four-Josephson-junction one. Although the four-Josephson-junction qubit is not implemented into the quantum switch, dc-SQUID measurements indicate that the chosen design of the Josephson junctions allows for further applications using a four-Josephson-junction qubit.

A short overview about circuit QED helps to understand the complexity of the quantum switch and the later measurement scheme. The effective Hamiltonian of the system describes the individual components (qubit and two resonators), an ac-Zeeman shift of the cavity modes, and an interaction term between the two resonators mediated by a non-constant coupling strength $g_{\mathrm{AB}} + g_{\mathrm{dyn}}\sigma_z$. While g_{AB} is the constant geometric coupling between resonator A and resonator B, g_{dyn} denotes a qubit dependent and thus flux dependent quantity. Depending on the qubit state, the total coupling strength between the two resonators is the sum or the difference between the geometric and dynamic parts. At the switch setting condition, the external flux is tuned to fulfill $g_{\mathrm{AB}} = g_{\mathrm{dyn}}$

which results in a decoupled system for the qubit being in the ground state. To get a sufficiently strong coupling between the resonators and the qubit, which is required to compensate the geometric coupling, the qubit is galvanically contacted to the lines of the two resonators. The fabricated quantum switch works as expected.

Although the Hamiltonian of the system considers the individual components and their interaction terms, the measurements show that the fabricated quantum switch does not only consist of two resonator modes and a qubit. Due to the geometry, an additional mode, can be observed at frequency ω_a. This additional mode is identified as a current mode flowing through the qubit. The additional inductance due to the Josephson junctions leads to a reduced frequency ω_a compared to ω_R. As the current of this mode is flowing through the qubit, the coupling between the qubit and the additional mode is of ultra-strong nature ($g_\mathrm{a}/\omega_\mathrm{a} > 1$, the Hamiltonian describing the system cannot be simplified using a rotating-wave approximation). Consequently, higher "harmonics" of this additional mode behave non-harmonically ($\omega_{n\mathrm{a}} \neq n\omega_\mathrm{a}$) [81]. In summary, the Hamiltonian describing the system consists of the Hamiltonians of the individual components, the interaction terms between these components, and the Hamiltonian of the additional mode interacting with the qubit. A comparison at the switch setting condition between the original model withour and the new model including the additional modes shows a difference of g_dyn by a factor of two. Hence, the original model does not describe the galvanically coupled system quanitatively.

Despite the additional mode, the quantum switch modes show the expected properties as spectroscopy measurements indicate. At the switch setting condition, a mode-crossing of the degenerate two-resonator modes (quantum switch modes) and thus a decoupling of the two resonators is observable for the qubit being in the ground state. A detailed analysis of the transmission through one resonator shows how the coupling decreases when the applied flux approaches the switch setting condition. The measured coupling constant reaches values of $(41.6 \pm 21.4)\,\mathrm{kHz}$ and $(166 \pm 20.0)\,\mathrm{kHz}$ at the flux values close to the switch setting condition. These numbers are bound due to the measurement resolution and fitting inaccuracies as the fit of two Lorentzians separated by less than their width is not precise enough.

At the switch setting condition, the transmission through one of the resonators increases by more than a factor of two. This doubling of the transmitted signal and the existence of a mode crossing at the expected flux values are clear indications for a working quantum switch.

The coupling between the two resonators can be switched on and off by changing the qubit state at the switch setting condition. To this end, the qubit is excited into a mixed state using a high power cw-signal to populate the cavities with approximately 10^3 photons. As theory predicts, the coupling between the two resonators is non-zero independent of the applied flux. The two resonators remain coupled also at the switch setting condition. This measurement result shows the predicted difference of the coupling strengths depending on the qubit state.

The measured parameters of the qubit and the coupling constants between the individual components indicate that the switch setting condition and thus the decoupled resonator modes are in the dispersive limit with respect to the qubit transition frequency ω_Q. This is a good initial situation for further experiments with the quantum switch. Some ideas will be presented in the following.

A straight forward continuation is a transmission measurement using two ports as

input and two ports as output ports. Simultaneous measurements of the transmission on all output ports answers the question how the transmission through one resonator and the transmission from one to the other resonator behave with respect to the mediated coupling strength. First measurements using all four ports indicate a behavior following the expectations from theory. A π-pulse can be used to excite the qubit into the state $|e\rangle$. The ratio of the transmitted signals at the different ports for different qubit states is a fingerprint of the performance and the on-off ratio of the quantum switch.

Apart from spectroscopy measurements, entering the time domain is important. Rabi oscillations between the qubit and the coupled resonator mode ω_+ can be used to calculate the relaxation rate of the qubit. Although, the qubit relaxation and dephasing rates are not essential for a working quantum switch they are important quantities for other qubit applications at the Walther-Meissner-Institut. Efforts towards that direction are currently made and first results are expected soon.

After characterizing the individual components and the complete quantum switch, the next step is the application of the device for quantum experiments. Some examples of how the quantum switch architecture can be exploited to create nonclassical states or entanglement between the two resonators are pointed out in the following. Detailed explanations are presented in Ref. [43].

As the flux qubit of the quantum switch is placed in the center of the resonators to couple via the magnetic field a second qubit, e.g., a transmon [59], which couples via the electrical field to one of the resonators, e.g., resonator A, can be placed close to one of the coupling capacitors. This ancilla-qubit can be used to create a Fock state in the resonator [102]. Both resonators should be decoupled, meaning, the quantum switch qubit is in its ground state and the switch setting condition is fulfilled. The state $|1\rangle_\mathrm{A}$ stays in resonator A while cavity B remains is the vacuum state $|0\rangle_\mathrm{B}$. The quantum switch is now turned on, either by exciting the qubit or using an adiabatic shift. If the resonators are coupled for a time t the state evolves as

$$|\Psi\rangle = \cos(g_\mathrm{sw}^\mathrm{on} t)|1\rangle_\mathrm{A}|0\rangle_\mathrm{B} + \exp(i\pi/2)\sin(g_\mathrm{sw}^\mathrm{on} t)|0\rangle_\mathrm{A}|1\rangle_\mathrm{B}.$$

Depending on t the Fock state can be completely transferred from resonator A to resonator B ($t = \pi/(2g_\mathrm{sw}^\mathrm{on})$) or maximal entanglement between both cavities can be achieved ($t = \pi/(4g_\mathrm{sw}^\mathrm{on})$).

The quantum mechanical nature of the qubit is essential in the following idea. Resonator A is again prepared in Fock state $|1\rangle_\mathrm{A}$. The qubit is in the ground state $|g\rangle$ and the switch setting condition is fulfilled. Applying a $\pi/2$-pulse excites the qubit into a symmetric superposition state $(|g\rangle + |e\rangle)/\sqrt{2}$. As the time evolution of the Hamiltonian acts only on the excited state of the qubit, the state of the quantum switch evolves as

$$\frac{1}{\sqrt{2}}\left(|g\rangle|1\rangle_\mathrm{A}|0\rangle_\mathrm{B} + \cos(g_\mathrm{sw}^\mathrm{on} t)|e\rangle|1\rangle_\mathrm{A}|0\rangle_\mathrm{B} + \exp(i\pi/2)\sin(g_\mathrm{sw}^\mathrm{on} t)|e\rangle|0\rangle_\mathrm{A}|1\rangle_\mathrm{B}\right).$$

By waiting for time $t = \pi/(2g_\mathrm{sw}^\mathrm{on})$ the part $|e\rangle|1\rangle_\mathrm{A}|0\rangle_\mathrm{B}$ of the initial state is transferred to $|e\rangle|0\rangle_\mathrm{A}|1\rangle_\mathrm{B}$ and the result is

$$\frac{1}{\sqrt{2}}\left(|g\rangle|1\rangle_\mathrm{A}|0\rangle_\mathrm{B} + \exp(i\pi/2)|e\rangle|0\rangle_\mathrm{A}|1\rangle_\mathrm{B}\right).$$

This state represents maximal entanglement of three systems, here two Fock states and one qubit. The generation of tripartite entangled states is the precondition for the investigation of these states. As the two resonators are prepared in a Fock state configuration and thus, the resonators act as photonic qubits, additional qubits are not needed. As only one quantum switch qubit has to be fabricated, the system and the assumptions on the fabrication technology are eased dramatically. The same idea can be used to create entanglement between coherent states. Instead of preparing resonator A with a Fock state it is populated by a coherent state $|\alpha\rangle_{\mathrm{A}}$. The same principle as mentioned before results in the tripartite entangled state

$$\frac{1}{\sqrt{2}}\left(|g\rangle|\alpha\rangle_{\mathrm{A}}|0\rangle_{\mathrm{B}} + \exp(i\phi)|e\rangle|0\rangle_{\mathrm{A}}|\alpha\rangle_{\mathrm{B}}\right).$$

For a simple transformation of states between the two resonators the qubit is detuned from the cavities and decoherence of the qubit plays a minor role to the cavity states. Nevertheless, long relaxation and dephasing times are desired. Therefore, an implementation of a four-Josephson-junction qubit into further samples is recommended. The layout of such a qubit can be adapted from the design shown in subsection 4.1.3. The microwave spectroscopy data of such a four-Josephson-junction qubit, presented in section 4.3, indicates suitable performance.

Appendix A

Design Parameters of the Qubits

This section provides the exact layout parameters that were used to fabricate the four-Josephson-junction qubit shown in chapter 4.3 and the three-Josephson-junction qubit implemented in the quantum switch. The dose factor used in electron beam lithography within the GDS II file varies for the single components. For the three-Josephson-junction qubit implemented in the quantum switch, the internal dose factor of the bars is 1.2, the dose factor of the junction's nose, see Fig.A.1(d), is increased to 1.1 compared to the qubit line. The overall dose was $\approx 600\,\mu C/cm^2$. The dose of the resonator connection is reduced by 60 % to approximately $400\,\mu C/cm^2$. For the four-Josephson junction case, an internal dose adjustment was not necessary but the dose for the SQUID and qubit structure was with $500 - 600\,\mu C/cm^2$ a bit lower. In general these numbers differ for each fabricated sample.

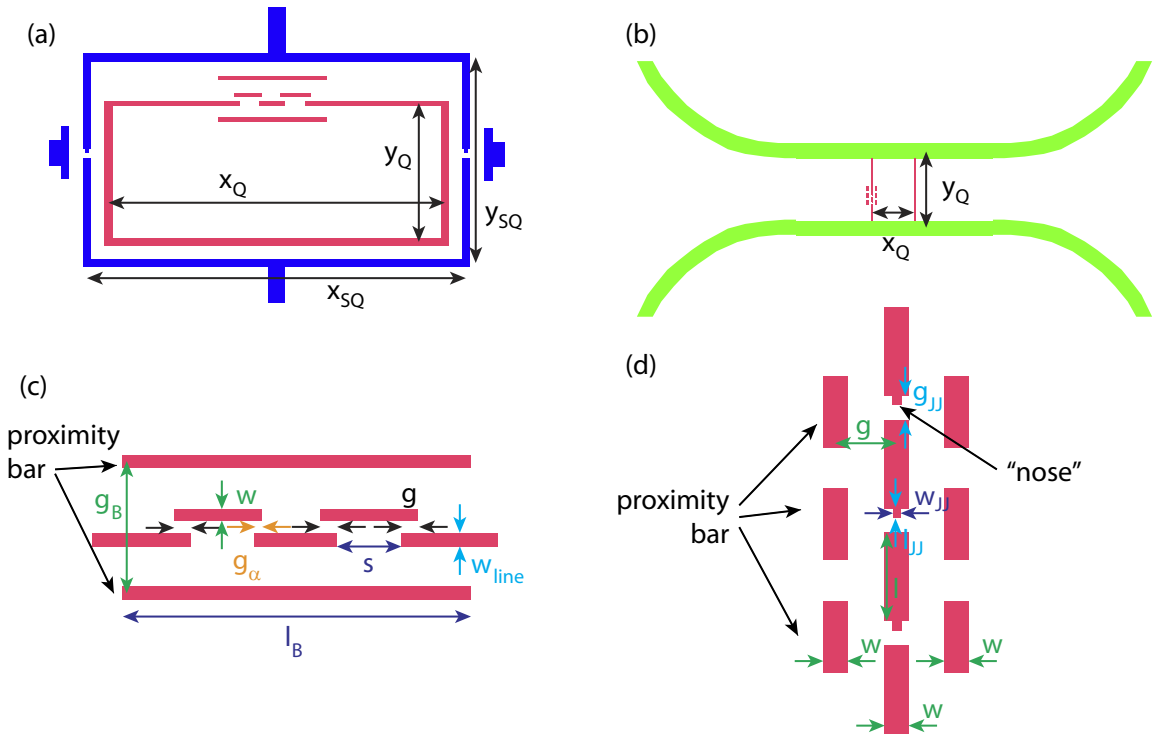

Figure A.1: GDS II layout used for the qubits (a) and (b) shows the overall layout. (c) and (d) depict details of the Josephson-junction layout.

three-Josephson-junction qubit		four-Josephson-junction qubit	
Parameter	Value (nm)	Parameter	Value (nm)
x_{Q}	20500	x_{Q}	20000
y_{Q}	8500	y_{Q}	30000
x_{sq}	23030		
y_{sq}	12500	$w_{\mathrm{JJ},\alpha}$	160
w	180	w_{JJ}	200
w_{line}	279	w	506
g	305	g_{JJ}	600
g_{α}	158	l_{JJ}	302
s	1190	g	2000
l_{B}	6600	l	2700
g_{B}	2520		

Table A.1: Layout parameters of the GDS II design of the three-Josephson-junction qubit (left) and the four-Josephson-junction qubit (right).

Appendix B

Fabrication Parameters

The following chapter gives information on the exact parameters for the fabrication of the different devices. Beginning with some general information (appendix B.1), the fabrication process of niobium resonators (appendix B.2), dc-bias lines (appendix B.3) and superconducting qubits (appendix B.4) are presented.

B.1 General information

One of the most critical steps which is always underestimated is the first cleaning of the blank substrate. Every bit of dust and dirt which sticks to the substrate during the first fabrication step is going to disturb the following process steps and may lead to an imperfect result. The cleaning procedure is as follows:

Process step	Parameters	Comments
First wafer cleaning	Acetone bath $t = 10\,\text{min}$ and $T = 70°$	Protection resist is removed.
	Acetone bath in ultrasonic, $t = 2\,\text{min}$, power 9	Before switching to the next bath, the wafer has to be splattered with fresh acetone
	Acetone bath in ultrasonic, $t = 2\,\text{min}$, power 9	Before switching to the next bath, the wafer has to be splattered with isopropanol
	Isopropanol bath in ultrasonic, $t = 2\,\text{min}$, power 9	The wafer should be flooded with fresh isopropanol before drying
	Dry with N_2	
General wafer cleaning	Acetone bath in ultrasonic, $t = 2\,\text{min}$	Before switching to the next bath, the wafer has to be splattered with fresh acetone
	Acetone bath in ultrasonic, $t = 2\,\text{min}$	Before switching to the next bath, the wafer has to be splattered with isopropanol
	Isopropanol bath in ultrasonic, $t = 2\,\text{min}$	The wafer should be flooded with fresh isopropanol before drying
	Dry with N_2	

B.2 Niobium resonators

The niobium resonators are fabricated using dc-magnetron sputtering and pattern transfer via a dry-etching technique. Thus, the niobium material is sputtered on an unstructured wafer and the layout is etched into the material using a SF_6 and Ar plasma. The following parameters were used for fabrication.

Process step	Parameters	Comments
Wafer cleaning	See appendix B.1	With power 9
Sputtering	Position of the sample holder in front of Nb-magnetron process pressure : $2.73 \cdot 10^{-3}$ mbar Ar flow: 10 sccm Power: 200 W Ramp: 5 s Pre-sputtering: $t = 5$ min	The pressure before the sputtering process is started should be less than $5 \cdot 10^{-9}$ mbar The actual sputtering time t has to be adjusted to the desired niobium thickness and to the actual sputtering ratio.
Wafer cleaning	See appendix B.1	With power 9
Spin coating	Resist: AZ 5214E $t = 55$ s at 8000 rpm	The wafer has to be placed onto the desired chuck. The vacuum ensures the stability during the coating. It is important to use a clean new pipette
Softbake	Wafer on hotplate: $t = 70$ s, $T = 110°$ C	
Edgewall removing	$t \approx 15 - 25$ s	For this exposure, a mask with a $150 - 200$ nm transparent border is designed. Thus, only the border is exposed and developed in the next step.
Developing	AZ 726 MIF developer from Microchemicals, $t = 30$ s H_2O basin, $t = 1$ min H_2O basin, $t = 1$ min	During development the basin should be moved. H_2O is a stopper concerning the AZ 726 MIF developer
Mask exposure	$t \approx 4 - 10$ s	The energy dose to obtain the exposure time is 36 mJ/cm^2 at 365 nm

To be continued on next page

Process step	Parameters	Comments
Development	AZ 726 MIF developer from Microchemicals, $t = 70 - 90\,\mathrm{s}$	During development, the basin should be moved.
	H_2O basin, $t = 1\,\mathrm{min}$	H_2O is a stopper concerning the AZ 726 MIF developer
	H_2O basin, $t = 1\,\mathrm{min}$	
Optical Check	The layout of the resonator has to be a one-to-one image of the layout on the mask. The gaps between the signal lines and the ground planes must be completely clean. The coupling capacitors and the alignment structures for later e-beam process must be well defined.	
RIE physical etching	O_2 flow: 0 sccm Ar flow: 10 sccm SF_6 flow: 20 sccm RF power: 100 W ICP power: 50 W He backing: 10 sccm Chamber pressure: 15 mTorr Strike pressure: 30 mTorr Ramp rate: 5 mTorr/s	
O_2 plasma ashing	O_2 flow: 50 sccm Ar flow: 0 sccm SF_6 flow: 0 sccm RF power: 100 W ICP power: 0 W He backing: 10 sccm Champer pressure: 5 mTorr Strike pressure: 50 mTorr Ramp rate: 5 mTorr/s	
Lift off	Acetone bath $T = 70°$ for up to one hour Acetone bath in ultrasonic, $t = 2\,\mathrm{min}$, power 2 Isopropanol bath in ultrasonic, $t = 2\,\mathrm{min}$, power 2 Dry with N_2	The sample should now be checked for any inaccuracies.

B.3 Dc-bias lines of gold

Like the niobium for the resonators, the gold is sputtered onto the wafer. In contrast to the dry-etching technique, a lift-off process requires a structured wafer before the sputtering step. The excessed material is removed in an acetone bath.

Process step	Parameters	Comments
Wafer cleaning	See appendix B.1	Use power 9
Spin coating	Resist: AZ 5214E $t = 1\,\text{min}$ at $4000\,\text{rpm}$	The wafer is placed centered onto the corresponding chuck. A new clean pipette is necessary to receive good results
Softbake	Wafer on hotplate: $t = 70\,\text{s}$, $T = 110^\circ\,\text{C}$	
Flood exposure	$t = 0.1 - 0.2\,\text{s}$	The wafer is exposed using UV-light without any photomask
Reversal bake	Wafer on hotplate: $t = 120\,\text{s}$, $T = 130^\circ\,\text{C}$	
Mask exposure	$t \approx 4 - 10\,\text{s}$	The energy dose to optain the exposure time is $36\,\text{mJ/cm}^2$ at $365\,\text{nm}$
Developing	AZ 726 MIF developer from Microchemicals, $t = 20 - 35\,\text{min}$	The status of the development process has to be checked approximately every 2 minutes after 20 min. With increasing time the status has to be checked more frequently.
	H_2O basin, $t = 1\,\text{min}$ H_2O basin, $t = 1\,\text{min}$	To stop the developing process

To be continued on next page

Process step	Parameters	Comments
Sputtering	Sputtering of $3 - 5\,\mathrm{nm}$ chromium: $I_{\mathrm{sp}} = 120\,\mathrm{mA}$, $t = 30\,\mathrm{s}$, $p_{\mathrm{Ar}} = 5 \cdot 10^{-2}\,\mathrm{mbar}$ Sputtering of $25\,\mathrm{nm}$ gold: $I_{\mathrm{sp}} = 15\,\mathrm{mA}$, $t = 135\,\mathrm{s}$, $p_{\mathrm{Ar}} = 5 \cdot 10^{-2}\,\mathrm{mbar}$	The chromium layer is necessary as an adhesive layer for the gold.
Lift off	Acetone bath $T = 70°$ for up to one hour Acetone bath in ultrasonic, $t = 2\,\mathrm{min}$, power 2 Isopropanol bath in ultrasonic, $t = 2\,\mathrm{min}$, power 2 Dry with N_2	If the gold has not vanished completely, the sample has to be placed into a new acetone basin; the lift off has to be repeated. After drying removing any left gold material gets hard. Therefore, it has to be checked that everything is removed as expected. The sample should now be checked for any inaccuracies.

B.4 Qubits

The fabrication of the qubits requires good control of each fabrication parameter. The shadow evaporation of the aluminum does not allow any etching technique. The excess aluminum is removed using a lift-off step where the lift-off time may easily exceed one hour. The following parameters were used to fabricate three- and four-Josephson junction qubits.

Process step	Parameters	Comments
Wafer cleaning	See appendix B.1	Using power 2
Spin coating	Resist: PMMA/MA 30 % $t = 2\,\text{min}$ at 2000 rpm	The wafer is placed centered onto the corresponding chuck. A new clean pipette is necessary to receive good results.
First baking	Wafer on hotplate: $t = 10\,\text{min}$, $T = 160°\,\text{C}$	The hotplate needs to be hot at the beginning of the baking process. In general, it should be started to heat at least 20 min before the spin coating step.
Spin coating	Resist: PMMA 950k $t = 2\,\text{min}$ at 4000 rpm	The wafer is placed centered onto the corresponding chuck. A new clean pipette is necessary to receive good results.
Second baking	Wafer on hotplate: $t = 10\,\text{min}$, $T = 160°\,\text{C}$	
Chip mounting	The sample has to be mounted onto the desired sample holder. The contact between the sample and the holder has to be as tight as possible to ensure good electrical conductivity. In the case of a $6 \times 10\,\text{mm}^2$ chip a special sticking pad was used to ensure this contact. The sample holder is placed into the vacuum chamber of e-beam writer which is then evacuated.	

To be continued on next page

Process step	Parameters	Comments
E-Beam exposure parameters	Aligning the sample using three desired points on the layout. The alignment includes x and y position as well as the working distance and the optical properties of the beam, such as gun tild and astigmatism. Gun voltage: 30 kV, pot size 1 Beam current: ≈ 27 pA	The beam current has to be checked every time before the writing process.
	Lead lines: 400 − 500 µC/cm^2 SQUID and Qubit: 500 − 600 µC/cm^2 Qubit with resonator line: $\approx$ 600 µC/cm^2 Resonator line: $\approx$ 400 µC/cm^2 Step size: 5.5 nm Area mode: meander Settling time: 0.1 ms	
Development	Developer: AllResist AR − P 600 − 56 $t = 2:20$ min Isopropanol basin, $t = 45$ s Isopropanol basin, $t = 45$ s	To stop the developing process
Optical check	An optical check after the e-beam writing and development is useful. Obvious errors can be seen with an optical microscope and the resist can be removed in an lift off. The wafer can be reused in a new run.	
Aluminum evaporation	First angle: ±16° p_{start}: $\approx 5 \cdot 10^{-9}$ mbar Beam current: $\approx$ 350 − 450 nA p_{process}: $\approx 2 \cdot 10^{-7}$ mbar Beam voltage : 8 kV Emission current: 380 - 450 mA Thickness: 40 nm	

To be continued on next page

Process step	Parameters	Comments
Oxidation	p_{process}: $2.0 \cdot 10^{-4}$ mbar $t = 21 - 26$ min	The time is the critical parameter during the oxidation step.
Aluminum evaporation	Second angle: $\mp 16°$ p_{start}: $\approx 5 \cdot 10^{-9}$ mbar Beam current: $\approx$ 350 − 450 nA p_{process}: $\approx 2 \cdot 10^{-7}$ mbar Beam voltage : 8 kV Emission current: 380 - 450 mA Thickness: 70 nm	
Lift off	Acetone bath $T = 70°$ for up to one hour Acetone bath in ultrasonic, $t = 2$ min, power 2 Isopropanol bath in ultrasonic, $t = 2$ min, power 2 Dry with N_2	If the aluminum has not vanished completely, the sample has to be placed into a new acetone basin and the lift off has to be repeated. After drying, it is not easy to remove any left material anymore. Therefore, it has to be checked that everything is removed as expected. The sample should now be checked concerning any inaccuracies.

Appendix C

Measurement Box

To perform the measurements the $6 \times 10\,\mathrm{mm}^2$ small silicon substrates are mounted into an appropriate measurement box. This box has to fulfill some requirements. First, the material must exhibit a good thermal and electrical conductivity at temperatures below 4 K. The chosen material oxygen-free high thermal conductivity (OFHC) copper has an electrical conductivity comparable to the conductivity of ordinary copper whereas the thermal conductivity is increased by a factor of 10 for temperatures below 2 K compared to standard copper. To avoid any surface oxidation, the boxes are galvanically covered with a thin gold layer. The second aspect considers the geometry of the box. Any box modes in the regime of less than 8 GHz should be avoided. The dimensions of the inner volume are therefore chosen to be as small as possible. The first measurement boxes (CPW and MS) have an inner volume of $11 \times 11 \times 3.25\,\mathrm{mm}^3$. Printed circuit boards (PCBs) are used to connect the V-connectors with the sample, see Fig. C.1.

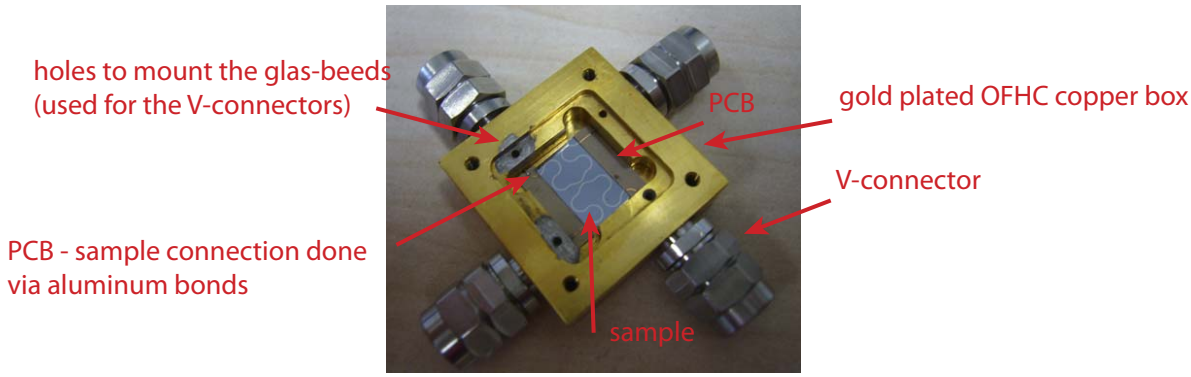

Figure C.1: MS measurement box with sample and PCBs.

Although the first box design was planned very well, the difficult connection between V-connector and PCB and between PCB and sample necessitated a new, simpler box. The second design (measurement box) has a smaller inner volume $10 \times 6 \times 5\,\mathrm{mm}^3$ and includes the usage of SMA-connectors. Their assembly is easier and less sensitive.

The CAD layouts of all three box designs are printed on the following pages.

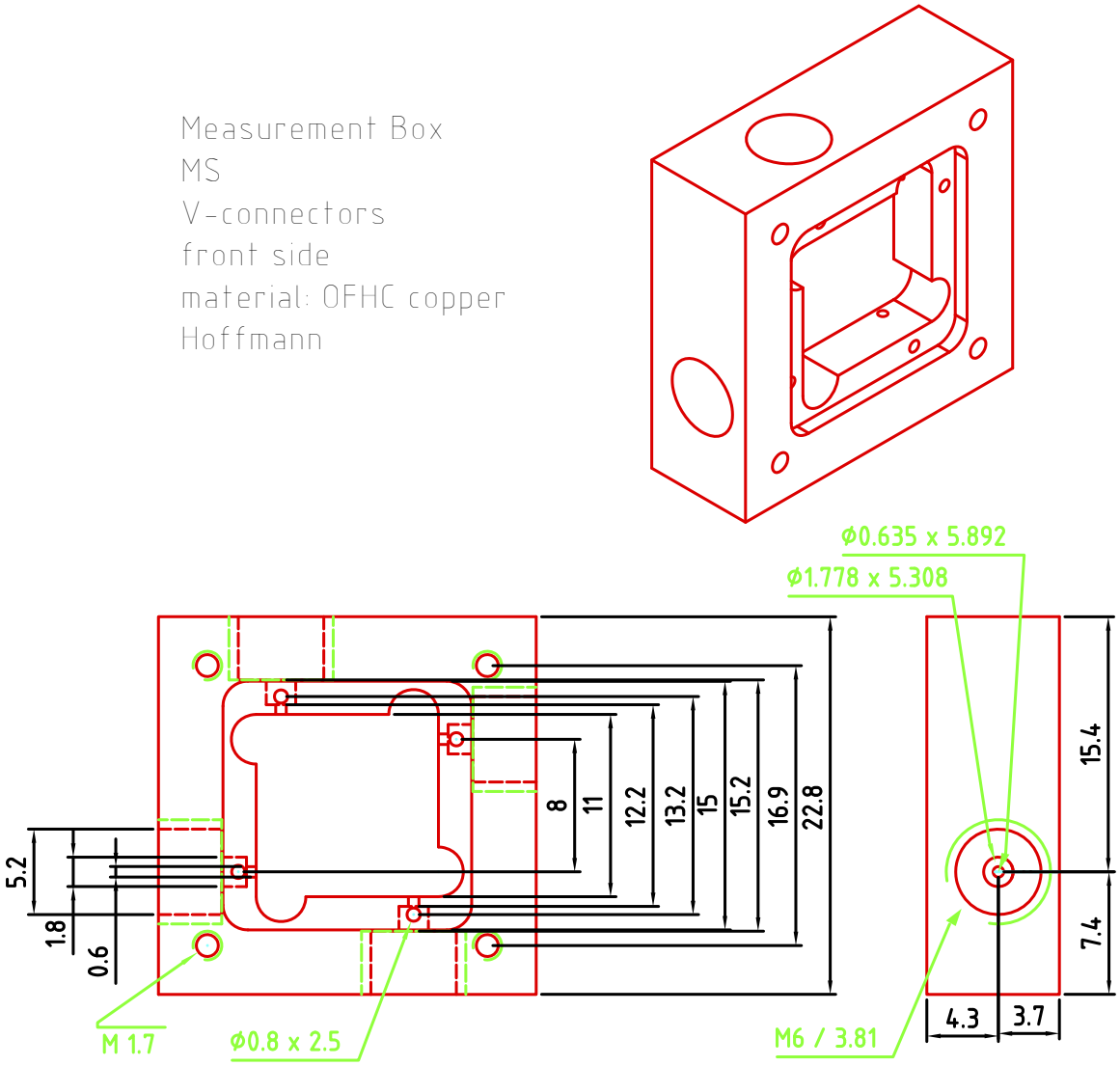

Figure C.2: CAD design of MS measurement box front side

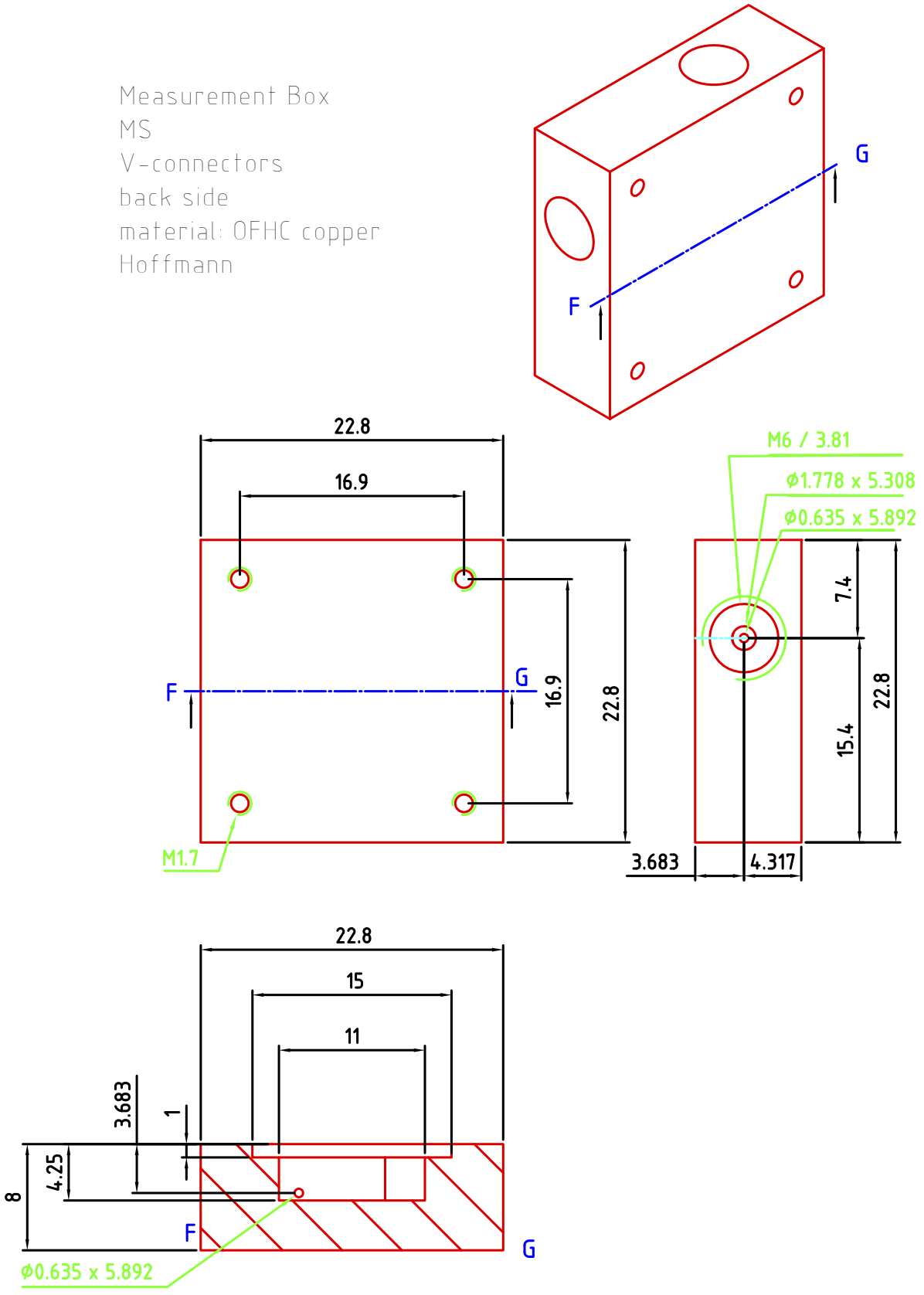

Figure C.3: CAD design of MS measurement box back side

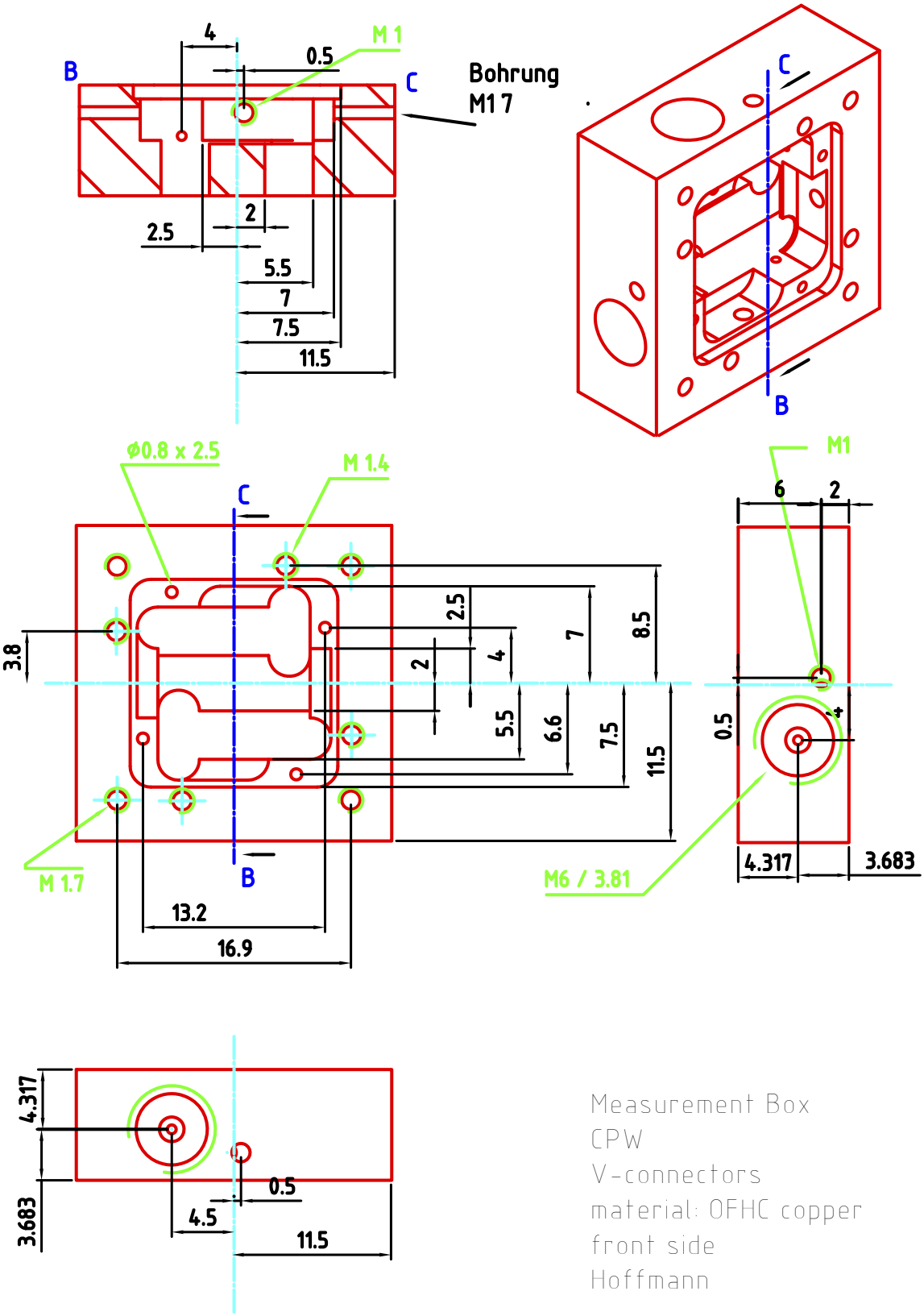

Figure C.4: CAD design of CPW measurement box front side

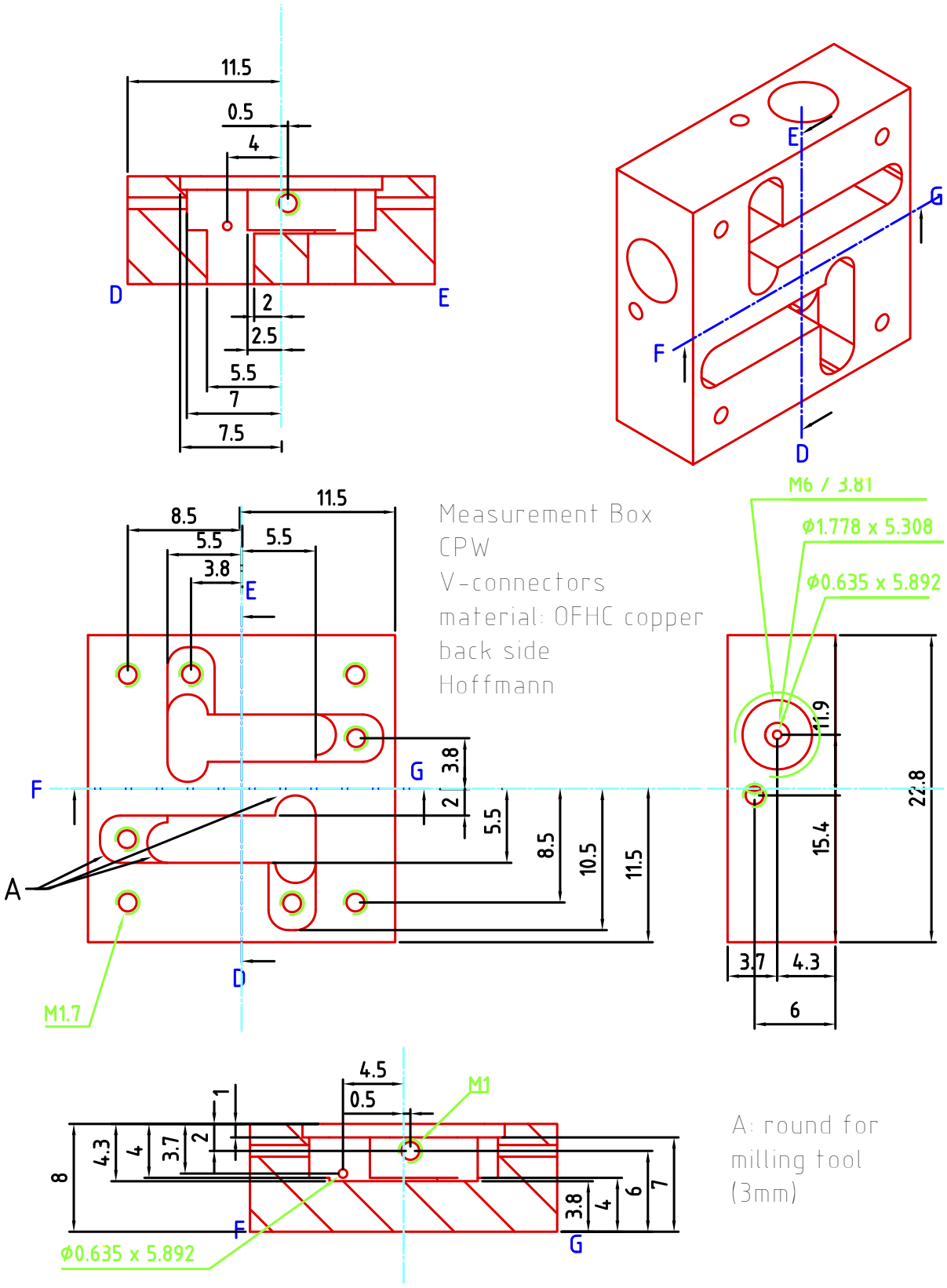

Figure C.5: CAD design of CPW measurement box back side

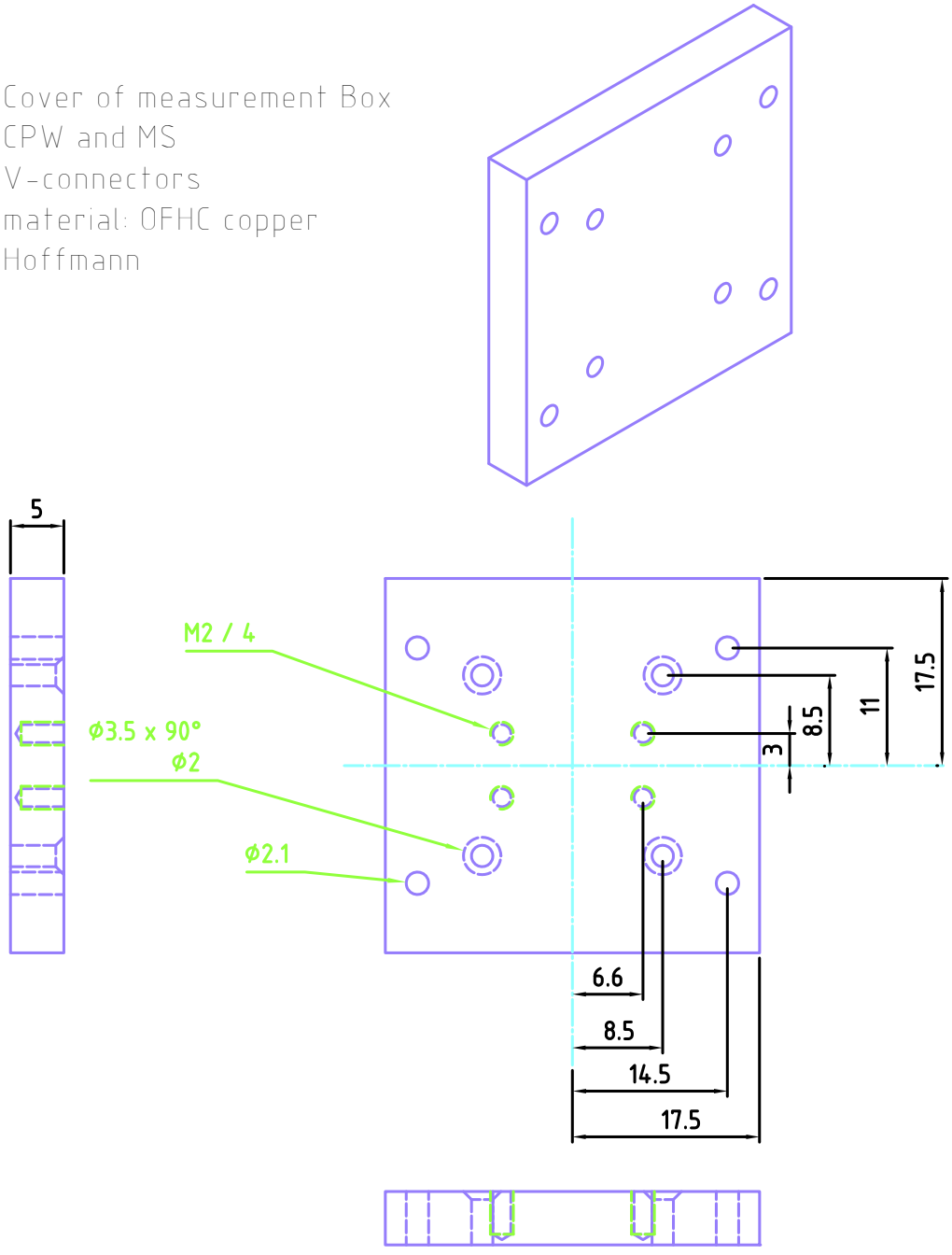

Figure C.6: CAD design of cover

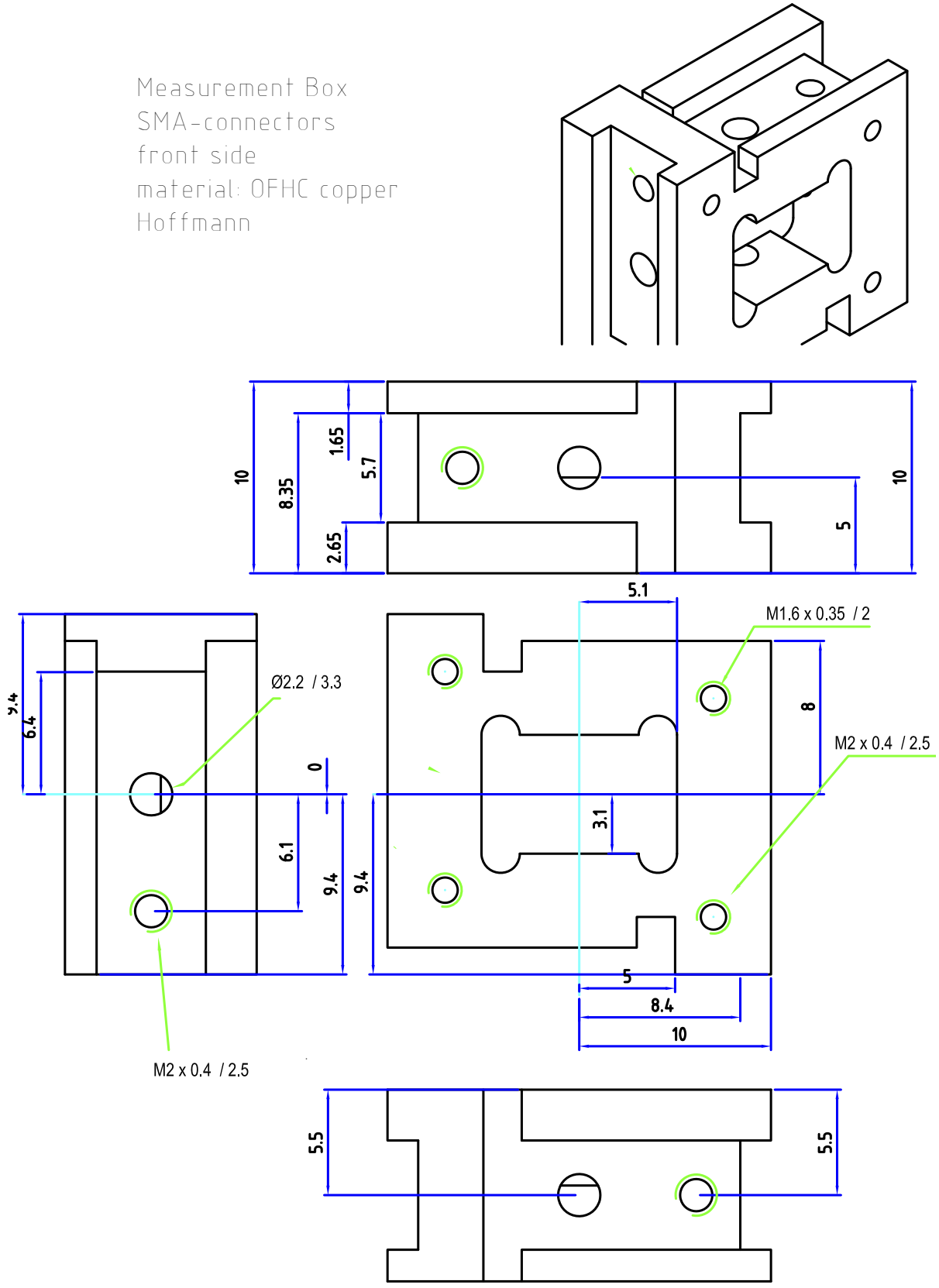

Figure C.7: CAD design of second measurement box

Appendix D

Setup of the 30 mK dilution unit

As mentioned in chapter 4.4, the used 30 mK setup was rebuilt during this work. In the following an overall scheme and the layouts of the components designed by the author are shown.

D.1 Complete Setup

The cryostat offers seven input channels which are all attenuated and thermalized at the required temperature stages, independently. Each of the four output channels implies at least two circulators at base temperature and at 700 mK and one cryogenic amplifier.

Figure D.1 depicts a sketch of the RF-cable connections inside the cryostat. The blue line represents the chain which was used to perform the presented measurements on the quantum switch sample.

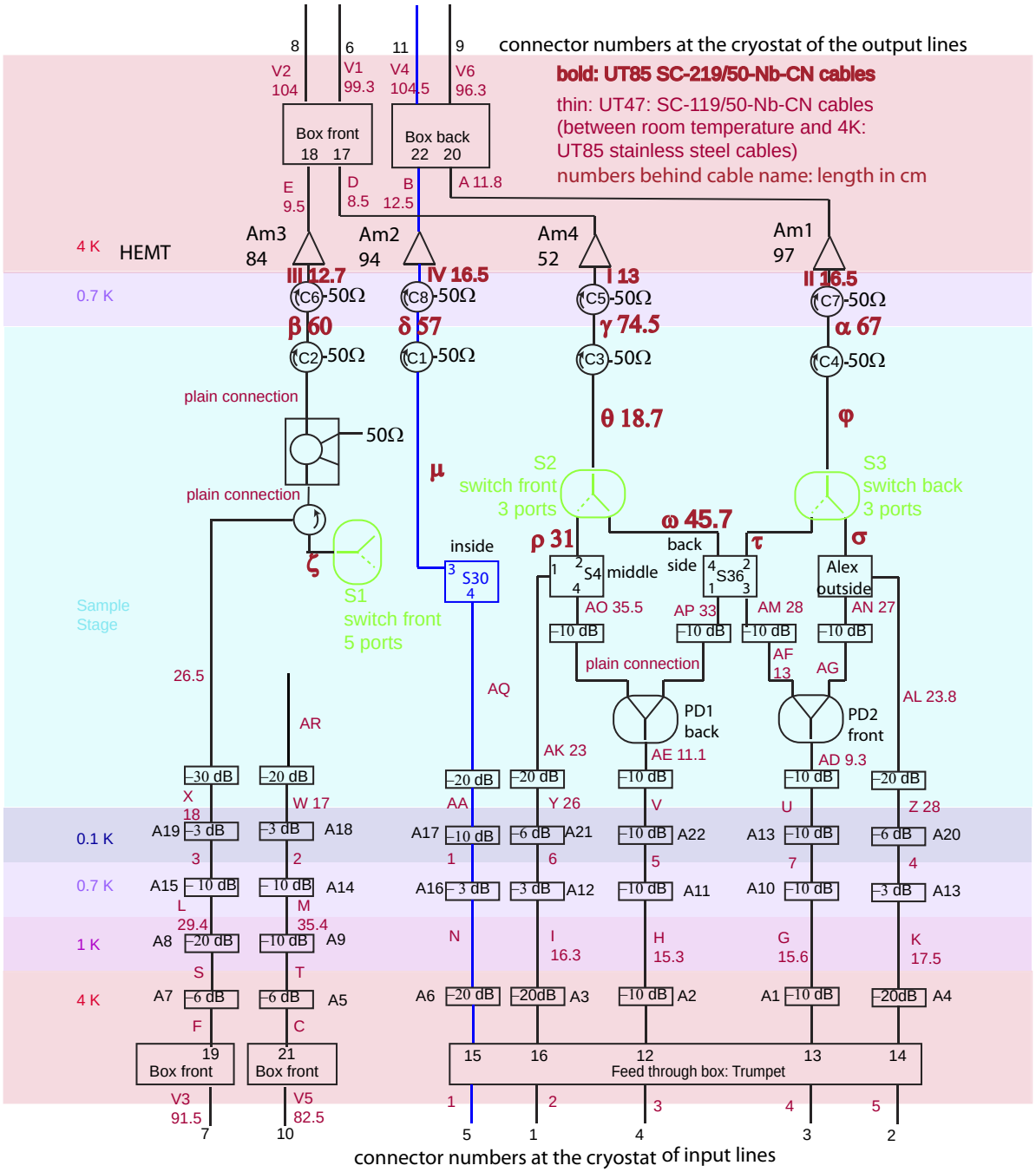

Figure D.1: Complete 30 mK setup. The blue line represents the chain used for the presented measurements.

D.2 dc-wiring

Apart from well defined RF-connections, thermal control and dc-drive of the used switches and amplifier is absolutely important. For this purpose, 96 dc-cables are implemented to transfer signals to the desired components. The complexity here lies in the channel which was used to implement the cables, namely the inner vacuum pumping line. Therefore, the connection box at room temperature and the used Lemo-connectors have to be vacuum tight and show a leaking rate of less than $1 \cdot 10^{-7}\,\mathrm{l} \cdot \mathrm{mbar/s}$ at the ^{4}He detection. As the box is fabricated using single components that are screwed and glued using silicone a smaller rate is not assumed. The individual components are not soldered as the option of re-soldering the Lemo-connectors is left open. The back side of the Lemo-connectors is shown in the close up in Fig. D.2.

As the cables are transferred from room temperature to 4 K a thermalization in between is obligatory. Therefore, the dc-cables are glued using GE varnish into small capillaries that are soldered into the copper baffels. The baffels are big enough to contact the inner wall of the vacuum tube. To ensure the quality of the pumping the baffels are only half-sided and always two of them are mounted to built a pair. They are made of copper to ensure a good thermal conductivity. The three lowerst baffels have to be a bit smaller, as the pumping line tube is bend in this region and reduced in radius.

The following figure presents an assembly overview of the single components and their CAD designs, respectively.

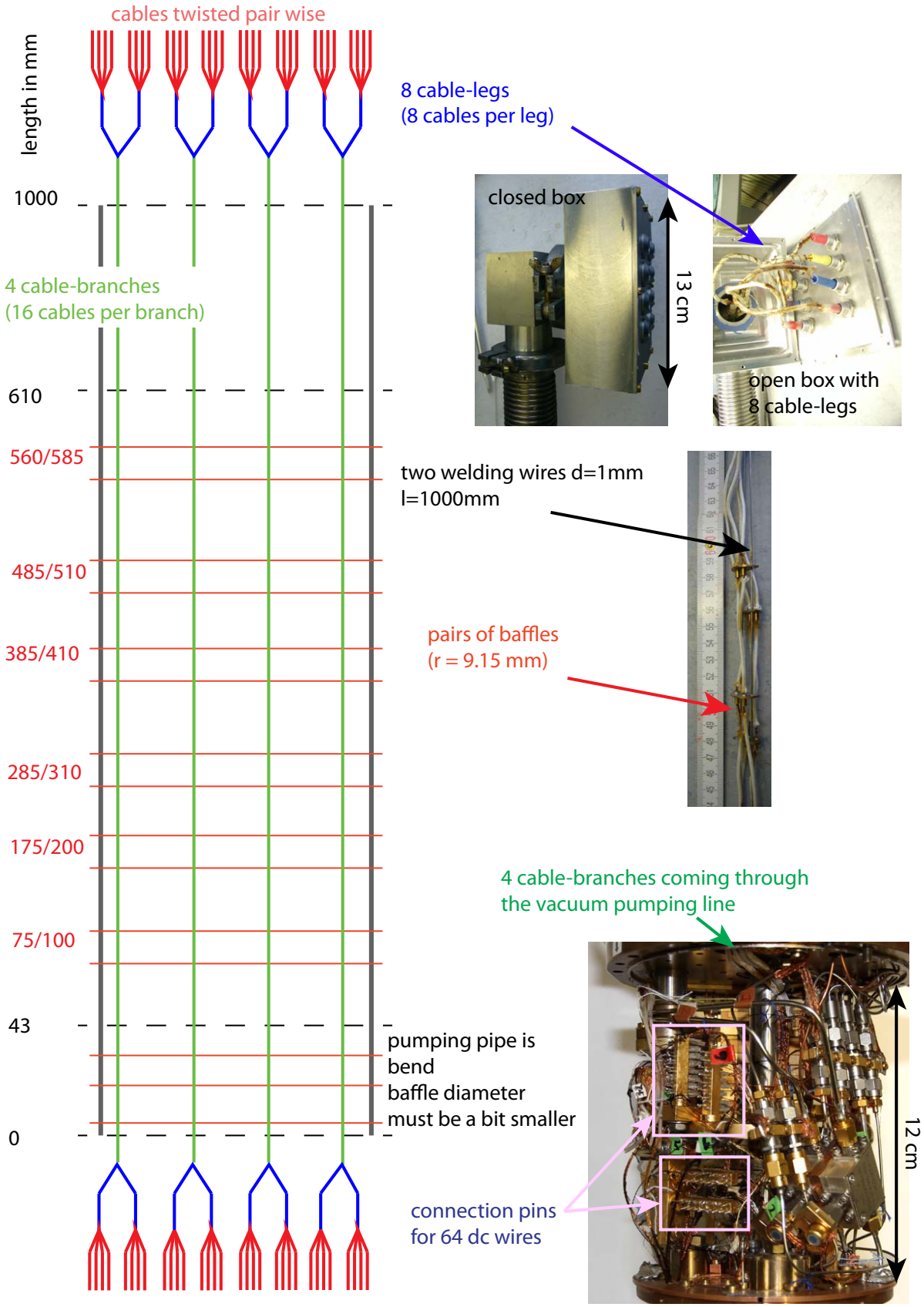

Figure D.2: Installation scheme of 96 dc-wires in the 30 mK cryostat

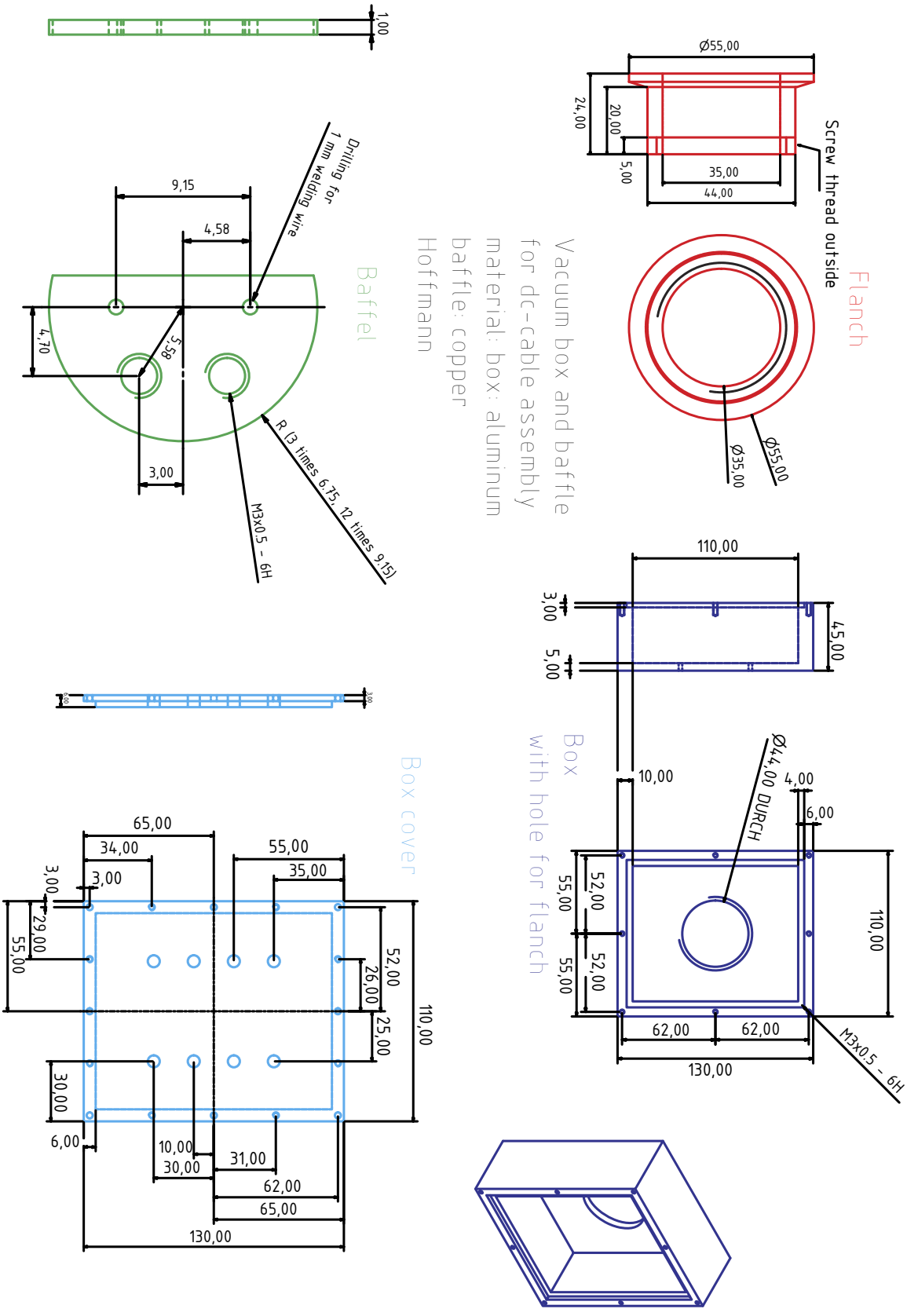
Vacuum box and baffle
for dc-cable assembly
material: box: aluminum
baffle: copper
Hoffmann
Baffel
Drilling for
1 mm wiedging wire
9,15
4,58
4,70
5,58
3,00
M3x0.5 - 6H
R (3 times 6.75, 12 times 9.15)
1,00
Box cover
65,00
34,00
3,00
55,00
35,00
29,00
55,00
52,00
26,00
25,00
110,00
30,00
6,00
10,00
30,00
31,00
62,00
65,00
130,00
Flanch
Ø55,00
24,00
20,00
5,00
35,00
44,00
Screw thread outside
Ø35,00
Ø55,00
Box
with hole for flanch
110,00
3,00
5,00
45,00
10,00
Ø4,00 DURCH
4,00
6,00
55,00
52,00
52,00
55,00
110,00
62,00
62,00
130,00
M3x0.5 - 6H

Appendix E

Estimation of the balance

In this chapter, the time evolution of the populated resonators is estimated analogously to Ref. [101]. In case of coupled resonators and neglecting any decay rates κ to the environment, the input-output relations for a time t are

$$\hat{a}_{\text{out}} = \hat{U}\hat{a}_{\text{in}}\hat{U}^{\dagger} \quad \text{and} \quad \hat{b}_{\text{out}} = \hat{U}\hat{b}_{\text{in}}\hat{U}^{\dagger}$$

with $\hat{U} = \exp[ig_{\text{AB}}t(\hat{a}^{\dagger}_{\text{in}}\hat{b}_{\text{in}} + \hat{a}_{\text{in}}\hat{b}^{\dagger}_{\text{in}})]$. This leads to

$$\hat{a}_{\text{out}}(t) = \cos(g_{\text{AB}}t)\hat{a}_{\text{in}} + i\sin(g_{\text{AB}}t)\hat{b}_{\text{in}}$$

and

$$\hat{b}_{\text{out}}(t) = \cos(g_{\text{AB}}t)\hat{b}_{\text{in}} + i\sin(g_{\text{AB}}t)\hat{a}_{\text{in}}.$$

Using only one input signal at resonator A at an input rate γ and the decay into the environment with $\exp(-\kappa t)$ the number of photons in the resonators reads

$$\langle \hat{a}^{\dagger}_{\text{out}}(t)\hat{a}_{\text{out}}(t)\rangle = \left(\gamma t\cos(g_{\text{AB}}t)e^{-\kappa t}\right)^2$$

and for resonator B

$$\langle \hat{b}^{\dagger}_{\text{out}}(t)\hat{b}_{\text{out}}(t)\rangle = \left(\gamma t\sin(g_{\text{AB}}t)e^{-\kappa t}\right)^2.$$

To calculate the balance between the two resonators, the integral over the hole time has to be normalized by the overall population. Thus, the balance is

$$\frac{\int_0^{\infty}\langle \hat{a}^{\dagger}_{\text{out}}(t)\hat{a}_{\text{out}}(t)\rangle\,\mathrm{d}t}{\int_0^{\infty}\langle \hat{a}^{\dagger}_{\text{out}}(t)\hat{a}_{\text{out}}(t)\rangle\,\mathrm{d}t + \int_0^{\infty}\langle \hat{b}^{\dagger}_{\text{out}}(t)\hat{b}_{\text{out}}(t)\rangle\,\mathrm{d}t} : \frac{\int_0^{\infty}\langle \hat{b}^{\dagger}_{\text{out}}(t)\hat{b}_{\text{out}}(t)\rangle\,\mathrm{d}t}{\int_0^{\infty}\langle \hat{a}^{\dagger}_{\text{out}}(t)\hat{a}_{\text{out}}(t)\rangle\,\mathrm{d}t + \int_0^{\infty}\langle \hat{b}^{\dagger}_{\text{out}}(t)\hat{b}_{\text{out}}(t)\rangle\,\mathrm{d}t}$$

With $g_{\text{AB}} = 8.5\,\text{MHz}$ and the mean value of $\kappa = 2.67\,\text{MHz}$, the balance is estimated to be $49 : 51$.

It is important to note that with decreasing decay rate κ, the two resonators becomes more and more a $50 : 50$ beam-splitter. As the decay rate of a single resonator cannot be measured in the presented setup, taking the mean value of κ_- and κ_+ gives only an upper limit on κ. Although the estimated unbalanced beam-splitter is a worst-case scenario, the quantum switch is comparably close to the ideal case.

List of publications

- E. Hoffmann, A. Baust, F. Deppe, D. Zueco, F. Quijandria, J. J. Garcia-Ripoll, M. Haeberlein, E. P. Menzel, E. Solano, A. Marx, and R. Gross, *Tunable Coupling Between Two Resonators Controlled by a Flux Qubit - The Quantum Switch*, in preparation for publication.

- M. Haeberlein, D. Zueco, P. Assum, T. Weißl, E. Hoffmann, B. Peropadre, J.J. Garcia-Ripoll, E. Solano, F. Deppe, A. Marx, and R. Gross, *Fast microwave beam splitters from superconducting resonators*, arXiv:1302.0729 submitted for publication (2013).

- E. P. Menzel, R. Di Candia, F. Deppe, P. Eder, L. Zhong, M. Ihmig, M. Haeberlein, A. Baust, E. Hoffmann, D. Ballester, K. Inomata, T. Yamamoto, Y. Nakamura, E. Solano, A. Marx, and R. Gross, *Path Entanglement of Continuous-Variable Quantum Microwaves*, Phys. Rev. Lett. **109**, 250502 (2012).

- T. Niemczyk, F. Deppe, E. P. Menzel, M. J. Schwarz, H. Huebl, F. Hocke, M. Haeberlein, M. Danner, E. Hoffmann, A. Baust, E. Solano, J. J. Garcia-Ripoll, A. Marx, and R. Gross, *Selection rules in a strongly coupled qubit-resonator system*, arXiv:1107.0810 (2011).

- E. Hoffmann, F. Deppe, T. Niemczyk, T. Wirth, E. P. Menzel, G. Wild, H. Huebl, M. Mariantoni, T. Weißl, A. Lukashenko, A. P. Zhuravel, A. V. Ustinov, A. Marx, and R. Gross, *A superconducting 180° hybrid ring coupler for circuit quantum electrodynamics*, Appl. Phys. Lett. **97**, 222508 (2010).

- M. Mariantoni, E. P. Menzel, F. Deppe, M. A. Araque Caballero, A. Baust, T. Niemczyk, E. Hoffmann, E. Solano, A. Marx, and R. Gross, *Planck Spectroscopy and Quantum Noise of Microwave Beam Splitters*, Phys. Rev. Lett. **105**, 133601 (2010).

- E. P. Menzel, F. Deppe, M. Mariantoni, M. A. Araque Caballero, A. Baust, T. Niemczyk, E. Hoffmann, A. Marx, E. Solano, and R. Gross, *Dual-Path State Reconstruction Scheme for Propagating Quantum Microwaves and Detector Noise Tomography*, Phys. Rev. Lett. **105**, 100401 (2010).

- G. M. Reuther, D. Zueco, F. Deppe, E. Hoffmann, E. P. Menzel, T. Weißl, M. Mariantoni, S. Kohler, A. Marx, E. Solano, R. Gross, and P. Hänggi, *Two-resonator circuit quantum electrodynamics: Dissipative theory*, Phys. Rev. B **81**, 144510 (2010).

- T. Niemczyk, F. Deppe, M. Mariantoni, E. P. Menzel, E. Hoffmann, G. Wild, L. Eggenstein, A. Marx, and R. Gross, *Fabrication technology of and symmetry*

breaking in superconducting quantum circuits, Supercond. Sci. Technol. **22**, 034009 (2009).

Bibliography

[1] P. Dirac, Proceedings of the Royal Society of London. Series A **114**, 243 (1927).

[2] A. L. Schawlow and C. H. Townes, Physical Review **112**, 1940 (1958).

[3] W. Zinth, A. Laubereau, and W. Kaiser, The European Physical Journal H (2011).

[4] D. Walls and G. Milburn, *Quantum optics* (Springer-Verlag, Berlin, 1994).

[5] C. W. Gardiner and P. Zoller, *Quantum noise* (Springer-Verlag, Berlin, 2004).

[6] R. Feynman, Int. J. Theor. Phys. **21**, 467 (1982).

[7] M. H. Levitt, Progress in Nuclear Magnetic Resonance Spectroscopy **18**, 61 (1986).

[8] D. Jaksch and P. Zoller, Annals of Physics **315**, 52 (2005).

[9] D. Jaksch, J. I. Cirac, P. Zoller, S. L. Rolston, R. Côté, and M. D. Lukin, Physical Review Letters **85**, 2208 (2000).

[10] D. Schrader, I. Dotsenko, M. Khudaverdyan, Y. Miroshnychenko, A. Rauschenbeutel, and D. Meschede, Physical Review Letters **93**, 150501 (2004).

[11] M. Anderlini, P. J. Lee, B. L. Brown, J. Sebby-Strabley, W. D. Phillips, and J. V. Porto, Nature **448**, 452 (2007).

[12] H. Weimer, M. Müller, I. Lesanovsky, P. Zoller, and H. P. Büchler, Nature Physics **6**, 382 (2010).

[13] T. Wilk, A. Gaëtan, C. Evellin, J. Wolters, Y. Miroshnychenko, P. Grangier, and A. Browaeys, Physical Review Letters **104**, 010502 (2010).

[14] G. P. Miroshnichenko and A. I. Trifanov, Quantum Information Processing **12**, 1417 (2013).

[15] Q. A. Turchette, C. S. Wood, B. E. King, C. J. Myatt, D. Leibfried, W. M. Itano, C. Monroe, and D. J. Wineland, Physical Review Letters **81**, 3631 (1998).

[16] S. Gulde, M. Riebe, G. P. T. Lancaster, C. Becher, J. Eschner, H. Häffner, F. Schmidt-Kaler, I. L. Chuang, and R. Blatt, Nature **421**, 48 (2003).

[17] H. Haffner, W. Hansel, C. F. Roos, J. Benhelm, D. Chek-al-kar, M. Chwalla, T. Korber, U. D. Rapol, M. Riebe, P. O. Schmidt, C. Becher, O. Guhne, W. Dur, and R. Blatt, Nature **438**, 643 (2005).

[18] D. L. Moehring, P. Maunz, S. Olmschenk, K. C. Younge, D. N. Matsukevich, L.-M. Duan, and C. Monroe, Nature **449**, 68 (2007).

[19] D. Hanneke, J. P. Home, J. D. Jost, J. M. Amini, D. Leibfried, and D. J. Wineland, Nature Physics **6**, 13 (2010).

[20] W. C. Campbell, J. Mizrahi, Q. Quraishi, C. Senko, D. Hayes, D. Hucul, D. N. Matsukevich, P. Maunz, and C. Monroe, Physical Review Letters **105**, 090502 (2010).

[21] D. J. Wineland, "Superposition, entanglement, and raising Schrödinger's cat," (2012), Nobel Lecture.

[22] R. G. Hulet, J. C. Bergquist, W. M. Itano, J. J. Bollinger, C. H. Manney, and D. J. Wineland, AIP Conference Proceedings **172**, 298 (1988).

[23] P. Goy, J. M. Raimond, M. Gross, and S. Haroche, Physical Review Letters **50**, 1903 (1983).

[24] J. M. Raimond, M. Brune, and S. Haroche, Reviews of Modern Physics **73**, 565 (2001).

[25] S. Haroche, "Controlling photons in a box and exploring the quantum to classical boundary," (2012), Nobel Lecture.

[26] G. Nogues, A. Rauschenbeutel, S. Osnaghi, M. Brune, J. M. Raimond, and S. Haroche, Nature **400**, 239 (1999).

[27] A. Blais, R.-S. Huang, A. Wallraff, S. M. Girvin, and R. J. Schoelkopf, Physical Review A **69** (2004), 10.1103/PhysRevA.69.062320.

[28] A. Wallraff, D. I. Schuster, A. Blais, L. Frunzio, R.-S. Huang, J. Majer, S. Kumar, S. M. Girvin, and R. J. Schoelkopf, Nature **431**, 162 (2004).

[29] A. Wallraff, D. I. Schuster, A. Blais, L. Frunzio, J. Majer, M. H. Devoret, S. M. Girvin, and R. J. Schoelkopf, Physical Review Letters **95**, 060501 (2005).

[30] D. I. Schuster, A. Wallraff, A. Blais, L. Frunzio, R.-S. Huang, J. Majer, S. M. Girvin, and R. J. Schoelkopf, Physical Review Letters **94**, 123602 (2005).

[31] O. Astafiev, K. Inomata, A. O. Niskanen, T. Yamamoto, Y. A. Pashkin, Y. Nakamura, and J. S. Tsai, Nature **449**, 588 (2007).

[32] F. Deppe, M. Mariantoni, E. P. Menzel, A. Marx, S. Saito, K. Kakuyanagi, H. Tanaka, T. Meno, K. Semba, H. Takayanagi, E. Solano, and R. Gross, Nature Physics **4**, 686 (2008).

[33] J. Abdumalikov, O. Astafiev, Y. Nakamura, Y. A. Pashkin, and J. Tsai, Physical Review B **78**, 180502 (2008).

[34] J. Majer, J. M. Chow, J. M. Gambetta, J. Koch, B. R. Johnson, J. A. Schreier, L. Frunzio, D. I. Schuster, A. A. Houck, A. Wallraff, A. Blais, M. H. Devoret, S. M. Girvin, and R. J. Schoelkopf, Nature **449**, 443 (2007).

[35] S. Filipp, M. Göppl, J. M. Fink, M. Baur, R. Bianchetti, L. Steffen, and A. Wallraff, Physical Review A **83**, 063827 (2011).

[36] M. A. Sillanpää, J. I. Park, and R. W. Simmonds, Nature **449**, 438 (2007).

[37] Y.-X. Liu, L. F. Wei, J. S. Tsai, and F. Nori, Physical Review Letters **96**, 067003 (2006).

[38] X.-L. He, J. Q. You, Y.-x. Liu, L. F. Wei, and F. Nori, Physical Review B **76**, 024517 (2007).

[39] M. Neeley, R. C. Bialczak, M. Lenander, E. Lucero, M. Mariantoni, A. D. O'Connell, D. Sank, H. Wang, M. Weides, J. Wenner, Y. Yin, T. Yamamoto, A. N. Cleland, and J. M. Martinis, Nature **467**, 570 (2010).

[40] M. Mariantoni, H. Wang, R. C. Bialczak, M. Lenander, E. Lucero, M. Neeley, A. D. O'Connell, D. Sank, M. Weides, J. Wenner, T. Yamamoto, Y. Yin, J. Zhao, J. M. Martinis, and A. N. Cleland, Nature Physics **7**, 287 (2011).

[41] M. Mariantoni, H. Wang, T. Yamamoto, M. Neeley, R. C. Bialczak, Y. Chen, M. Lenander, E. Lucero, A. D. O'Connell, D. Sank, M. Weides, J. Wenner, Y. Yin, J. Zhao, A. N. Korotkov, A. N. Cleland, and J. M. Martinis, Science **334**, 61 (2011).

[42] A. Dewes, F. R. Ong, V. Schmitt, R. Lauro, N. Boulant, P. Bertet, D. Vion, and D. Esteve, Physical Review Letters **108**, 057002 (2012).

[43] M. Mariantoni, F. Deppe, A. Marx, R. Gross, F. K. Wilhelm, and E. Solano, Physical Review B **78**, 104508 (2008).

[44] G. M. Reuther, D. Zueco, F. Deppe, E. Hoffmann, E. P. Menzel, T. Weissl, M. Mariantoni, S. Kohler, A. Marx, E. Solano, R. Gross, and P. Hänggi, Physical Review B **81**, 144510 (2010).

[45] D. M. Greenberger, M. A. Horne, A. Shimony, and A. Zeilinger, American Journal of Physics **58**, 1131 (1990).

[46] B. Josephson, Physics Letters **1**, 251 (1962).

[47] R. Gross and A. Marx, *Festkörperphysik* (Oldenbourg Wissenschaftsverlag GmbH, München, 2012).

[48] R. Doll and M. Näbauer, Physical Review Letters **7**, 51 (1961).

[49] B. Deaver and W. Fairbank, Physical Review Letters **7**, 43 (1961).

[50] J. Clarke and A. I. Braginski, *SQUID Handbook* (WILEY-VCH Verlag GmbH & Co. KGaA, Weinheim, 2004).

[51] R. C. Jaklevic, J. Lambe, A. H. Silver, and J. E. Mercereau, Physical Review Letters **12**, 159 (1964).

[52] M. Ketchen, IEEE Transactions on Magnetics **17**, 387 (1981).

[53] V. Ambegaokar and A. Baratoff, Physical Review Letters **10**, 486 (1963).

[54] W. C. Stewart, Applied Physics Letters **12**, 277 (1968).

[55] D. E. McCumber, Journal of Applied Physics **39**, 3113 (1968).

[56] Y. Nakamura, C. D. Chen, and J. S. Tsai, Physical Review Letters **79**, 2328 (1997).

[57] Y. Nakamura, Y. A. Pashkin, and J. S. Tsai, Nature **398**, 786 (1999).

[58] Y. Nakamura, Y. A. Pashkin, and J. S. Tsai, Physical Review Letters **87**, 246601 (2001).

[59] J. Koch, T. M. Yu, J. Gambetta, A. A. Houck, D. I. Schuster, J. Majer, A. Blais, M. H. Devoret, S. M. Girvin, and R. J. Schoelkopf, Physical Review A **76**, 042319 (2007).

[60] J. M. Fink, M. Göppl, M. Baur, R. Bianchetti, P. J. Leek, A. Blais, and A. Wallraff, Nature **454**, 315 (2008).

[61] J. A. Schreier, A. A. Houck, J. Koch, D. I. Schuster, B. R. Johnson, J. M. Chow, J. M. Gambetta, J. Majer, L. Frunzio, M. H. Devoret, S. M. Girvin, and R. J. Schoelkopf, Physical Review B **77**, 180502 (2008).

[62] T. P. Orlando, J. E. Mooij, L. Tian, C. H. van der Wal, L. S. Levitov, S. Lloyd, and J. J. Mazo, Physical Review B **60**, 15398 (1999).

[63] I. Chiorescu, Y. Nakamura, C. J. P. M. Harmans, and J. E. Mooij, Science **299**, 1869 (2003).

[64] J. M. Martinis, M. H. Devoret, and J. Clarke, Physical Review Letters **55**, 1543 (1985).

[65] J. Clarke, A. N. Cleland, M. H. Devoret, D. Esteve, and J. M. Martinis, Science **239**, 992 (1988).

[66] J. M. Martinis, S. Nam, J. Aumentado, and C. Urbina, Physical Review Letters **89**, 117901 (2002).

[67] J. M. Martinis and K. Osborne, cond-mat/0402415 (2004).

[68] J. Clarke and F. K. Wilhelm, Nature **453**, 1031 (2008).

[69] F. Yoshihara, K. Harrabi, A. O. Niskanen, Y. Nakamura, and J. S. Tsai, Physical Review Letters **97**, 167001 (2006).

[70] D. J. Van Harlingen, T. L. Robertson, B. L. T. Plourde, P. A. Reichardt, T. A. Crane, and J. Clarke, Physical Review B **70**, 064517 (2004).

[71] J. M. Martinis, K. B. Cooper, R. McDermott, M. Steffen, M. Ansmann, K. D. Osborn, K. Cicak, S. Oh, D. P. Pappas, R. W. Simmonds, and C. C. Yu, Physical Review Letters **95**, 210503 (2005).

[72] C. Cohen-Tannoudji, J. Dupont-Roc, and G. Grynberg, *Atom-photon interactions: basic processes and applications* (John Wiley & Sons, Inc., New York, 1992).

[73] M. Göppl, A. Fragner, M. Baur, R. Bianchetti, S. Filipp, J. M. Fink, P. J. Leek, G. Puebla, L. Steffen, and A. Wallraff, Journal of Applied Physics **104**, 113904 (2008).

[74] R. E. Collin, *Foundations for Microwave Engineering, Second Edition* (Wiley-IEEE Press, New Jersey, 2000).

[75] D. M. Pozar, *Microwave Engineering, Third Edition* (John Wiley & Sons, Inc., New York, 2005).

[76] R. N. Simons, *Coplanar Waveguide Circuits, Components, and Systems* (John Wiley & Sons, Inc., New York, 2001).

[77] J. J. Sakurai, *Modern Quantum Mechanics* (Addison-Wesley Publishing Company, Inc., New York, 1994).

[78] I. Awai, S. Iwamura, H. Kubo, and A. Sanada, Electronics and Communications in Japan (Part II: Electronics) **89**, 27 (2006).

[79] H. Toida, T. Nakajima, and S. Komiyama, Physical Review Letters **110**, 066802 (2013).

[80] E. Jaynes and F. Cummings, Proceedings of the IEEE **51**, 89 (1963).

[81] T. Niemczyk, *From strong to ultrastong coupling in circuit QED architectures* (Technische Universität München, 2011) ph.d. thesis.

[82] E. M. Purcell, H. C. Torrey, and R. V. Pound, Physical Review **69**, 37 (1946).

[83] A. Blais, R.-S. Huang, A. Wallraff, S. M. Girvin, and R. J. Schoelkopf, Physical Review A **69**, 062320 (2004).

[84] J. Gambetta, A. Blais, D. Schuster, A. Wallraff, L. Frunzio, J. Majer, M. Devoret, S. Girvin, and R. Schoelkopf, Physical Review A **74**, 042318 (2006).

[85] J. R. Schrieffer and P. A. Wolff, Physical Review **149**, 491 (1966).

[86] D. I. Schuster, A. A. Houck, J. A. Schreier, A. Wallraff, J. M. Gambetta, A. Blais, L. Frunzio, J. Majer, B. Johnson, M. H. Devoret, S. M. Girvin, and R. J. Schoelkopf, Nature **445**, 515 (2007).

[87] A. Fragner, M. Goppl, J. M. Fink, M. Baur, R. Bianchetti, P. J. Leek, A. Blais, and A. Wallraff, Science **322**, 1357 (2008).

[88] T. Weissl, *Two-Resonator Circuit-QED: Two Coupled Resonators on a Chip* (Technische Universität München, 2009) diploma thesis.

[89] L. Eggenstein, *Optimierung und Charakterisierung von supraleitenden Quantenschaltkreisen auf der Basis von Fluss-Qubits* (Technische Universität München, 2009) diploma thesis.

[90] F. Bilger, *Herstellung und Charakterisierung von Fluss-Quantenbits mit vier Josephson-Kontakten* (Technische Universität München, 2011) diploma thesis.

[91] T. Niemczyk, F. Deppe, M. Mariantoni, E. P. Menzel, E. Hoffmann, G. Wild, L. Eggenstein, A. Marx, and R. Gross, Superconductor Science and Technology **22**, 034009 (2009).

[92] J. Schuler, *Ferromagnetische Einzelladungs-Transistoren* (Technische Universität München, 2005) ph.d. thesis.

[93] M. Göppl, *Quantenelektronik mit supraleitenden Bauelementen - Herrstellung und Charakterisierung von Fluss-Qubits* (Technische Universität München, 2006) diploma thesis.

[94] T. Brenninger, *A new thin film deposition system for the preparation of persistent current qubits* (Munich University of Applied Sciences, 2007) master thesis.

[95] H. A. Haus, *Waves and Fields in Optoelectronics* (CBLS, New Delhi, 2004).

[96] H. Kamerlingh Onnes, Comm. Phys. Lab. Univ. **124c** (1911).

[97] M. Wallquist, V. S. Shumeiko, and G. Wendin, Physical Review B **74**, 224506 (2006).

[98] M. Sandberg, C. M. Wilson, F. Persson, T. Bauch, G. Johansson, V. Shumeiko, T. Duty, and P. Delsing, Applied Physics Letters **92**, 203501 (2008).

[99] J. Bourassa, J. M. Gambetta, J. Abdumalikov, O. Astafiev, Y. Nakamura, and A. Blais, Physical Review A **80**, 032109 (2009).

[100] C. W. Gardiner and M. J. Collett, Physical Review A **31**, 3761 (1985).

[101] L. Chirolli, G. Burkard, S. Kumar, and D. P. DiVincenzo, Physical Review Letters **104**, 230502 (2010).

[102] A. A. Houck, D. I. Schuster, J. M. Gambetta, J. A. Schreier, B. R. Johnson, J. M. Chow, L. Frunzio, J. Majer, M. H. Devoret, S. M. Girvin, and R. J. Schoelkopf, Nature **449**, 328 (2007).

Danksagung

Wie immer bei großen Arbeiten, ist auch diese Arbeit nicht ohne unterstützende Hilfe entstanden. Ich möchte daher hier die Möglichkeit ergreifen, mich bei allen beteiligten Personen zu bedanken.

Ein ganz herzliches Danke geht an meinen Doktorvater und Betreuer Herrn Prof. Dr. Rudolf Gross. Es war immer wieder hilfreich, auf seinen Erfahrungsschatz zurückgreifen zu können, wenn es eben doch mal nicht so klappte wie gedacht. Wie wertvoll das sein kann, wurde vor allem in der letzten Phase der Arbeit deutlich. Abgesehen von der direkten Betreuung ist jedoch ein zweiter Aspekt nicht zu vernachlässigen, der uns WMIlern erst im Vergleich mit anderen Gruppen auffällt. Ich möchte mich für eine hervorragende finanzielle Absicherung (Stichwort SFB) bedanken, die einerseits eine gut fundierte Wissenschaft ermöglicht, die natürlich aber auch das Privatleben planbar macht. Die dadurch geförderte gute Atmosphäre am WMI hat ihren Beitrag zum Gelingen dieser Arbeit geleistet.

Jedoch hilft die beste Atmosphäre nichts, gäbe es da nicht die direkte Betreuung durch die Projektleiter. Dr. Achim Marx und Dr. Frank Deppe möchte ich für die intensive und gute Betreuung meiner Tätigkeit danken.

Dadurch, dass Frank bei der theoretischen Entwicklung des Quantum Switches direkt beteiligt war, waren Diskussionen hinsichtlich der theoretischen Beschreibung und experimentellen Messverfahren sehr aufschlussreich. Des Weiteren möchte ich mich insbesondere dafür bedanken, dass er mir auch abseits der Physik, besonders in schwierigen Situationen, den Rücken gestärkt hat.

Achim möchte ich neben der fachlichen Hilfe vor allem für die Unterstützung im Laboralltag danken. Es war gut bei größeren Projekten, sei es der Umbau des Kryos oder eine Umstrukturierung der Laborarbeit, auf seine Hilfe zählen zu können.

An dieser Stelle möchte ich mich insbesondere bei meinen Betreuern, Herrn Gross, Herrn Marx und Herrn Deppe für die intensive Korrektur der hier vorliegenden schriftlichen Arbeit bedanken.

Obwohl Dr. Hans Hübl kein offizieller Betreuer meiner Arbeit war, geht ein herzlicher Dank für die zahlreichen helfenden Ratschläge über Herstellungsverfahren und mögliche Messungen an ihn. Sein fachliches Wissen hat mir immer wieder weitergeholfen (und wenn nicht das Wissen direkt, dann doch zumindest der Tipp wo was zu finden ist). Es war zudem eine Freude und wertvolle Erfahrung zusammen mit Hans und Alex den Doktoranden-Workshop in der Wildschönau 2012 zu organisieren.

Bei Alexander Baust möchte ich mich für zwei sehr nette Jahre im Labor bedanken. Es war eine Freude mit ihm zusammenzuarbeiten und über Physikalisches und Weltliches zu diskutieren. Ich hoffe, dass mein Quantum Switch auch bei ihm zu einem Erfolg führt.

Dem schließt sich direkt mein Dank an Max Häberlein für die Organisation des Kryo-Umbaus an. Zumal es immer wieder hilfreich war, seine Sichtweise der Theorie oder des Systems gemeinsam zu erörtern und dadurch systematische Herangehensfehler auszuschließen. Für Material-Diskussionen und Hilfestellungen beim Umbau möchte ich mich bei Dr. Karl

Neumaier, Dr. Christian Probst und Dr. Kurt Ulig bedanken. Es war sehr wertvoll auf ihren Erfahrungsschatz zurückgreifen zu können.

Tomasz Niemczyk und Edwin Menzel möchte ich für die Einarbeitung im Labor und an den technische Geräten danken. Tomasz, der mich schon während meiner Diplomzeit am WMI betreute, führte mich zu Anfang in die Labore, die Herstellungs- und Messtechnik der Qubits ein und ermöglichte mir somit einen gelungenen Start in die Doktorarbeit.

Quisiera expresar mi especial agradecimiento al Dr. David Zueco, al Fernando Quijandria, al Dr. Juan-Jose García-Ripoll y al Prof. Dr. Enrique Solano por el apoyo y la ayuda que me han prestado durante años con relación a la teoría y a la interpretación de los resultados de los ensayos.

Abgesehen von wissenschaftlicher Hilfestellung kommt eine solche Arbeit nicht Zustande ohne technisches Knowhow. Hier möchte ich mich vor allem bei Thomas Brenninger bedanken, der die technischen Groß-Geräte, die für die Herstellung benötigt wurden, nicht nur wartet, sondern pflegt. Für die unermessliche Ruhe und Geduld auf der einen Seite und die ständige Unterstützung andererseits möchte ich mich ganz herzlich bedanken.

Abgesehen von zahlreichen Doktoranden, möchte ich mich natürlich auch bei all denjenigen bedanken, die mir im Rahmen von Diplomarbeiten und Werkstudententätigkeiten "zugearbeitet" haben. Das wären Thomas Weissl (Diplomarbeit 2009), Felix Bilger (Diplomarbeit 2011), Maurice Hermwille (Werkstudent 2009), Marta Krawczyk (Werkstudentin 2010) und Norbert Kalb (Werkstudent 2012). Ohne ihre Fragen hätte ich mir über so manches möglicherweise weniger Gedanken gemacht und ohne fremde Hilfe hätte vieles länger gedauert. Auch möchte ich mich an dieser Stelle bei Namvar Jahanmehr bedanken, der mir vor allem in der "heißen Phase" der Qubit-Optimierung helfend zur Seite stand und viele der unzähligen Proben herstellte, die ich für die Layout- und Dosistests benötigte.

Für eine gute Zusammenarbeit möchte ich mich bei den aktuellen und ehemaligen Doktoranden/innen der Qubit Gruppe bedanken, insbesondere bei Peter Eder, Jan Goetz, Fredrik Hocke, Karl Friedrich Wulschner und Ling Zhong. Abseits der Qubitgruppe möchte ich mich vor allem bei Matthias Althammer, Franz Czeschka, Johannes Büttner, Bernhard Muschler, Toni Helm, Dr. Matthias Opel und Mathias Weiler für die gute interdisziplinäre Zusammenarbeit (Stichwort Laborbesprechung, Freitagsbier) bedanken. Zurückkommend auf das gute Arbeitsklima, möchte ich mich an dieser Stelle meine Büro-Nachbarn erwähnen und bedanke mich bei Johannes Büttner, Florian Palitschka, Friedrich Wulschner, Sybille Meyer für eine gelockerte Büro- und Arbeitsatmosphäre.

Eine noch so gut hergestellte Probe bringt wenig, wenn diese nicht vermessen werden kann. Ein ganz großes Dankeschön geht daher an die Werkstatt des WMIs, an Helmut Thies, Robert Müller, Christian Reichlmeier (der all meine Probenboxen herstellte), Julius Klaus und Georg Nietschke für die viele hilfreichen Tipps und Verbesserungsvorschläge bei technischen Fragestellungen und für eine hervorragende Zusammenarbeit beim Umbau des Kryostaten.

Ein Dank der besonderen Art geht an Katrin Nobbe, die einerseits nicht die Mühe scheute die vorliegende Arbeit zu lesen, mich andererseits immer wieder an einer Welt teilhaben lässt, die ich so noch nicht kenne. Zudem möchte ich mich bei Julia Hengenbart bedanken, die mich immer mal wieder auf den Boden der Tatsachen zurückholt und mir zeigt, dass es auch noch Anderes im Leben gibt.

Mein größter Dank geht an mein Freund Florian Trommer und meine Familie.

Lieber Flo, ich danke Dir, dass Du mich in den letzten Jahren so unterstützt hast und auch nicht davor zurückgeschreckt bis als Optiker meine Doktorarbeit zu lesen und zu korrigieren. Ich danke Dir, dass Du mich immer mal wieder zu einem "Zwangsurlaub" verdonnert hast, wenn ich anfing in der Nacht von Kryostaten zu reden. Ich hoffe ich kann mich in dem gleichen Umfang in absehbarer Zeit revanchieren.

Meinen Eltern möchte ich für all die Hilfestellungen im Leben danken, die man als Kind als selbstverständlich entgegennimmt. Vielen Dank, dass Ihr mir eine sorgenfreie Ausbildung ermöglicht und mich immer in meinen Ideen bestärkt habt. Vielen Dank auch an meine Geschwister Martin, Thomas und Angelika. Mit Euch macht Familie doch gleich mehr Spaß.